MAGNETIC PROPERTIES OF AB-STACKED KAGOME LATTICE CRYSTALS: SYMMETRY, ORDER, AND DUALITY

by

Andrey Zelenskiy

Submitted in partial fulfillment of the requirements
for the degree of Doctor of Philosophy

at

Dalhousie University
Halifax, Nova Scotia
August 2023

To my family.

Table of Contents

List of Tables

List of Figures

Abstract

Competing interactions have long been recognized as a fundamental mechanism driving the emergence of complex phases in a wide range of physical systems. In magnetic systems, these competitions arise from the geometry of the underlying lattice and manifest as geometric frustration or various spin-orbit coupling effects. A prototypical example of geometrically frustrated systems is the antiferromagnetic kagome lattice. Although the exotic properties of the 2D kagome layers have been investigated extensively over the years, a relatively small number of studies considered the effects of a 3D stacking.

This work concerns the magnetic properties of compounds composed of AB-stacked kagome layers. We perform the analysis from the ground up, starting with a derivation of a spin Hamiltonian from symmetry principles. The resulting magnetic model exhibits a fascinating self-duality property: different sets of model parameters are related to each other through changes of the reference frame. By exploiting these relationships, we are able to provide a very general description of the magnetic properties of AB-stacked kagome lattices, including a detailed classification of possible magnetic phases, which we obtain by performing numerical Monte Carlo simulations. Some of the phases, characterized by the magnetic wavevector $\mathbf{Q} = \Gamma$, correspond to magnetic ground states in known compounds, such as Mn_3X systems, where $X = \{\mathrm{Sn}, \mathrm{Ge}, \mathrm{Ga}\}$. To aid the experiments and resolve recent controversies in the literature, we investigate the effects of the magnetic anisotropy in these structures and provide analytical solutions for changes in the spin configurations induced by these interactions. Finally, we study a more exotic set of phases, where the spin structure consists of irregular Ising-like patterns.

The theoretical results reported here are relevant to a number of known magnetic compounds with the AB-stacked kagome structure. Throughout this work, we refer to potential experiments that may verify our predictions. We hope that the present study would lead to further theoretical and experimental investigations of these fascinating systems.

Acknowledgements

First and foremost, I would like to thank my supervisors, Dr. Theodore Monchesky and Dr. Martin Plumer, for inviting me to Halifax to pursue a graduate program at Dalhousie University. I am incredibly thankful for their guidance and encouragement throughout this degree. I owe my qualification as a researcher to their patience and support. I would also like to extend this gratitude to Dr. Byron Southern at the University of Manitoba, who, in many ways, acted as a third supervisor and was always available for discussions and helpful suggestions.

I am grateful for the predoctoral Killam fellowships that generously supported my graduate work.

I thank the members of my supervising committee, Dr. Andrew Rutenberg and Dr. Kimberley Hall, for their helpful comments regarding this work. I also thank Dr. Stephen Payne and Dr. Jesse Maassen, with whom I had the pleasure of working as a TA during my time at Dalhousie. In addition, I thank Dr. Maassen for stepping up as a temporary committee member during my preliminary examination.

I thank the theory group at the Institute Laue-Langevin and especially Dr. Mike Zhitomirsky and Dr. Tim Ziman for welcoming me during my stay at Grenoble.

I am beyond grateful for the support of my colleagues and friends at the Monchesky Lab (Moncheskions). Dave, Cam, Jason, and Brett – you made my time at Dalhousie exciting and fun.

Lastly, I want to thank my family for being my biggest supporters. To my parents, my family in Kazakhstan, and my in-laws – your encouragement has helped me persevere. Most importantly, I thank my wife for believing in me even when I did not believe in myself. None of this would have been possible without her everyday love and kindness.

Chapter 1

Introduction

> Antiferromagnets are extremely interesting from the theoretical viewpoint but do not seem to have any applications.
>
> Louis Néel, *Nobel Lecture*

Antiferromagnets, first predicted by Louis Néel in 1936 [1], initially were nothing more than an academic curiosity. The absence of spontaneous magnetization in zero magnetic field rendered them useless for any practical applications, as noted by Néel himself during his Nobel Prize lecture [2]. Lack of magnetization also resulted in a controversy about the magnetic structure of these systems, until in 1949 the first neutron scattering experiments confirmed the anticollinear spin configurations in antiferromagnets [3].

Nowadays, Néel's statement in 1936 is no longer accurate: recent developments in the data storage industry have indicated a need to go beyond the conventional ferromagnetic storage devices in order to meet the ever-increasing demands for materials with higher storage capacity [4, 5]. In an effort to reduce the power consumption and increase the writing speed of the modern storage technologies, a recently emerged field of antiferromagnetic spintronics has put out proposals for antiferromagnetic data storage devices [6, 7]. On the academic front, the investigation of antiferromagnetic systems catalyzed a chain reaction of discoveries, which completely changed the landscape of condensed matter research. Two important examples of impactful discoveries that resulted from studies of antiferromagnets are the *geometric frustration* and *Dzyaloshinskii-Moriya* (DM) interactions. Both situations describe competitions between magnetic interactions that arise as a result of the geometry of the underlying lattice.

In nature, competing forces frequently lead to the formation of complex structures, from the fractal patterns of snowflakes to the intricate architecture of living organisms. This phenomenon is ubiquitous across different physical systems and holds important implications for a range of scientific fields, from physics to biology. The work discussed in this thesis focuses on different magnetic competitions and the properties that may arise from them. Therefore, this chapter is dedicated to the discussion of the origins of competing interactions in magnetic systems. At the same time, we will introduce the subject of our studies: the AB-stacked kagome layers.

1.1 Geometrical frustration

1.1.1 Exchange interaction

It was rigorously established in the early 1900's first by Niels Bohr and later by Hendrika van Leeuwen that a system, in which the magnetic fields originate from an angular motion of charged particles, cannot develop an equilibrium magnetization at any finite temperature, even in the presence of an applied magnetic field [8, 9]. This theorem appeared to be in clear contradiction to the observed phenomena: after all, there are lots of examples of magnetic systems in nature. The resolution of this dilemma came with the development of quantum mechanics. After the discovery of spin by Pauli in 1924 [10], Heisenberg and Dirac [11, 12] proposed a coupling mechanism between two spins, thus concluding that the origin of magnetic order is purely quantum-mechanical.

Heisenberg interactions arise when in addition to spin-independent energy terms, such as kinetic energy and Coulombic interactions, we also consider quantum-mechanical constraints imposed by the Pauli exclusion principle. Specifically, the total many-electron wavefunction, which includes spin degrees of freedom, must be antisymmetric with respect to odd permutations of particles. This constraint leads to a difference in Coulomb energy between the singlet and triplet spin states, which results in an effective spin interaction

$$E(\mathbf{r}, \mathbf{r}') = J(\mathbf{r} - \mathbf{r}')\mathbf{S}(\mathbf{r}) \cdot \mathbf{S}(\mathbf{r}'), \tag{1.1}$$

where the spins $\mathbf{S}(\mathbf{r})$ are labeled by their positions in space, $\mathbf{r}$, and $J(\mathbf{r} - \mathbf{r}')$ is the coupling constant, which depends on the types and relative contributions of electron interactions in a given system. This interaction is known as the *Heisenberg exchange* coupling, in reference to the imposed permutation symmetry due to the Pauli principle. Since the original derivation, many other mechanisms of magnetic exchange have been discovered [13].

Although eq. (1.1) is only strictly correct for a system with two spins, these exchange interactions are often generalized in an effective Hamiltonian, which includes many spins:

$$\mathcal{H}_J = \sum_{\mathbf{r}\mathbf{r}'} E(\mathbf{r},\mathbf{r}') = \sum_{\mathbf{r}\mathbf{r}'} J(\mathbf{r}-\mathbf{r}')\mathbf{S}(\mathbf{r})\cdot\mathbf{S}(\mathbf{r}'), \tag{1.2}$$

where the sum is over all pairs of spins in the system. Note that since this definition is essentially an approximation to the true many-body interaction, the exact values of the exchange constants, $J(\mathbf{r}-\mathbf{r}')$, are often less important than their signs, which can often be obtained without the use of electronic structure calculation methods. In many systems, the magnitude of the exchange coupling constant is an exponentially decaying function of the distance between two spins. Therefore, it is common in the initial analysis of the problem to restrict the sum in Eq. (1.2) to nearest-neighbours (NN) only[1].

Strictly speaking, the spin variables are quantum objects, and the model in eq. (1.2) describes a quantum many-body system. In practice, most compounds[2] are well described by a "classical" approximation, where the quantum operators are replaced by components of real vectors with fixed magnitude: $|\mathbf{S}(\mathbf{r})| = S$. In this thesis we will use classical spins with $S = 1$ (which is equivalent to rescaling the coupling constants by a factor S^2).

---

[1] Note that in metallic systems, the itinerant electrons lead to the so-called Ruderman–Kittel–Kasuya–Yosida (RKKY) exchange, which is characterized by a slowly decaying and oscillating exchange coupling of the form $J(\mathbf{r}-\mathbf{r}') \sim \cos\big(k_F|\mathbf{r}-\mathbf{r}'|\big)/|\mathbf{r}-\mathbf{r}'|^3$, where k_F is the Fermi momentum.

[2] Typically, quantum effects are strongest for spins with quantum number $s = \frac{1}{2}$. The properties of compounds in which the magnetic ions have a total spin that is larger than $s = 1$ are often indistinguishable from classical predictions [14].

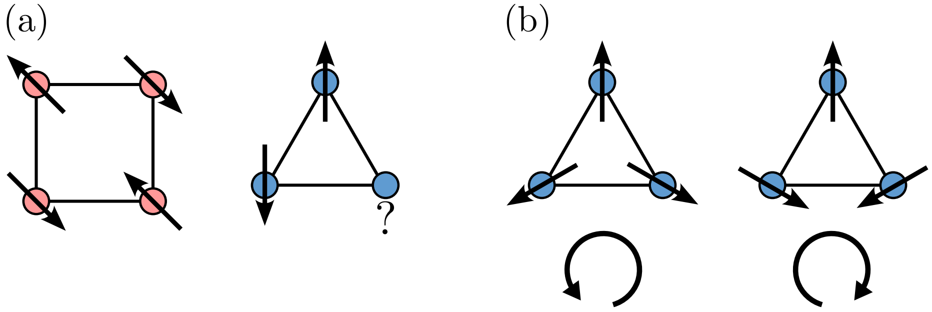

Figure 1.1: An illustration of geometric frustration. (a) Antiferromagnetic exchange interactions can be satisfied on each bond on a square. On a triangle, a collinear configuration will always result in at least one parallel pair of spins, which means that the system is frustrated. (b) Continuous spins on a triangle minimize antiferromagnetic exchange interactions by forming the 120 degree configurations. These structures break the mirror symmetry and are therefore chiral.

Note that the exchange interactions are isotropic[3], meaning that we can apply any global orthogonal transformation (*e.g.* a rotation) to a spin configuration without changing its energy. In practice, changing the relative orientations of spins with respect to the lattice also changes the energy due to magnetic anisotropy, which will be discussed in Sec. 1.2.

1.1.2 Lattice connectivity constraints

The exchange interaction in eq. (1.1) is minimized when two spins are parallel (ferromagnetic coupling $J(\mathbf{r}-\mathbf{r}') < 0$) or antiparallel (antiferromagnetic coupling $J(\mathbf{r}-\mathbf{r}') > 0$) to each other. We see that in order to minimize the exchange interactions on each bond in the system, we have to ensure that each bond corresponds to either a parallel or antiparallel orientation of a spin pair. This geometric constraint can always be satisfied if all interactions are ferromagnetic, since in this case all spins simply have the same orientation. On the other hand, antiferromagnetic arrangements require the possibility of splitting the lattice into two sublattices. For example, the geometric constraint is satisfied on a square lattice, but fails on a triangular lattice, since on each triangle there would always be a single parallel pair of spins (fig. 1.1 (a)). Generally, the system is said to be geometrically frustrated when the geometric constraints imposed by the interactions on each bond cannot be satisfied simultaneously.

---

[3] Because the scalar product only depends on the relative orientations of the vectors.

If we restrict the orientations of spins to be along a single axis (*i.e.* if we consider Ising spins), the frustrated antiferromagnetic structures on a triangular geometry would have a degeneracy, associated with the location of the ferromagnetic bond. The implications of this degeneracy are much greater for lattices formed by tiling equilateral triangles, since the large multiplicity of the ground state ($W_{\mathrm{G.S.}}$) leads to a finite residual entropy per spin $S_{\mathrm{G.S}} = \lim_{N\to\infty} \frac{1}{N}\ln(W_{\mathrm{G.S.}})$, where N is the total number of spins. This was first investigated by Wannier in 1950, who concluded that antiferromagnetic Ising triangular lattice remains disordered down to $T = 0$ [15, 16]. He also calculated the residual entropy of this system to be $S_{\mathrm{G.S}}^{\mathrm{(tri}} \approx 0.323$.

Removing the Ising constraint and introducing continuous Heisenberg spins allows one to minimize the exchange energy of a triangle by introducing a non-collinear 120 degree configuration (fig. 1.1 (b)). In the triangular lattices, the 120 degree ground state corresponds to a commensurate helix with period 3 and has zero residual entropy.

1.1.3 Kagome lattice antiferromagnet

Besides the antiferromagnetic triangular lattice, one of the most famous examples of geometric frustration is the NN antiferromagnetic kagome[4] lattice, which is constructed from corner-sharing equilateral triangles, as shown in fig. 1.2.

Kano and Naya [17] calculated the residual entropy in the antiferromagnetic Ising kagome system to be even larger than in the triangular lattice: $S_{\mathrm{G.S}}^{\mathrm{(kag)}} \approx 0.502$. For continuous spins, the exchange interaction in eq. (1.2) can be rewritten as a sum over the elementary triangles:

$$\begin{aligned}
\mathcal{H}_J &= J\sum_{\langle \mathbf{r}\mathbf{r}'\rangle} \mathbf{S}(\mathbf{r})\cdot\mathbf{S}(\mathbf{r}') \\
&= J\sum_{\triangle}\left[\mathbf{S}_{\triangle,1}\cdot\mathbf{S}_{\triangle,2} + \mathbf{S}_{\triangle,2}\cdot\mathbf{S}_{\triangle,3} + \mathbf{S}_{\triangle,3}\cdot\mathbf{S}_{\triangle,1}\right] \\
&= -JN + \frac{J}{2}\sum_{\triangle}|\mathbf{L}_{\triangle}|^2, \qquad (1.3)
\end{aligned}$$

---

[4] The name comes from the Japanese woven bamboo pattern, 籠目, where *kago* means “basket” and *me* means “eye”, referring to the hexagonal holes in the pattern.

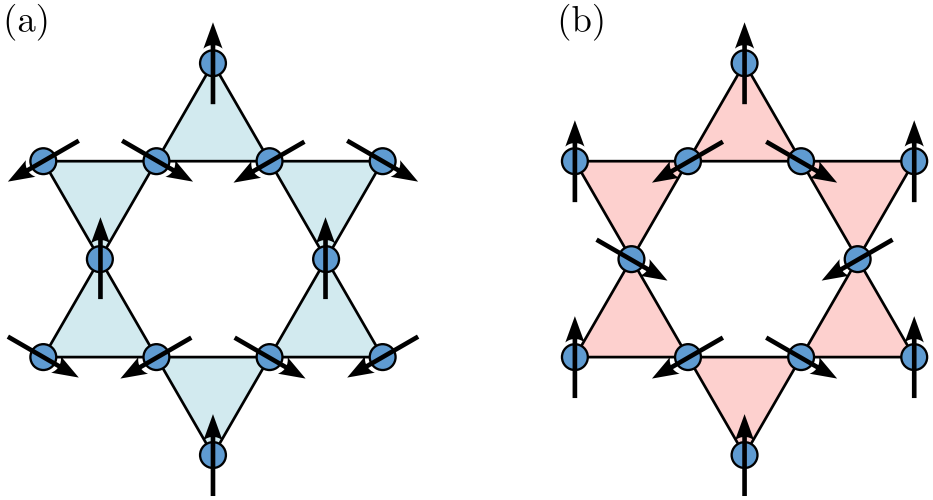

Figure 1.2: Antiferromagnetic configurations on a 2D kagome lattice. The lattice is formed by corner-sharing triangles. The two ordered spin configurations shown here correspond to the famous (a) $\mathbf{Q} = 0$ and (b) $\mathbf{Q} = \mathrm{K}$ (also known as $\sqrt{3} \times \sqrt{3}$) structures.

where N is the number of lattice sites, $J > 0$, $\langle \cdots \rangle$ represent NN bonds, $\triangle$ labels elementary triangles composed of three spins $\mathbf{S}_{\triangle,i}$, $i \in \{1, 2, 3\}$, and

$$\mathbf{L}_{\triangle} = \mathbf{S}_{\triangle,1} + \mathbf{S}_{\triangle,2} + \mathbf{S}_{\triangle,3}. \tag{1.4}$$

The ground state corresponds to $\mathbf{L}_{\triangle} = 0$ for every triangle in the system, which is equivalent to setting a 120 degree configuration on each kagome triangle. Note that we can rotate the plane of the 120 degree structure in fig. 1.1 by an arbitrary angle without distorting the spin configuration and thus leaving the energy unchanged. These rotations are therefore referred to as the zero-energy (or simply zero) modes. It turns out that as we go from individual triangles to the connected kagome lattice, a large number of these zero modes survive, leading to a continuous manifold of ground state configurations [18–21]. We show two possible ordered structures in fig. 1.2 (a) and (b), but in general these systems remain disordered, as a result of the entropic cost to form periodic structures. For this reason, the ground state of antiferromagnetic kagome lattice is often called the *classical spin liquid* phase[5]. As a result of this classical degeneracy, the properties of the system become very sensitive

---

[5] The name comes from the fact that the spins exhibit local correlations, but remain disordered on a macroscopic scale, just like atoms or molecules in a liquid.

to various perturbations, including changes in the connectivity as well as thermal and quantum fluctuations. Thus, at low temperatures quantum effects determine the physical quantities of the system [22].

1.2 Anisotropic interactions

Apart from site connectivity, the effects of the underlying lattice on the magnetic structure may manifest through the spin-orbit coupling (SOC), which allows the spins to "feel" the local electronic environment of the atom[6]. In turn, the local environment imposes the symmetry of the crystal onto the spins, leading to magnetic anisotropy. All magnetic compounds are anisotropic to some degree, and therefore it is often necessary to consider anisotropic spin interactions in order to provide a realistic description of the material properties. Importantly, these interactions sometimes compete with the isotropic exchange couplings, resulting in more complicated spin arrangements.

1.2.1 Single-ion anisotropy

The most common type of anisotropic interactions arises from the crystal electric fields acting on the magnetic site. Depending on the nature of the surrounding atoms, electrostatic interactions may either decrease or increase the energy of certain orbitals, and, via spin-orbit coupling, impose favourable and unfavourable directions for the spins [23]. Due to the nature of this anisotropy, it is commonly referred to as the *single-ion anisotropy* (SIA). SIA results in effective couplings between spin components on the same atomic site. Typically, the lowest order terms are quadratic[7]:

$$\mathcal{H}_K = \sum_{\mathbf{r}} \sum_{\alpha} K_\alpha \left(\hat{\mathbf{n}}_\alpha(\mathbf{r}) \cdot \mathbf{S}(\mathbf{r}) \right)^2 , \tag{1.5}$$

where $\hat{\mathbf{n}}_\alpha(\mathbf{r})$ label principal axes of anisotropy (labelled by α) for each site $\mathbf{r}$, and K_α are the corresponding SIA coefficients. Note that if K_α is negative (positive), the

---

[6] Without spin-orbit coupling, spin and lattice degrees of freedom are decoupled. In this case, there is no preferred global orientation of the structure with respect to the lattice.

[7] This is not the case in cubic systems, where the lowest order of SIA is 4. In general, the order of spin interactions must be even, as a result of the time-reversal symmetry, as discussed in Sec. 2.2.

spins prefer to lay parallel (perpendicular) to $\hat{\mathbf{n}}_\alpha(\mathbf{r})$, which are then called easy (hard) axes.

Depending on the strength of the SOC, the strength of the SIA varies from one compound to another. In most cases, the anisotropy is much weaker than exchange and can be treated as a perturbation to the exchange interaction, while in other it may be the dominant type of interactions. However, sometimes, it is possible to deduce the relative strengths of different SIA couplings based on the symmetry. For example, in a monoclinic crystal with sides $a \approx b \ll c$ or $a \approx b \gg c$ we would expect the anisotropy in the ab plane to be less significant than along the c-axis.

1.2.2 Dzyaloshinskii-Moriya interactions

During the late 1950's, one of the biggest questions in the magnetic community was the origin of weak ferromagnetism in several antiferromagnetic materials, such as $\alpha - \mathrm{Fe}_2\mathrm{O}_3$ and MnCO_3. These compounds exhibit antiferromagnetic spin ordering that is distorted by a small spin canting, which in turn leads to a small magnetic moment. Models with isotropic exchange and SIA were not sufficient to explain this phenomena, which pointed towards another type of magnetic interactions. This puzzle was first solved by Dzyaloshinskii [24], who used a symmetry approach in order to construct a phenomenological model, which included *antisymmetric* spin invariants. Several years after Dzyaloshinskii's article, following the success of Anderson's superexchange formulation [13], Moriya attempted to provide a microscopic origin of antisymmetric exchange by proposing a perurbative calculation with included Coulombic and SOC interactions. Moriya showed that the SOC and the symmetries of the underlying lattice result in *antisymmetric exchange interactions* of the form

$$E(\mathbf{r}, \mathbf{r}') = \mathbf{D}(\mathbf{r} - \mathbf{r}') \cdot [\mathbf{S}(\mathbf{r}) \times \mathbf{S}(\mathbf{r}')], \tag{1.6}$$

where $\mathbf{D}$ is a vector with an antisymmetric property, $\mathbf{D}(\mathbf{r}-\mathbf{r}') = -\mathbf{D}(\mathbf{r}'-\mathbf{r})$ [25]. This type of interactions is referred to as the Dzyaloshinskii-Moriya (DM) interaction, in tribute to the pioneering work of the two researchers. Similar to the case of Heisenberg exchange, one can generalize this two-body interaction to an effective Hamiltonian:

$$\mathcal{H}_D = \sum_{\mathbf{r}\mathbf{r}'} \mathbf{D}(\mathbf{r}-\mathbf{r}') \cdot [\mathbf{S}(\mathbf{r}) \times \mathbf{S}(\mathbf{r}')]. \tag{1.7}$$

The form (orientation) of the DM vector is determined by the local symmetry of the bond, whereas the magnitude and sign (*i.e.* direction along a specified axis) depend on the details of the electronic structure. In addition to the derivation of the microscopic model, Moriya proposed a set of simple rules for determining the direction of the DM vector, $\mathbf{D}(\mathbf{r}-\mathbf{r}')$, for two spins at $\mathbf{r}$ and $\mathbf{r}'$ forming a bond $\boldsymbol{\rho} = \mathbf{r} - \mathbf{r}'$ with midpoint $\mathbf{O}$:

1. If there is a point of inversion at $\mathbf{O}$, $\mathbf{D} = 0$
2. If there is a mirror plane that passes through $\mathbf{O}$ and is perpendicular to $\boldsymbol{\rho}$, $\mathbf{D} \perp \boldsymbol{\rho}$
3. If there is a mirror plane which includes $\boldsymbol{\rho}$, $\mathbf{D} \perp$ mirror plane
4. If there is a two-fold rotation axis, $\hat{\mathbf{C}}_2$, that passes through $\mathbf{O}$ and is perpendicular to $\boldsymbol{\rho}$, $\mathbf{D} \perp \hat{\mathbf{C}}_2$
5. If there is an n-fold rotation axis ($n \geq 2$), $\hat{\mathbf{C}}_n$, along $\boldsymbol{\rho}$, $\mathbf{D} \parallel \boldsymbol{\rho}$

Symmetric and antisymmetric exchange interactions in eqs. (1.1), (1.6) produce competitions between collinear and orthogonal spin configurations, resulting in spin canting away from the collinear order. Since DM interactions favour non-collinear configurations, they are known to be crucial for stabilization of helical structure with a particular chirality (depending on the sign of $\mathbf{D}$). Furthermore, these chiral interactions have been shown to stabilize exotic spin textures, such as skyrmions [26, 27].

1.2.3 Anisotropic exchange

Moriya's derivation produced another anisotropic interaction, which was symmetric with respect to the exchange of spins in a given bond. These interactions are generally referred to as the *anisotropic exchange* and can be written as

$$\mathcal{H}_A = \sum_{\mathbf{r}\mathbf{r}'} \sum_{\alpha\beta} A^{(\alpha\beta)}(\mathbf{r}-\mathbf{r}') S_\alpha(\mathbf{r}) S_\beta(\mathbf{r}'), \tag{1.8}$$

where the form of the coupling matrix $A^{(\alpha\beta)}(\mathbf{r}-\mathbf{r}') = A^{(\alpha\beta)}(\mathbf{r}'-\mathbf{r})$ is determined by the symmetry of the local environment of the bond.

From Moriya's perturbation theory it follows that while the DM couplings depend linearly on the strength of the SOC, the symmetric part of the anisotropic exchange shows quadratic dependence on the SOC parameter. As a result, anisotropic exchange interactions are typically much weaker perturbations than the DM interactions. However, they are always present in the crystal environment and may sometimes account for the properties that are incompatible with other interactions. Several studies also indicated situations where the anisotropic exchange may exactly balance the DM couplings [28, 29]. More recently, anisotropic interactions received a considerable amount of attention due to their role in stabilizing exotic phases, especially the Kitaev spin liquids [30].

1.3 AB-stacked kagome lattices

We have already introduced kagome antiferromagnets as a paradigmatic example of geometric frustration. The properties of these systems, including the extensive degeneracy of the ground state are extremely sensitive to various perturbations, such as anisotropic interactions or changes in the geometry. For this reason, the classical spin liquid ground state opens a wide playground for stabilizing various unconventional phases. For example, recently, in a series of works dedicated to the effects of anisotropic interactions in kagome magnets, Essafi, Rosales, and Jaubert demonstrated that DM interactions allow for a stabilization of unusual chiral phases, including chiral spin liquids, skyrmions, and bimeron glass [31–33].

Most theoretical studies that have been conducted on the magnetic properties of kagome typically concern 2D systems. The bulk limit is achieved by stacking the kagome layers on top of each other. The most common types of stacking are the AA, AB, and ABC stacking. The AA layered kagome (fig. 1.3 (a)) is the simplest type of layering, which preserves the symmetry of the 2D kagome layers. The studies of this category of bulk kagome compounds are rather sparse [34, 35]. However, we note that because the AA stacking does not introduce any additional frustration, the properties of the 3D systems are expected to be similar to those in the 2D limit. On the other hand, the ABC-stacking (fig. 1.3 (c)) introduces frustrated octahedral units

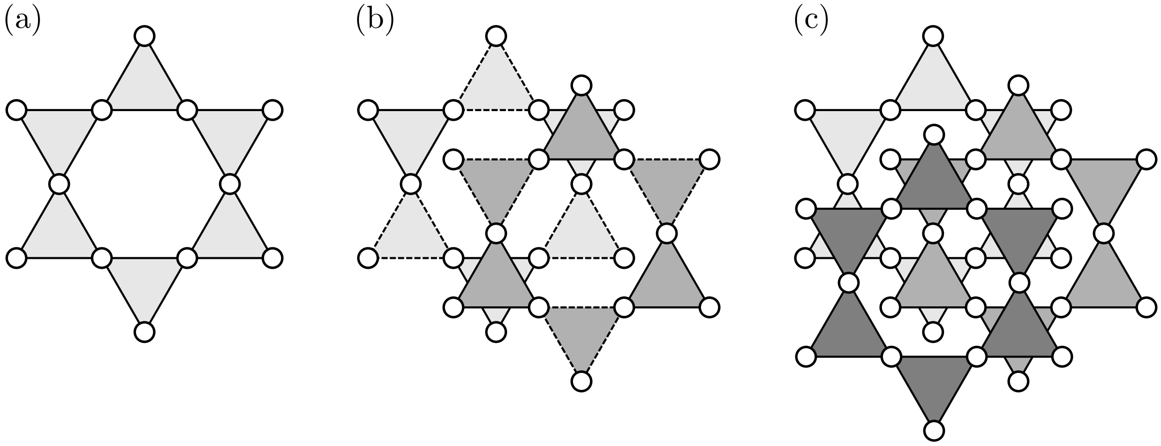

Figure 1.3: Examples of stacked kagome lattices. (a) AA-stacked, (b) AB-stacked, and (c) ABC-stacked kagome layers. In (b), the solid and dashed lines indicate the two inequivalent triangles in the case of a breathing anisotropy.

in each crystallographic unit cell, which both increases the symmetry of the system and introduces additional frustration compared to the 2D limit. The most well-studied ABC-stacked kagome system is the metallic $\mathrm{Mn_3Ir}$ compound [36–44]. The properties of $\mathrm{Mn_3Ir}$ is of high interest for industrial applications, such as spin-valve technologies [45].

Until recently, the AB-stacked kagome layers (fig. 1.3 (b)) (AB-SKL) have remained relatively unstudied. Like the 2D kagome, the AB-SKL have a hexagonal symmetry but the inter-layer interactions introduce additional frustration, similar to the ABC stacking. An interesting consequence of the AB stacking is a possibility of the *breathing anisotropy*, where the “up” and “down” kagome triangles have different sizes (fig. 1.3 (b)).

The interest in these systems has grown rapidly in recent years, due to the experimental discovery of the anomalous Hall effect (AHE) in a class of metallic compounds with a general formula $\mathbf{Mn_3X}$, $\mathbf{X} = \{\mathbf{Ge}, \mathbf{Sn}, \mathbf{Ga}\}$ [46–49]. The AHE has been an open problem in theoretical and experimental physics for over a century since it intertwines the concepts of topology and geometry [50, 51]. Moreover, until the discovery of this effect in $\mathrm{Mn_3}X$ compounds, which host non-collinear antiferromagnetic order, the AHE has only been observed in ferromagnetic materials with strong spin-orbit coupling [46, 52–55].

Besides the $\mathrm{Mn_3}X$ family, there are other examples of compounds in which the magnetic ions form the AB-SKL structure. We will list some of the examples below.

$\mathbf{R_3Ru_4Al_{12}},\ \mathbf{R = \{Gd, La, Pr, Nd, Ce, Yb, Dy, U\}}$ are metallic compounds with AB-SKL formed by the magnetic rare-earth R atoms, identical to the Mn atoms in the Mn_3X family. The properties of $R_3\mathrm{Ru}_4\mathrm{Al}_{12}$ change depending on the R atom, and at low temperatures can manifest in ferromagnetic, non-collinear antiferromagnetic, or more complicated partially-ordered phases [56–64].

$\mathbf{T_3X_2},\ \mathbf{T = \{Fe, Mn, Cr\}},\ \mathbf{X = \{Ge, Sn\}}$ is another family of metallic compounds. However, in this case the crystal structure is different from the previous two examples, since the AB kagome bilayers of T atoms are separated from each other by significant distances. Therefore, to a good level of accuracy these systems can be approximated as isolated AB kagome bilayers. The most studied member of the family is $\mathrm{Fe_3Sn_2}$, which is ferromagnetic at room temperature, but has recently been shown to stabilize complex phases at lower temperatures, such as magnetic bubbles [65–69].

$\mathbf{R_3BWO_9},\ \mathbf{R = \{Pr, Nd, Gd, Ho\}}$ is a family of recently discovered compounds with a distorted kagome structure. The first magnetic measurements conducted on $\mathrm{Nd_3BWO_9}$ found commensurate and incommensurate orders at significantly suppressed temperatures [70].

Surprisingly, despite the plethora of experimental results, the theoretical studies of the AB-SKL remain relatively sparse. Most of the recent effort has been dedicated to the ground state properties of the Mn_3X [71–75]. In view of this, the thesis work presented here attempts to provide a more general study of the effects of AB stacking on the properties of kagome magnets.

From a technological standpoint, the magnetoelectronic properties of certain compounds presented above make them promising candidates for spintronic applications, such as magnetic storage devices. Notably, the aforementioned $\mathrm{Mn_3Ir}$, has been used in almost all hard drives as the antiferromagnetic pinning layer in spin valves. However, the high cost of metallic Ir, as well as undesireable domain formation, makes the devices based on the AB-SKL $\mathrm{Mn_3X}$ compounds even more promising, especially since novel techniques have already been proposed for imaging and writing of magnetic domains in Mn_3Sn [76–79]. This further motivates a thorough investigation of magnetic properties of the AB-SKL compounds.

1.4 Outline of this thesis

The rest of this work is outlined as follows.

Any theoretical discussion of the magnetic properties must begin with the definition of the magnetic model. Therefore, we dedicate Chapter 2 to a derivation of possible magnetic interactions in AB-SKL using symmetry principles. This chapter is loosely based on Ref. [75] and the corresponding supplemental material, but we introduce the derivation using a geometric perspective, without relying on heavy group-theoretical formalism.

In Chapter 3 we introduce an extremely important property of our model, namely *self-duality*. We will discuss in detail the meaning and consequences of self-duality and attempt to provide an approximate relationship between the possible self-duality transformations and the strength of SOC in AB-SKL. This material was first introduced in Ref. [80]. Here, we again choose a geometry-based approach for deriving the self-duality transformations, rather than the group theory-based methodology used in the original reference.

Chapter 4 gives some background on the numerical Monte Carlo methods that we employ to study our systems.

In Chapter 5 we present an extensive numerical study of the ground state properties of our magnetic model, the main focus of Ref. [80]. For simplicity, we separate the discussion into three cases, corresponding to isotropic limit, weak-SOC limit, and strong-SOC limit. The resulting magnetic phases are characterized according to the spatial periodicity and self-duality principles.

The strong-SOC limit is relevant for experimental studies of AB-SKL compounds, especially for the Mn_3X family. Therefore, Chapter 6 provides an in-depth analytical analysis of the effects of in-plane anisotropy on the spin structure of experimentally-relevant magnetic phases. The material in this chapter was partially covered in Ref. [75] and its supplemental material, but it is presented here in a more general and precise form.

Chapter 7 we will serve as an introduction to the properties of the most exotic structures in this study: the Ising-like phases. These results are contained in the recently submitted work in Ref. [81]. This chapter describes the analytical coarse-graining of the magnetic Hamiltonian, which serves to uncover the effective biquadratic interactions, which are expected to stabilize the Ising-like configurations.

Finally, Chapter 8 presents the results of the finite-temperature numerical MC simulations of the Ising-like phases, which reveal a complex three-step nucleation process. The data presented in this chapter is included in Ref. [81] and the corresponding supplemental material.

1.5 Work not presented in this thesis

Although the material in this work already covers a large number of topics, there is a number of projects that the author chose not to present here, in order to focus on a single consistent story. Below are the main topics that are not covered in this thesis, but can be found in Refs. [75], [80], [81], and the corresponding supplementals.

Group theory. As already mentioned, many of the original derivations in Refs. [75] and [80] made heavy use of group theory (specifically, representation theory). To simplify the discussion and eliminate potential confusion, these calculations were focused on more simple geometrical concepts.

Spin waves. The most significant part of Refs. [75] and [80] that is not presented here is the description of the spin wave excitations in the AB-SKL. In Ref. [75], we analyzed the effects of the in-plane anisotropy on the spin wave dispersions and showed that the inelastic neutron scattering intensity is extremely sensitive to small changes in anisotropic constants. These results can be used to fit experimental data and potentially used to determine the relative strengths of different anisotropic interactions. In Ref. [80], we studied spin wave spectra of several magnetic phases, while varying the strength of the SOC. Furthermore, the dispersions corresponding to the collinear configurations in the weak-SOC limit allowed us to demonstrate that thermal fluctuations tend to rotate these structures perpendicular to the kagome layers.

Ising-like phases. Chapters 7 and 8 introduce the reader to some of the properties of the Ising-like phases, but some of the important analytical results are not included here. In particular, the derivation of the Landau theory and the analysis of the fluctuations, which confirmed the Brazovskii-type fluctuation-induced first-order transition are omitted from this thesis and instead are qualitatively described in Chapter 8. However, these results are included in the recently submitted manuscript in Ref. [81] (and its supplemental material). A potential future publication will include thermal properties of Ising-like phases in bulk 3D systems.

Chapter 2

Symmetry and magnetic interactions in AB-SKL

> Reality favours symmetry.
>
> Jorge Luis Borges, *Ficciones*

Symmetry shapes the physical interactions in our universe. It is no coincidence that the classical gravitational and electromagnetic forces, which we deal with on a daily basis, depend only on relative distances between objects and not their absolute positions. This distance dependence comes from the fact that the space in which all matter exists is uniform, and therefore possesses *translational symmetry*. Translational symmetry in turn postulates that the interactions between objects must remain the same if all of them are simultaneously moved to another location in space, while preserving the *relative* positions. Similarly, the isotropy of space also implies *rotational symmetry*, which leads to the spherical symmetry of most fundamental interactions. Thus, for example, the gravitational and electrostatic interactions depend on the scalar distance, rather than the vector displacement between the objects.

These concepts equally apply to systems with reduced symmetry, such as crystal lattices. Although the emergent interactions could be calculated via quantum mechanical principles, the phenomenological symmetry-based approach is more appealing, since the calculations do not require the heavy machinery of numerical methods. By requiring that interactions between spins are invariant with respect to the symmetries of the underlying lattice, one can deduce the *spin invariants*, which will correspond to different types of magnetic couplings. The limitation of this approach is that nothing can be said about the strength of these interactions in a given system, since the invariants only reflect the generic symmetry properties of the crystal and not the specific electronic environments of physical compounds. To overcome this issue, one has to either consider more sophisticated calculation techniques, which inevitably leads back to quantum mechanical algorithms, or to consult experimental data to at least narrow down the parameter space. In the present case, the symmetry approach is sufficient, since we are simply concerned with finding all of the possible types of interactions in order to characterize the phases that can occur when some of the parameters are varied.

The methodology for symmetry-based model derivation, based heavily on group theoretical tools [82], has been developed over the past several decades (see, for example [32,83–85]). However, a consistent approach suitable for physicists with introductory knowledge of mathematical groups is still missing in the literature. Therefore, this section is dedicated to a step-by-step derivation of the magnetic model for AB-SKL using basic symmetry principles, making only occasional references to group theory.

2.1 Transformation properties of spins

To effectively use the symmetry toolbox, one must first understand how the degrees of freedom transform under various symmetry operations. Magnetic systems are characterized by spins, which are three-component vectors. However, it would be a mistake to simply state that spins transform like regular vectors. To understand why this is the case, we recall that spin is a quantum-mechanical property of particles, which describes a type of *angular momentum*. A conventional angular momentum, which describes orbital motion, is defined as

$$\mathbf{L} = \mathbf{r} \times \mathbf{p}, \tag{2.1}$$

where $\mathbf{r}$ and $\mathbf{p}$ label the position and linear momentum of the object. Because it is defined as a cross product, angular momentum and spin are *axial* vectors (as opposed to more familiar *polar* vectors). To determine the transformation properties of axial vectors, we can apply a general orthogonal transformation $\mathbf{R}$ to $\mathbf{r}$ and $\mathbf{p}$ in eq. (2.1), such that

$$\begin{aligned} \mathbf{L}' &= (\mathbf{R}\mathbf{r}) \times (\mathbf{R}\mathbf{p}) \\ &= \det(\mathbf{R})\mathbf{R}(\mathbf{r} \times \mathbf{p}) \\ &= \det(\mathbf{R})\mathbf{R}\mathbf{L}, \end{aligned} \tag{2.2}$$

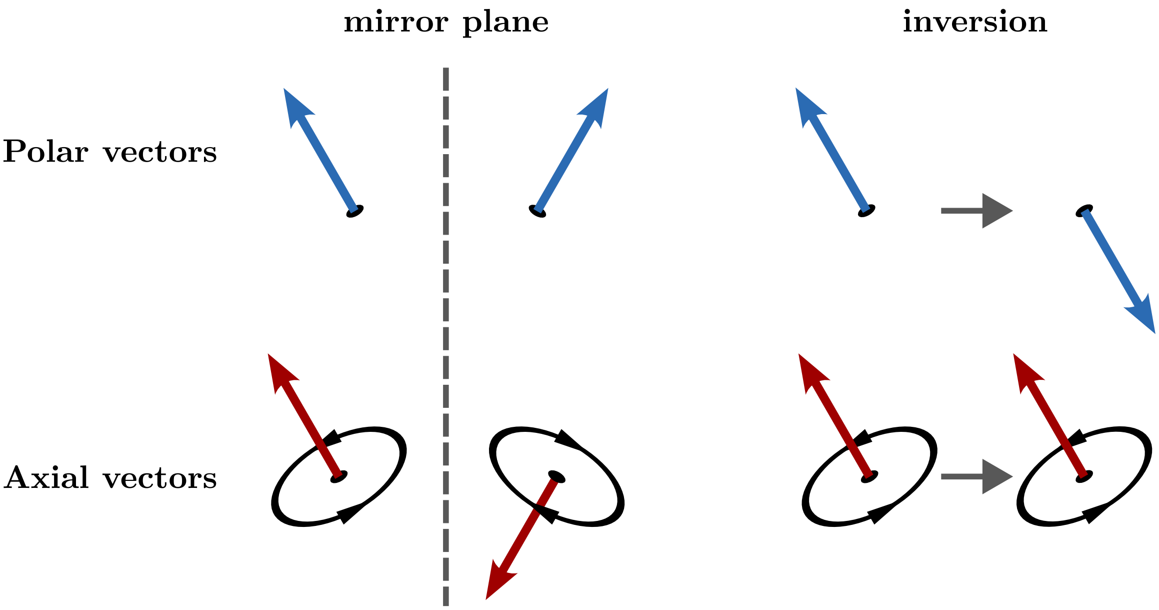

Figure 2.1: Transformation properties of polar and axial vectors. Polar vectors transform “intuitively”, meaning that the mirror reflections and inversion act on the object itself. On the other hand, axial vectors are analogous to magnetic moments originating from a current loop (according to the right-hand rule). This means that their orientation after a transformation depends on whether the direction of the current has been reversed. Such is the case, for example, for reflections with mirror planes lying perpendicular to the current loop. However, inversion operation leaves the axial vector invariant, since it does not change the direction of the current.

where in the second line we used a transformation property of cross products (see Appendix A). Therefore, if $\mathbf{R}$ describes a rotation ($\det(\mathbf{R}) = 1$), the axial and polar vectors transform in exactly the same way. However, if $\mathbf{R}$ represents inversion, improper rotation, or a mirror symmetry ($\det(\mathbf{R}) = -1$), the axial vectors acquire an additional orientation flip after the transformation. To better understand these differences, it is useful to look at a classical analogue of spin: a magnetic moment generated by current in a loop circuit. Fig. 2.1 demonstrates various transformations applied to the magnetic moment.

A current-loop magnetic moment representation is a useful tool for any type of transformation applied to spins. In the following sections, we will consider symmetries that typically arise in magnetic crystals and determine how they influence the form of the spin interactions in AB-SKL.

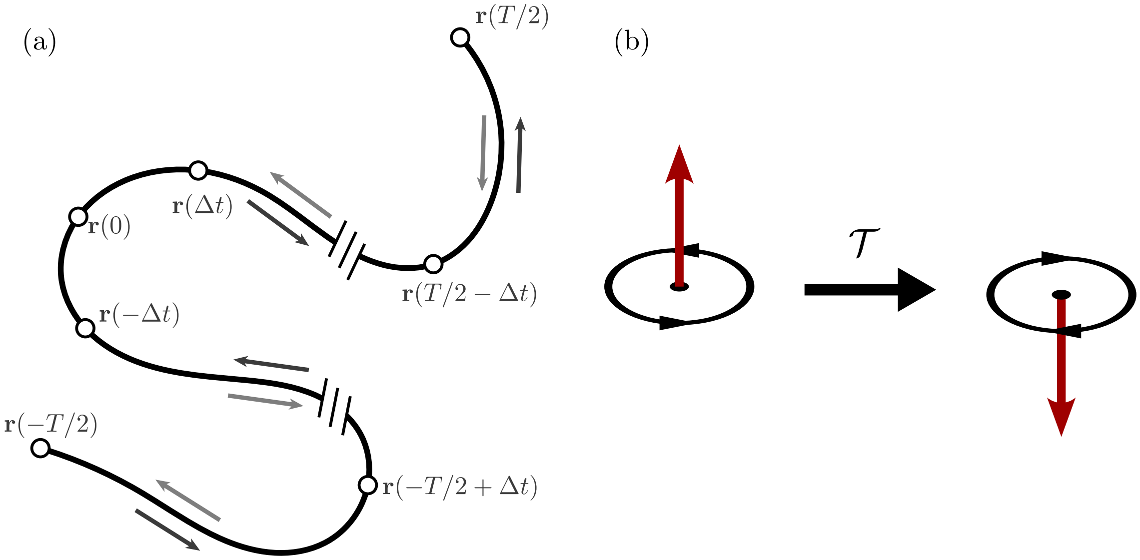

Figure 2.2: Examples of time-reversal operation. (a) given some initial conditions at starting time $t = -T/2$, a particle follows a trajectory, specified by its equations of motion, until we stop the motion at time $t = T/2$. The circles denote positions at regular time intervals Δt and arrows represent the direction of particle's momentum $\mathbf{p}(t)$. Time-reversal changes the direction of motion ($\mathcal{T}(\mathbf{p}(t)) = -\mathbf{p}(-t)$), such that it begins at $\mathbf{r}(T/2)$ and moves towards $\mathbf{r}(-T/2)$. If the energy is conserved, the reversed trajectory will be exactly the same as the original one. (b) Time-reversal operation reverses the momentum of the charge carriers, thus changing the direction of the current and flipping the magnetic moment.

2.2 Time-reversal symmetry

Before we discuss crystals, it is worth talking about a symmetry that characterizes all spin systems, namely, the *time-reversal* symmetry. Unlike the translations and rotations, which act on the spatial degrees of freedom, time-reversal, which we will denote as $\mathcal{T}$, reverses the arrow of time, such that $\mathcal{T} : t \to -t$. In the absence of dissipative forces[1], a given physical variable will either be invariant (even) or change sign (odd) under $\mathcal{T}$. For example, the position of an object is even under the time-reversal operation ($\mathcal{T}(\mathbf{r}(t)) = \mathbf{r}(-t)$), while its momentum is odd ($\mathcal{T}(\mathbf{p}(t)) = -\mathbf{p}(-t)$), as demonstrated in fig. 2.2 (a). Therefore, the angular momentum, defined in eq. (2.1), and consequently the spin, are also odd under the time-reversal. This is more easily understood from the current-loop magnetic moment picture, as shown in fig. 2.2 (b).

---

[1] *i.e.* in an isolated system.

At a microscopic level, a Hamiltonian of the system must be $\mathcal{T}$-invariant in order to ensure the conservation of energy. For this reason, in the absence of the magnetic field[2], the magnetic Hamiltonian will contain only terms that have an even number of spin components. Typically, quadratic terms are sufficient to describe most magnetic properties[3] and we can write a generic model as

$$\mathcal{H} = \sum_{\boldsymbol{\rho}\boldsymbol{\rho}'} \mathcal{H}(\boldsymbol{\rho}, \boldsymbol{\rho}') = \sum_{\boldsymbol{\rho}\boldsymbol{\rho}'} \sum_{\alpha\beta} \mathcal{A}_{\alpha\beta}(\boldsymbol{\rho}, \boldsymbol{\rho}') S_\alpha(\boldsymbol{\rho}) S_\beta(\boldsymbol{\rho}'), \tag{2.3}$$

where $\boldsymbol{\rho}$ and $\boldsymbol{\rho}'$ are the positions of spins, α and β label the spin components, and $\mathcal{A}_{\alpha\beta}(\boldsymbol{\rho}, \boldsymbol{\rho}')$ is a general coupling matrix, which must reflect the symmetry of the crystal.

2.3 Lattice translational symmetry

A crystal is a periodic array of atoms. The periodicity is determined by discrete *lattice translations*, specified by three lattice vectors $\mathbf{a}_1$, $\mathbf{a}_2$, and $\mathbf{a}_3$. Analogous to the continuous translations discussed above, to ensure the invariance of the magnetic interactions with respect to lattice translations, a coupling between spins on sites $\boldsymbol{\rho}$ and $\boldsymbol{\rho}'$ only depends on the displacement $\boldsymbol{\rho} - \boldsymbol{\rho}'$:

$$\mathcal{H}(\boldsymbol{\rho}, \boldsymbol{\rho}') = \sum_{\alpha\beta} \mathcal{A}_{\alpha\beta}(\boldsymbol{\rho} - \boldsymbol{\rho}') S_\alpha(\boldsymbol{\rho}) S_\beta(\boldsymbol{\rho}'). \tag{2.4}$$

The situation is slightly more complicated when we are dealing with a lattice with an atomic basis. This is the case for kagome lattices, which are formed by replacing each vertex point on a triangular lattice with an equilateral triangle of basis atoms. Non-Bravais lattices are characterized by Bravais lattice vectors $\mathbf{r} = n_1\mathbf{a}_1 + n_2\mathbf{a}_2 + n_3\mathbf{a}_3$ (n_i are integers), as well as the basis vectors $\mathbf{r}_i$. Vectors $\mathbf{r}$ determine the positions of the unit cells, while $\mathbf{r}_i$ label the locations of the atoms in each cell, see fig. 2.3 (b). Importantly, while $\mathbf{r}$ are periodic, $\mathbf{r}_i$ are not, which implies that the interaction between spins on $\boldsymbol{\rho} = \mathbf{r} + \mathbf{r}_i$ and $\boldsymbol{\rho}' = \mathbf{r}' + \mathbf{r}_j$ can be written as

---

[2] Similarly to the magnetic moments, magnetic field is odd under $\mathcal{T}$. For non-zero magnetic field, a Hamiltonian will include a Zeeman term, $-\mathbf{H} \cdot \sum_{\boldsymbol{\rho}} \mathbf{S}(\boldsymbol{\rho})$, which is odd in spin.

[3] Higher-order spin interactions do arise in some systems due to, for example, magnetoelastic coupling [86], or the itenerant electrons [87, 88].

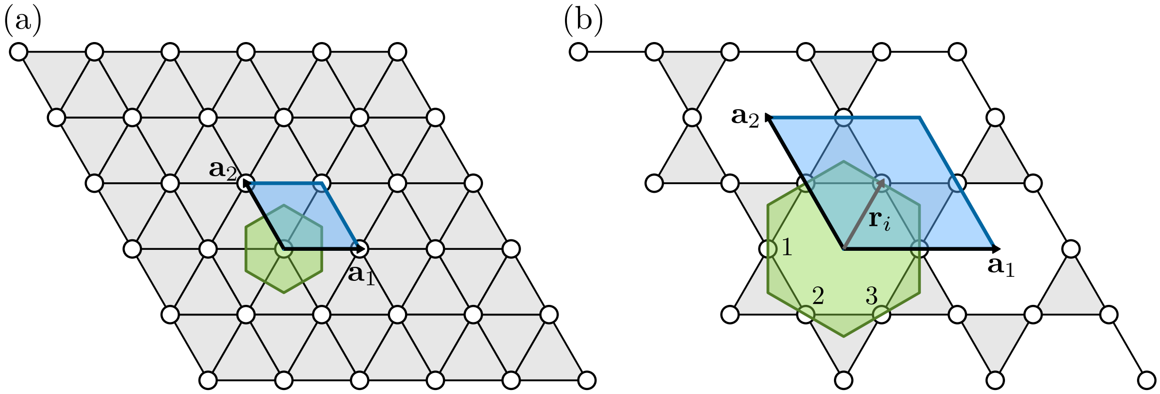

Figure 2.3: Symmetries of the 2D (a) triangular and (b) kagome lattices. On both figures, the black arrows represent lattice vectors $\mathbf{a}_1$ and $\mathbf{a}_2$, while blue and green areas correspond to the conventional and Wigner-Seitz unit cells. In (b), $\mathbf{r}_i$ is one of the basis vectors, and the numbers denote the sublattice atoms. Both lattices have the same point group symmetry, which is more easily seen from the symmetry of the Wigner-Seitz cells. However, while point group operations leave the atoms of the triangular lattice unchanged (assuming translation modulo, see text), they interchange inequivalent sublattice atoms on the kagome lattice.

$$\mathcal{H}(\boldsymbol{\rho}, \boldsymbol{\rho}') = \sum_{\alpha\beta} \mathcal{A}_{ij,\alpha\beta}(\mathbf{r} - \mathbf{r}') S_{i\alpha}(\mathbf{r}) S_{j\beta}(\mathbf{r}'), \tag{2.5}$$

where the basis (sublattice) labels i and j are used as matrix indices to simplify the notation.

2.4 Point group symmetry

Besides lattice translations, crystals generally have a number of other symmetries, including n-fold proper and improper rotations (C_n and S_n respectively), inversion (I), and mirror (σ) transformations. In addition, in *non-symmorphic* crystals some operations are combined with fractional translations. Examples of such transformations are glide plane and screw-axis rotations. The transformations listed above form

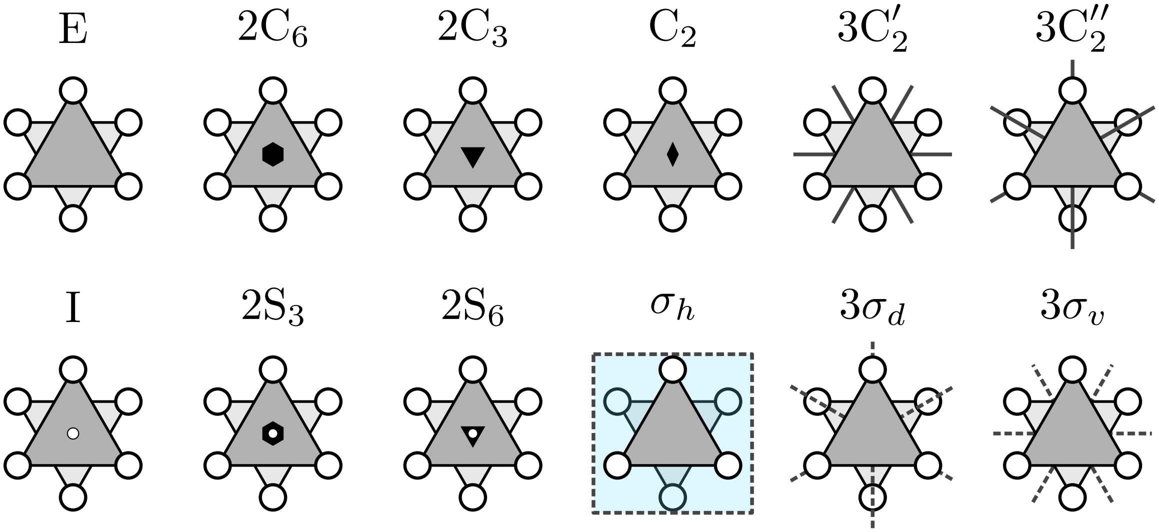

Figure 2.4: Point group symmetries of AB-SKL. The 24 elements are organized into 12 classes of equivalent symmetries. Here, black shapes indicate the type of rotation around the z-axis, white circle implies inversion center, and solid and dashed lines represent the mirror planes. Note that all operations that interchange atoms of A and B layers are non-symmorphic.

the crystallographic *point group*[4]. In Bravais lattices, point groups contain symmetries of an individual atom in the crystal environment (fig. 2.3 (a)). More generally, point groups represent the symmetries of the crystal unit cell, which, in the case of non-Bravais lattice, may generally permute the atoms inside the cell (fig. 2.3 (b)). A combination of translations and point group symmetries produces the *space group* of the crystal. Importantly, point group operations can be obtained by imposing "translation modulo" on all space group operations: if a space group transformation takes some atoms outside of a reference unit cell, we apply an appropriate translation to bring these atoms back inside the cell. For AB-SKL, the point group is D_{6h}, which has 24 elements, illustrated in fig. 2.4. The precise definitions of these symmetry transformations can be found in crystallographic tables [89] (space group 194).

So far, all of the operations discussed here permute the bonds on the lattice, but

---

[4] An observant reader would object to this statement by noting that the non-symmorphic operations described above do not qualify a point group symmetries, as they displace all points from their original positions. However, in crystallography, we still include these operations after removing the fractional translations. This transforms a screw-axis into a rotation and a glide plane into a mirror reflection, which are both valid point group symmetries.

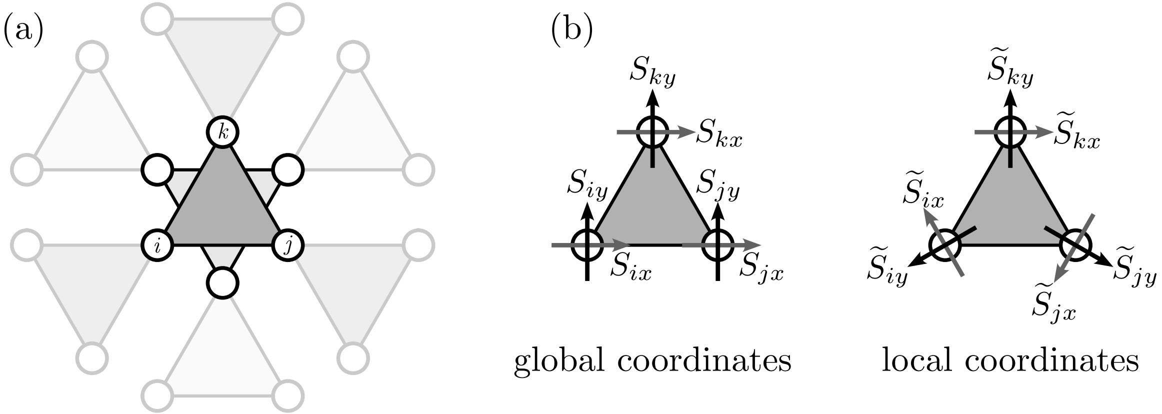

Figure 2.5: (a) Site labels used in the text for the derivation of the intra-layer spin invariants. (b) Global and local spin coordinates on a single triangle. Local axes are obtained by rotations of the global frames on atoms i and j by 120 and -120 degrees respectively.

do not change their magnitudes. A valid magnetic coupling will therefore contain all bonds with the same bond length that transform into each other:

$$\mathcal{H} = \sum_n \mathcal{H}_n, \tag{2.6}$$

$$\mathcal{H}_n = \sum_{\langle \mathbf{r}\mathbf{r}' \rangle_n} \sum_{\langle ij \rangle_n} \sum_{\alpha\beta} \mathcal{A}_{ij,\alpha\beta}(\mathbf{r}-\mathbf{r}') S_{i\alpha}(\mathbf{r}) S_{j\beta}(\mathbf{r}'), \tag{2.7}$$

where n label different "families" of symmetry-related bonds, and $\langle \ldots \rangle_n$ represent positions of bonds in a given family. In practice, the label n usually represents n^{th} nearest-neighbour shell. However, there are situations where two bonds that are unrelated by symmetry have the same length[5].

Besides bond permutations, point group symmetries may also change the orientations of spins. We can determine the possible spin invariants for a given bond family via a simple procedure. For the purpose of demonstration, consider the family of intra-layer NN bonds. First, we select a single bond in this family and determine which point group symmetries leave it in the same location (the atoms on the ends of

---

[5] Such is the case for triangular lattice, where there are two types of 20^{th} neighbours, which have the same bond lengths but are not related by symmetry. Similarly, in kagome lattice, there are two types of 3^{rd} neighbours, since this lattice can be constructed from a triangular lattice with 1/4 depleted sites.

the bond are allowed to be interchanged). Consider the bond between sites i and j in fig. 2.5 (a). Recall that we assume translation modulo for all point group operations. With these rules, there are four qualifying operations: a trivial identity operation E, C_2 rotation around y-axis, xy mirror plane (σ_h), and yz mirror plane (σ_d). These operations compose the C_{2v} point group. The particular choice of a representative bond ensures that the symmetry operations do not permute the components of spins. Next, we analyze how the different couplings between the components of spins i and j transform under these operations. The summary of these transformations is presented in table 2.1 (recall that spins transform like axial vectors). Note that $S_{i\alpha}S_{j\alpha}$ terms are already invariant under all operations of C_{2v}. In principle, one could simply take these terms as three independent couplings, namely $J_{xx}S_{ix}S_{jx}$, $J_{yy}S_{iy}S_{jy}$, and $J_{zz}S_{iz}S_{jz}$. However, it is more instructive to construct the invariants from linear combinations of these terms, such that

E	C_2	σ_h	σ_d
$S_{ix}S_{jx}$	$S_{ix}S_{jx}$	$S_{ix}S_{jx}$	$S_{ix}S_{jx}$
$S_{iy}S_{jy}$	$S_{iy}S_{jy}$	$S_{iy}S_{jy}$	$S_{iy}S_{jy}$
$S_{iz}S_{jz}$	$S_{iz}S_{jz}$	$S_{iz}S_{jz}$	$S_{iz}S_{jz}$
$S_{ix}S_{jy}$	$-S_{iy}S_{jx}$	$S_{ix}S_{jy}$	$-S_{iy}S_{jx}$
$S_{iy}S_{jx}$	$-S_{ix}S_{jy}$	$S_{iy}S_{jx}$	$-S_{ix}S_{jy}$
$S_{ix}S_{jz}$	$S_{iz}S_{jx}$	$-S_{ix}S_{jz}$	$-S_{iz}S_{jx}$
$S_{iz}S_{jx}$	$S_{ix}S_{jz}$	$-S_{iz}S_{jx}$	$-S_{ix}S_{jz}$
$S_{iy}S_{jz}$	$-S_{iz}S_{jy}$	$-S_{iy}S_{jz}$	$S_{iz}S_{jy}$
$S_{iz}S_{jy}$	$-S_{iy}S_{jz}$	$-S_{iz}S_{jy}$	$S_{iy}S_{jz}$

Table 2.1: Transformation properties of quadratic spin expressions on a representative intra-layer NN bond in AB-SKL.

$$H_{ij}^{(1)} = J(S_{ix}S_{jx} + S_{iy}S_{jy} + S_{iz}S_{jz}) = J\mathbf{S}_i \cdot \mathbf{S}_j, \tag{2.8}$$

$$H_{ij}^{(2)} = A^{(xy)}(S_{ix}S_{jx} - S_{iy}S_{jy}), \tag{2.9}$$

$$H_{ij}^{(3)} = A^{(z)}S_{iz}S_{jz}. \tag{2.10}$$

Here, J, $A^{(xy)}$, and $A^{(z)}$ are the isotropic and two anisotropic exchange coupling constants, respectively. The particular set of the linear combinations in eqs. (2.8 - 2.10) is useful because it separates the isotropic and anisotropic interactions, and because the two anisotropic couplings reflect the symmetry of the kagome lattice.

The remaining invariants can be obtained by simply adding terms in a given row of table 2.1. If the resulting sum is non-zero, the expression corresponds to a valid invariant. This gives us an extra term:

$$H_{ij}^{(4)} = D(S_{ix}S_{jy} - S_{iy}S_{jx}) = D\hat{\mathbf{z}} \cdot [\mathbf{S}_i \times \mathbf{S}_j], \tag{2.11}$$

where D is the DM constant, with arbitrarily selected sign.

We have found all spin invariants for a single bond, but how do we extend these expressions to the full bond family? There are two ways to proceed, and these will be reviewed next.

2.4.1 Method 1

The first approach is to perform the same type of symmetry analysis on the remaining non-equivalent bonds. For example, consider the bond between the spins j and k in fig. 2.5 (b). Unsurprisingly, the bond point group is again C_{2v}. However, this time, the C_2 and σ_d operators mix the x- and y-components of spins, which leads to a table of transformations that is different from table 2.1. This change is rather unfortunate, since it implies that the same analysis has to be repeated for all non-equivalent bonds, while yielding the same or similar invariants. To avoid these unnecessary calculations, we employ a useful trick: rather than writing the coordinates of each spin in the same global coordinates (x, y, z), we choose local coordinates for each site ($\tilde{x}_i$, $\tilde{y}_i$, $\tilde{z}_i$), such that the angles between the local coordinates on each bond are the same. This is shown in fig. 2.5 (b). Now, the transformations of quadratic terms $\widetilde{S}_{i\alpha}\widetilde{S}_{j\beta}$ will be identical for all bonds. Fortunately, the expressions in local coordinates transform the same way as presented in table 2.1, and the local bond invariants become

$$\widetilde{H}_{ij}^{(1)} = \widetilde{J}(\widetilde{S}_{ix}\widetilde{S}_{jx} + \widetilde{S}_{iy}\widetilde{S}_{jy} + \widetilde{S}_{iz}\widetilde{S}_{jz}) = \widetilde{J}\widetilde{\mathbf{S}}_i \cdot \widetilde{\mathbf{S}}_j, \tag{2.12}$$

$$\widetilde{H}_{ij}^{(2)} = \widetilde{A}^{(xy)}(\widetilde{S}_{ix}\widetilde{S}_{jx} - \widetilde{S}_{iy}\widetilde{S}_{jy}) \tag{2.13}$$

$$\widetilde{H}_{ij}^{(3)} = \widetilde{A}^{(z)}\widetilde{S}_{iz}\widetilde{S}_{jz}, \tag{2.14}$$

$$\widetilde{H}_{ij}^{(4)} = \widetilde{D}(\widetilde{S}_{ix}\widetilde{S}_{jy} - \widetilde{S}_{iy}\widetilde{S}_{jx}) = \widetilde{D}\hat{\mathbf{z}} \cdot [\widetilde{\mathbf{S}}_i \times \widetilde{\mathbf{S}}_j], \tag{2.15}$$

for all bonds. Here, the local and global z-components are the same. Therefore, in the local coordinates, the coupling matrix $\widetilde{\mathcal{A}}_{ij,\alpha\beta}(\mathbf{r}-\mathbf{r}')$ for the NN intra-layer interactions reads

$$\widetilde{\boldsymbol{\mathcal{A}}}_{ij}(\mathbf{r}-\mathbf{r}') = \begin{bmatrix} \widetilde{J}+\widetilde{A}^{(xy)} & \widetilde{D} & 0 \\ -\widetilde{D} & \widetilde{J}-\widetilde{A}^{(xy)} & 0 \\ 0 & 0 & \widetilde{J}+\widetilde{A}^{(z)} \end{bmatrix}. \tag{2.16}$$

Note that the local coupling constants are different from the global ones. The relationship between the global and local parameters can be determined by expanding $\widetilde{H}_{ij}^{(1,\ldots,4)}$ and relating the resulting expressions to the original $H_{ij}^{(1,\ldots,4)}$ terms. In compact notation, this reads

$$\widetilde{\mathbf{S}}_i(\mathbf{r}) = \mathbf{R}_i\mathbf{S}_i(\mathbf{r}), \tag{2.17}$$

$$\widetilde{\mathbf{S}}_i^T(\mathbf{r})\widetilde{\boldsymbol{\mathcal{A}}}_{ij}(\mathbf{r}-\mathbf{r}')\widetilde{\mathbf{S}}_j(\mathbf{r}') = \mathbf{S}_i^T(\mathbf{r})\boldsymbol{\mathcal{A}}_{ij}(\mathbf{r}-\mathbf{r}')\mathbf{S}_j(\mathbf{r}'), \tag{2.18}$$

$$\boldsymbol{\mathcal{A}}_{ij}(\mathbf{r}-\mathbf{r}') = \mathbf{R}_i^T\widetilde{\boldsymbol{\mathcal{A}}}_{ij}(\mathbf{r}-\mathbf{r}')\mathbf{R}_j. \tag{2.19}$$

In the examples used so far, the rotation matrices are

$$\mathbf{R}_i = \mathbf{R}_j^T = \begin{bmatrix} -\frac{1}{2} & -\frac{\sqrt{3}}{2} & 0 \\ \frac{\sqrt{3}}{2} & -\frac{1}{2} & 0 \\ 0 & 0 & 1 \end{bmatrix}, \mathbf{R}_k = \mathbb{I}, \tag{2.20}$$

where $\mathbb{I}$ is the identity matrix. These transformations give

$$\begin{aligned} \mathbf{R}_i^T\widetilde{\boldsymbol{\mathcal{A}}}_{ij}\mathbf{R}_j &= \begin{bmatrix} -\frac{1}{2}\widetilde{J}+\widetilde{A}^{(xy)}+\frac{\sqrt{3}}{2}\widetilde{D} & -\frac{\sqrt{3}}{2}\widetilde{J}-\frac{1}{2}\widetilde{D} & 0 \\ \frac{\sqrt{3}}{2}\widetilde{J}+\frac{1}{2}\widetilde{D} & -\frac{1}{2}\widetilde{J}-\widetilde{A}^{(xy)}+\frac{\sqrt{3}}{2}\widetilde{D} & 0 \\ 0 & 0 & \widetilde{J}+\widetilde{A}^{(z)} \end{bmatrix} \\ &= \begin{bmatrix} J+A^{(xy)} & D & 0 \\ -D & J-A^{(xy)} & 0 \\ 0 & 0 & J+A^{(z)} \end{bmatrix} = \boldsymbol{\mathcal{A}}_{ij}, \end{aligned} \tag{2.21}$$

$$\begin{aligned}
\mathbf{R}_j^T \widetilde{\boldsymbol{\mathcal{A}}}_{jk} \mathbf{R}_k &= \begin{bmatrix} -\frac{1}{2}\widetilde{J} - \frac{1}{2}\widetilde{A}^{(xy)} + \frac{\sqrt{3}}{2}\widetilde{D} & -\frac{\sqrt{3}}{2}\widetilde{J} + \frac{\sqrt{3}}{2}\widetilde{A}^{(xy)} - \frac{1}{2}\widetilde{D} & 0 \\ \frac{\sqrt{3}}{2}\widetilde{J} + \frac{\sqrt{3}}{2}\widetilde{A}^{(xy)} + \frac{1}{2}\widetilde{D} & -\frac{1}{2}\widetilde{J} + \frac{1}{2}\widetilde{A}^{(xy)} + \frac{\sqrt{3}}{2}\widetilde{D} & 0 \\ 0 & 0 & \widetilde{J} + \widetilde{A}^{(z)} \end{bmatrix} \\
&= \begin{bmatrix} J - \frac{1}{2}A^{(xy)} & D + \frac{\sqrt{3}}{2}A^{(xy)} & 0 \\ -D + \frac{\sqrt{3}}{2}A^{(xy)} & J + \frac{1}{2}A^{(xy)} & 0 \\ 0 & 0 & J + A^{(z)} \end{bmatrix} = \boldsymbol{\mathcal{A}}_{jk}, \qquad (2.22)
\end{aligned}$$

$$\begin{aligned}
\mathbf{R}_k^T \widetilde{\boldsymbol{\mathcal{A}}}_{ki} \mathbf{R}_i &= \begin{bmatrix} -\frac{1}{2}\widetilde{J} + \frac{1}{2}\widetilde{A}^{(xy)} + \frac{\sqrt{3}}{2}\widetilde{D} & -\frac{\sqrt{3}}{2}\widetilde{J} + \frac{\sqrt{3}}{2}\widetilde{A}^{(xy)} - \frac{1}{2}\widetilde{D} & 0 \\ \frac{\sqrt{3}}{2}\widetilde{J} + \frac{\sqrt{3}}{2}\widetilde{A}^{(xy)} + \frac{1}{2}\widetilde{D} & -\frac{1}{2}\widetilde{J} - \frac{1}{2}\widetilde{A}^{(xy)} + \frac{\sqrt{3}}{2}\widetilde{D} & 0 \\ 0 & 0 & \widetilde{J} + \widetilde{A}^{(z)} \end{bmatrix} \\
&= \begin{bmatrix} J - \frac{1}{2}A^{(xy)} & D - \frac{\sqrt{3}}{2}A^{(xy)} & 0 \\ -D - \frac{\sqrt{3}}{2}A^{(xy)} & J + \frac{1}{2}A^{(xy)} & 0 \\ 0 & 0 & J + A^{(z)} \end{bmatrix} = \boldsymbol{\mathcal{A}}_{ki}, \qquad (2.23)
\end{aligned}$$

where we dropped the unit cell labels. The interactions on the B triangle can be obtained similarly and end up being the same as their counterparts on triangle A. The reciprocal interactions (*i.e.* $\boldsymbol{\mathcal{A}}_{ji}$, $\boldsymbol{\mathcal{A}}_{kj}$, and $\boldsymbol{\mathcal{A}}_{ik}$) are conveniently obtained from the transposes of the above matrices. After a few algebraic manipulations, we obtain the following relations between global and local coupling constants:

$$J = -\frac{1}{2}\widetilde{J} + \frac{\sqrt{3}}{2}\widetilde{D}, \qquad (2.24)$$

$$A^{(xy)} = \widetilde{A}^{(xy)}, \qquad (2.25)$$

$$A^{(z)} = \widetilde{A}^{(z)} + \frac{3}{2}\widetilde{J} - \frac{\sqrt{3}}{2}\widetilde{D}, \qquad (2.26)$$

$$D = -\frac{\sqrt{3}}{2}\widetilde{J} - \frac{1}{2}\widetilde{D}. \qquad (2.27)$$

Note that the anisotropic exchange interaction, characterized by $A^{(xy)}$ (from now on referred to as the in-plane anisotropic exchange) is bond-dependent, while the exchange, DM, and the $A^{(z)}$ (out-of-plane) anisotropic exchange are not.

2.4.2 Method 2

The above analysis suggests an even simpler method for obtaining all invariant expressions. Given the bond invariants $H_{ij}^{(1,\ldots,4)}$, we can simply apply operations in the crystallographic point group (D_{6h}) that are not contained in the bond point group (C_{2v}). The most natural choice are the repeated C_6 rotations. The exchange interaction is invariant with respect to all spin rotations and therefore does not change from one bond to the next. The out-of-plane anisotropic exchange and the DM term are invariant under spin rotations around the z-axis (see Appendix A), and also stay the same. Finally, the form of the in-plane anisotropic exchange changes, leading to matrices (2.21 - 2.23) above.

To demonstrate this, consider a C_3 operation, which rotates bond ij to ki, as in fig. 2.5 (a). In the matrix form, it reads

$$\mathbf{R}_3 = \begin{bmatrix} -\frac{1}{2} & \frac{\sqrt{3}}{2} & 0 \\ -\frac{\sqrt{3}}{2} & -\frac{1}{2} & 0 \\ 0 & 0 & 1 \end{bmatrix}. \tag{2.28}$$

Applying this matrix to $\boldsymbol{\mathcal{A}}_{ij}$ yields

$$\begin{aligned} \boldsymbol{\mathcal{A}}_{ki} &= \mathbf{R}_3^T \boldsymbol{\mathcal{A}}_{ij} \mathbf{R}_3 \\ &= \begin{bmatrix} -\frac{1}{2} & -\frac{\sqrt{3}}{2} & 0 \\ \frac{\sqrt{3}}{2} & -\frac{1}{2} & 0 \\ 0 & 0 & 1 \end{bmatrix} \begin{bmatrix} J + A^{(xy)} & D & 0 \\ -D & J - A^{(xy)} & 0 \\ 0 & 0 & J + A^{(z)} \end{bmatrix} \begin{bmatrix} -\frac{1}{2} & \frac{\sqrt{3}}{2} & 0 \\ -\frac{\sqrt{3}}{2} & -\frac{1}{2} & 0 \\ 0 & 0 & 1 \end{bmatrix} \\ &= \begin{bmatrix} J - \frac{1}{2}A^{(xy)} & D - \frac{\sqrt{3}}{2}A^{(xy)} & 0 \\ -D - \frac{\sqrt{3}}{2}A^{(xy)} & J + \frac{1}{2}A^{(xy)} & 0 \\ 0 & 0 & J + A^{(z)} \end{bmatrix}, \end{aligned} \tag{2.29}$$

which is identical to the expression derived using the local coordinates. This method is much faster than the first one and should generally be preferred for model derivation.

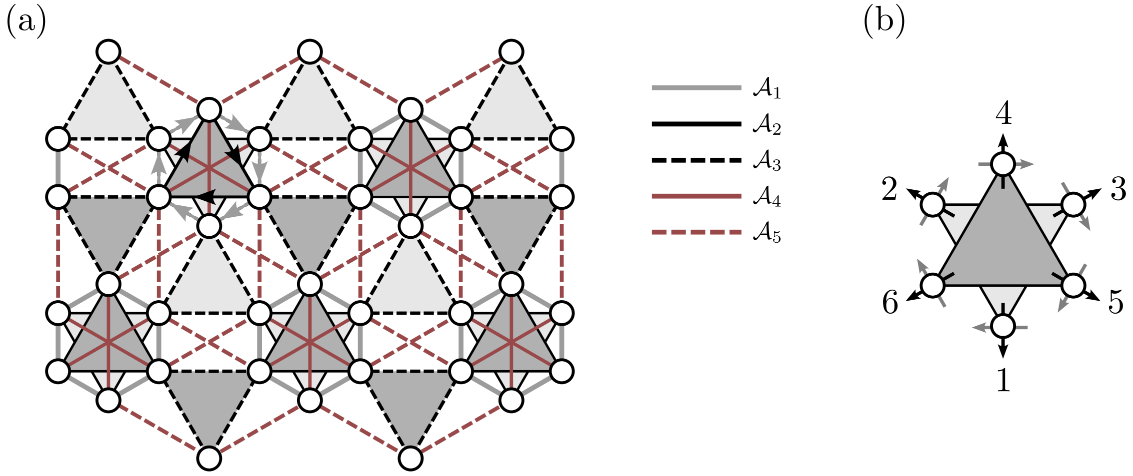

Figure 2.6: (a) Interaction pathways in AB-SKL. The $\mathcal{A}_k$ label the set of parameters $\{J_k, D_k, A_k^{(xy)}, A_k^{(z)}\}$. In the absence of breathing anisotropy, the dashed lines become identical to the solid lines of the same color. The arrows in the top right corner indicate the DM pathways, corresponding to the same sign of D_1 (grey) and D_2 (black). (b) Local anisotropic axes. The numbers indicate the indices we assign to each sublattice atom and the grey and black arrows represent $\hat{\mathbf{n}}_{ix}$ and $\hat{\mathbf{n}}_{iy}$ respectively.

2.5 Final Hamiltonian

Having demonstrated the method, we now apply the same principles to other bonds, assuming a general structure with potentially non-zero breathing anisotropy[6], mentioned in Sec. 1.3. Under these assumptions, we calculate invariants up to 5th neighbours: NN inter-layer (index 1), NN intra-layer (intra-cell - index 2, inter-cell - index 3), and next-nearest neighbours (NNN) (intra-cell - index 4, inter-cell - index 5). Fig. 2.6 (a) further illustrates these interaction pathways. In a compact form, the Hamiltonian reads

---

[6] The effects of breathing anisotropy will not be explored in this work. However, we will keep the discussion general, to make it more useful for future studies.

$$\mathcal{H} = \mathcal{H}_J + \mathcal{H}_D + \mathcal{H}_A + \mathcal{H}_K, \tag{2.30}$$

$$\mathcal{H}_J = \frac{1}{2}\sum_{\mathbf{r}\mathbf{r}'}\sum_{ij} J_{ij}(\mathbf{r}-\mathbf{r}')\mathbf{S}_i(\mathbf{r})\cdot\mathbf{S}_j(\mathbf{r}'), \tag{2.31}$$

$$\mathcal{H}_D = \frac{1}{2}\sum_{\mathbf{r}\mathbf{r}'}\sum_{ij} D_{ij}(\mathbf{r}-\mathbf{r}')\hat{\mathbf{z}}\cdot\left[\mathbf{S}_i(\mathbf{r})\times\mathbf{S}_j(\mathbf{r}')\right], \tag{2.32}$$

$$\mathcal{H}_A = \frac{1}{2}\sum_{\mathbf{r}\mathbf{r}'}\sum_{ij}\sum_{\alpha} A_{ij}^{(\alpha)}(\mathbf{r}-\mathbf{r}')\left(\hat{\mathbf{n}}_{i\alpha}\cdot\mathbf{S}_i(\mathbf{r})\right)\left(\hat{\mathbf{n}}_{j\alpha}\cdot\mathbf{S}_j(\mathbf{r}')\right), \tag{2.33}$$

$$\mathcal{H}_K = \sum_{\mathbf{r}}\sum_{i}\sum_{\alpha} K_\alpha\left(\hat{\mathbf{n}}_{i\alpha}\cdot\mathbf{S}_i(\mathbf{r})\right)^2, \tag{2.34}$$

where we recall that $\mathbf{r}$ and $\mathbf{r}'$ label the unit cell positions, while i and j label the positions of the sublattice atoms inside the unit cells. Note that the sums run over all sites, and the factors of $1/2$ in eqs. (2.31 - 2.33) are used to prevent double-counting.

Regular exchange interactions are always allowed by symmetry on every bond in the system because these interactions are completely invariant with respect to all spin rotations and reflections. This isotropic character also reflects the fact that exchange interactions have purely electronic origins and do not depend on the SOC (see Sec. 1.1.1).

The DM interactions are non-zero for the intra- and inter-layer NN bonds (indices 1-3) and zero otherwise (DM interactions on NNN bonds cancel because they pass through the inversion centre). One can verify that the form of the DM vector automatically satisfies Moriya's rules (see Sec. 1.2.2). Although DM interactions originate from the SOC, the anisotropy is weak, since these couplings preserve the in-plane rotational symmetry, as mentioned in Sec. 2.4.2.

Finally, for all types of neighbours considered in the derivation, there are non-zero anisotropic exchange interactions. We use $A_{ij}^{(y)} = -A_{ij}^{(x)} = A_{ij}^{(xy)}$ as in the derivation in the previous section. The vectors $\hat{\mathbf{n}}_{i\alpha}$ represent the local anisotropy axes (see fig. 2.6 (b)), and can be written as

$$\hat{\mathbf{n}}_{ix} = \begin{bmatrix}\cos\alpha_i\\ \sin\alpha_i\\ 0\end{bmatrix}, \hat{\mathbf{n}}_{iy} = \begin{bmatrix}-\sin\alpha_i\\ \cos\alpha_i\\ 0\end{bmatrix}, \hat{\mathbf{n}}_{iz} = \begin{bmatrix}0\\ 0\\ 1\end{bmatrix}, \tag{2.35}$$

where

$$\alpha_i = \frac{\pi l_i}{3}, \tag{2.36}$$

with

$$\{l_1, l_2, l_3, l_4, l_5, l_6\} = \{3, 1, 5, 0, 4, 2\}. \tag{2.37}$$

These vectors are also used to define the single-ion anisotropy (SIA), $\mathcal{H}_K$ in eq. (2.34). The allowed couplings of spin components on the same site can be derived using the same methods described in the previous section, where instead of bond point group one would be dealing with the site point group (which also happens to be C_{2v} in the AB-SKL). We note that the number of the SIA parameters can be reduced using the spherical representation of the spins

$$\mathbf{S}_i(\mathbf{r}) = \begin{bmatrix} \cos\big(\theta_i(\mathbf{r})\big)\sin\big(\phi_i(\mathbf{r})\big) \\ \sin\big(\theta_i(\mathbf{r})\big)\sin\big(\phi_i(\mathbf{r})\big) \\ \cos\big(\phi_i(\mathbf{r})\big) \end{bmatrix}, \tag{2.38}$$

and the definition of the local axes in eq. (2.35), such that

$$\begin{aligned}\sum_\alpha K_\alpha \left(\hat{\mathbf{n}}_{i\alpha}\cdot\mathbf{S}_i(\mathbf{r})\right)^2 &= K_x \cos^2(\theta_i(\mathbf{r})-\alpha_i)\sin^2(\phi_i(\mathbf{r})) \\ &+ K_y \cos^2(\theta_i(\mathbf{r})-\alpha_i)\sin^2(\phi_i(\mathbf{r})) \\ &+ K_z \cos^2(\phi_i(\mathbf{r})) \\ &= K_y + \bar{K}_x \cos^2(\theta_i(\mathbf{r})-\alpha_i)\sin^2(\phi_i(\mathbf{r})) + \bar{K}_z\cos^2(\phi_i(\mathbf{r})),\end{aligned} \tag{2.39}$$

where $\theta_i(\mathbf{r})$ and $\phi_i(\mathbf{r})$ are the spherical angles, $\bar{K}_x = K_x - K_y$ and $\bar{K}_z = K_z - K_y$. We see that the normalization constraint on the spin variables leaves only two independent SIA parameters. Therefore, in the remainder of this work, we will set $K_y = 0$.

While the out-of-plane anisotropy preserves rotational symmetry in the xy-plane, the in-plane anisotropic interactions reduce these continuous symmetries down to the discrete rotations of the point group. For this reason, we will refer to models with the in-plane anisotropic interactions as “strong SOC” cases.

2.6 Summary of important results and open questions

In this chapter, we demonstrated in a pedagogical manner the procedure of symmetry-based derivation of magnetic Hamiltonian for AB-SKL. The results of this derivation were published in Ref. [75]. Note that the original derivation, presented in the supplemental material of this reference, made use of concepts from group theory, which contrasts the simplified approach presented here. Although previous studies [71–73, 90–92] have discussed some of the terms in the model (2.30), the analysis in Ref. [75] was the first work to identify all allowed quadratic spin invariants. In doing so, we have demonstrated that the intra-layer DM interactions can only have a DM vector oriented along the $\hat{\mathbf{z}}$-axis. This contrasts the results in Ref. [71], which included a second type of DM interactions with the DM vectors lying parallel to the kagome plane. Importantly, the analysis above revealed that the NN inter-layer bonds may also host DM interactions, which has not been discussed in any of the previous literature. These inter-layer DM couplings will be shown to host a wide range of phenomena in the later chapters. Lastly, the derivation has identified the anisotropic exchange interactions, which have been excluded from all previous models of AB-SKL. The effects of these interactions may be non-negligible in some compounds, since the systems like Mn_3X have been previously experimentally shown to have a considerable magnetic anisotropy (see Chapter 6).

Having established the general model here, it would be interesting to investigate how the changes in symmetry modify the spin interactions. For example, at the surface, the symmetry is reduced, because the operations that interchange the A and B layers are no longer valid symmetry operations. As a result, the number of spin invariants will increase and the model will include terms that couple the planar and z-components of spins. The surface effects are important for the studies of thin magnetic films, which can be grown at the facilities in Dalhousie University.

Chapter 3

Self-duality transformations

> Nothing in physics seems so hopeful as the idea that it is possible for a theory to have a high degree of symmetry that was hidden from us in everyday life.
>
> Steven Weinberg

In the previous chapter, Sec. 2.4, we demonstrated two methods for extending the spin invariants on a single bond to other bonds in the same family. The first method, involving a change to local coordinates, may seem unnecessarily convoluted, considering simple rotations are able to achieve equivalent results. However, in the process of defining bond invariants in local coordinates, we accidentally stumbled onto a very interesting property: the local terms $\widetilde{H}_{ij}^{(1,\ldots,4)}$ had exactly the same form as the global invariants $H_{ij}^{(1,\ldots,4)}$, despite describing very different interactions (recall that the global coupling constants were defined as linear combinations of the local ones). This equivalence is called the *self-duality*[1] of the Hamiltonian.

Self-duality and symmetry transformations have a lot in common, since both types of operations describe some form of invariance of a given model. However, self-duality should be viewed as a generalization of symmetry, since it maps one set of parameters of the model to another, whereas a symmetry leaves it unchanged. Nevertheless, the existence of self-duality has important consequences on the physical properties of the corresponding model. For example, notice that if we treat the local and global coupling constants as independent parameters and set them equal to the same values

---

[1] By *self*-duality, we imply a transformation that maps a model consisting of some number of interactions into itself, without producing any new interactions. In this way, a symmetry is a trivial self-duality, since it leaves the model unchanged.

(*i.e.* $\widetilde{J} = J = J_0$, $\widetilde{D} = D = D_0$, $\dots$), the energy would be exactly the same. Notably, the local transformations change the spin structure of the system, thus mapping between different magnetic phases. Therefore, self-duality transformations describe hidden symmetries of the parameter space, which leave the energy unchanged, while modifying the spin structure.

Self-duality has played an significant role in statistical physics, an important example being a Kramers-Wannier duality that relates the ordered and paramagnetic phases in the two-dimensional Ising model on a square lattice [93–98]. Another famous example is the duality of electromagnetic fields, which is a consequence of the Lorentz symmetry of the Maxwell equations [99]. More recently, self-duality transformations have gained some interest in the studies of strongly anisotropic magnets, mostly in the context of the Kitaev systems [100–102]. In 2D kagome systems, Essafi and Jaubert used self-duality maps to study the emergent chiral spin liquids at the points of accidental symmetry [31, 32]. Note that some sources also refer to these transformations as spin gauge transformations [103, 104]. However, up to date, no formal description of emergent self-dualities exists for generic magnetic systems. The task of developing a general formalism for self-duality is an ambitious endeavour, and we will not pursue it here. Nevertheless, we will describe some of the self-duality transformations for the AB-SKL and approximately relate them to the strength of the SOC. The last section will be dedicated to the properties and applications of self-duality.

3.1 Conditions for self-duality

To understand the origin self-duality in our model, we should go back to the definition of the local coordinates. In order to have self-duality, in addition to eqs. (2.17 - 2.19), we must ensure that

$$\mathcal{H}\bigg(\Big\{\boldsymbol{\mathcal{A}}_{ij}(\mathbf{r}-\mathbf{r}');\mathbf{S}_i(\mathbf{r})\Big\}\bigg) = \mathcal{H}\bigg(\Big\{\widetilde{\boldsymbol{\mathcal{A}}}_{ij}(\mathbf{r}-\mathbf{r}');\widetilde{\mathbf{S}}_i(\mathbf{r})\Big\}\bigg), \tag{3.1}$$

where the model is written explicitly in terms of the elements of the coupling matrices $\boldsymbol{\mathcal{A}}_{ij}(\mathbf{r}-\mathbf{r}')$ and spin variables, which could either be in a local or global form. In the following, for the sake of compactness, we will abbreviate the coupling constants to $\boldsymbol{\mathcal{A}}_{ij}$, *i.e.* we will omit the unit cell positions. Eq. (3.1) essentially ensures that the local and global invariants are equivalent on every bond. The process for finding self-dualities then consists of the following steps:

1. Select a local coordinate frame using eq. (2.17). In principle, the transformation matrices can be further generalized by allowing them to be different for different unit cells ($\mathbf{R}_i \rightarrow \mathbf{R}_i(\mathbf{r})$), but this will not be done in this work for the sake of simplicity. We constrain the local transformation matrices to be real and orthogonal, in order to preserve the magnitude of the spin vectors.

2. Calculate the new bond coupling matrices using the inverse of eq. (2.19).

3. Solve eq. (3.1) to find the local transformations that correspond to the self-duality. In principle, this procedure could be performed numerically, in which case we would iterate through steps 2 and 3 while adjusting the local transformations until convergence is achieved.

We will demonstrate this procedure on the magnetic model in eq. (2.30) starting with only exchange interactions (*i.e.* no SOC), then adding the DM interactions and out-of-plane anisotropy (weak-SOC limit), and, finally, including the in-plane anisotropy.

Before proceeding, it is important to mention the uniqueness of duality transformations. Consider local transformation matrices $\mathbf{R}_i$ and $\mathbf{R}_j$. Consider also a symmetry transformation described by matrix $\mathbf{M}$. We can define new local transformations $\bar{\mathbf{R}}_i = \mathbf{R}_i\mathbf{M}$ and $\bar{\mathbf{R}}_j = \mathbf{R}_j\mathbf{M}$. Then

$$\begin{aligned}\widetilde{\boldsymbol{\mathcal{A}}}_{ij} &= \mathbf{R}_i\boldsymbol{\mathcal{A}}_{ij}\mathbf{R}_j^T \\ &= \mathbf{R}_i(\mathbf{M}\boldsymbol{\mathcal{A}}_{ij}\mathbf{M}^T)\mathbf{R}_j^T \\ &= \bar{\mathbf{R}}_i\boldsymbol{\mathcal{A}}_{ij}\bar{\mathbf{R}}_j^T, \end{aligned} \tag{3.2}$$

where in the second line we used the fact that the coupling matrix is invariant under the symmetry transformation $\mathbf{M}$. Hence, if the local transformations describe a self-duality, we can construct new local matrices using the symmetries of the Hamiltonian that describe the same self-duality. This allows us some freedom to select the exact form of the local transformations.

3.2 Isotropic limit

The simplest form of the magnetic model only includes exchange interactions, $\mathcal{H} = \mathcal{H}_J$. Then, all bond coupling matrices have the same form:

$$\boldsymbol{\mathcal{A}}_{ij} = \begin{bmatrix} J_{ij} & 0 & 0 \\ 0 & J_{ij} & 0 \\ 0 & 0 & J_{ij} \end{bmatrix} = J_{ij}\mathbb{I}, \tag{3.3}$$

where $\mathbb{I}$ is the identity matrix. Eqs. (2.19) and (3.1) imply that

$$\begin{aligned} \widetilde{\boldsymbol{\mathcal{A}}}_{ij} &= \mathbf{R}_i \boldsymbol{\mathcal{A}}_{ij} \mathbf{R}_j^T \\ &= J_{ij} \mathbf{R}_i \mathbf{R}_j^T \\ &= \widetilde{J}_{ij}\mathbb{I}, \end{aligned} \tag{3.4}$$

which suggests that $\mathbf{R}_i\mathbf{R}_j^T = r_{ij}\mathbb{I}$, such that $\widetilde{J}_{ij} = r_{ij}J_{ij}$, where r_{ij} is a constant. Since the transformation matrices are orthogonal, the only possible values for r_{ij} are ± 1. If $r_{ij} = 1$, then the matrices are identical, $\mathbf{R}_i = \mathbf{R}_j$, and correspond to a symmetry transformation, leaving the model unchanged. Therefore, the only possibility for self-duality is when $r_{ij} = -1$, or, equivalently,

$$\mathbf{R}_i = -\mathbf{R}_j. \tag{3.5}$$

Note that $\mathbf{R}_i$ can be any orthogonal matrix, so we can choose it to be the identity matrix. The only way to satisfy condition in eq (3.5) on every bond is if the underlying lattice consists of two independent sublattices. If this is the case, then we can assign the local transformations to be $\mathbb{I}$ for one sublattice, and $-\mathbb{I}$ for the other.

This is not possible for a 2D kagome lattice, and therefore it does not have the exchange self-duality. However, in the AB-SKL we have A and B sublattices, which allows us to define $\mathbf{R}_i = g_i\mathbb{I}$, where

$$g_i = \begin{cases} 1, & \text{if } i = 1,2,3, \\ -1 & \text{if } i = 4,5,6, \end{cases} \tag{3.6}$$

we get a map between models with positive and negative inter-layer exchange parameters:

$$\gamma : \begin{cases} J_{1,4,5} & \longrightarrow -J_{1,4,5} \\ J_{2,3} & \longrightarrow J_{2,3}. \end{cases} \tag{3.7}$$

This self-duality can be interpreted in two ways. First, assume that we know the spin structure that is stabilized by some set of parameters. When all out-of-plane coupling constants change sign, the new spin structure can be obtained by simply flipping the spins on the B (or A) layers. We will refer to the structures related via self-duality as *dual images*. Dual images are extremely useful for constructing phase diagrams: once the stability regions of a phase are known, we can apply self-duality transformations to obtain the phase boundaries of the dual images. The converse is also true: when the spins on either A or B layers are flipped (for any spin configuration), the corresponding energy change comes from the inter-layer couplings changing sign.

Although these properties might seem trivial, they demonstrate the usefulness of self-duality. Regardless of the number of model parameters, as long as they are of the same type[2], the duality transformations will remain valid.

3.3 Weak-SOC limit

It was mentioned in Sec. 2.5 that the DM as well as the out-of-plane anisotropic interactions (which includes both anisotropic exchange and SIA) are invariant under rotations of spins around the z-axis. Since in this case the SOC-induced interactions do not break continuous rotational symmetry, we will refer to this type of spin symmetry as the weak-SOC limit. The out-of-plane spin rotations change these interactions and are no longer valid symmetry operations of the system. Let's consider a coupling matrix of the form

---

[2] More precisely, the interactions must have the same symmetry properties. In the first example, exchange interactions were shown to be invariant under arbitrary orthogonal transformations. Anisotropic interactions reduce this symmetry, and can therefore introduce new self-duality transformations.

$$\boldsymbol{\mathcal{A}}_{ij} = \begin{bmatrix} J_{ij} & D_{ij} & 0 \\ -D_{ij} & J_{ij} & 0 \\ 0 & 0 & J_{ij} + A_{ij}^{(z)} \end{bmatrix}, \tag{3.8}$$

where in the special case of $i = j$ we can take

$$\boldsymbol{\mathcal{A}}_{ii} = \begin{bmatrix} 0 & 0 & 0 \\ 0 & 0 & 0 \\ 0 & 0 & K_z \end{bmatrix}. \tag{3.9}$$

The block-diagonal structure of eq. (3.8) suggests that we should have separate local spin transformations for the in-plane and out-of-plane spin components. The corresponding general transformation matrix is also block-diagonal:

$$\mathbf{R}_i = \begin{bmatrix} R_i^{(xx)} & R_i^{(xy)} & 0 \\ R_i^{(yx)} & R_i^{(yy)} & 0 \\ 0 & 0 & R_i^{(zz)} \end{bmatrix}. \tag{3.10}$$

In order for this matrix to be orthogonal, we must enforce that both blocks are independently orthogonal, meaning that $R_i^{(zz)} = \pm 1$. Since the z-components transform independently from the in-plane ones, we can study them independently of each other. To simplify the discussion, we will consider the transformation of the in-plane components first. The most general 2×2 orthogonal matrix is

$$\mathbf{R}_i = \begin{bmatrix} \varepsilon_i \cos(\theta_i) & -\varepsilon_i \sin(\theta_i) \\ \sin(\theta_i) & \cos(\theta_i) \end{bmatrix}, \tag{3.11}$$

where $\varepsilon_i, \varepsilon_j = \pm 1$. Applying this transformation to the top block of eq. (3.8) gives

$$\widetilde{\boldsymbol{\mathcal{A}}}_{ij} = \begin{bmatrix} J_{ij}\varepsilon_i\varepsilon_j \cos(\theta_{ij}) + D_{ij}\varepsilon_i\varepsilon_j \sin(\theta_{ij}) & -J_{ij}\varepsilon_i \sin(\theta_{ij}) + D_{ij}\varepsilon_i \cos(\theta_{ij}) \\ J_{ij}\varepsilon_j \sin(\theta_{ij}) - D_{ij}\varepsilon_j \cos(\theta_{ij}) & J_{ij} \cos(\theta_{ij}) + D_{ij} \sin(\theta_{ij}) \end{bmatrix}, \tag{3.12}$$

where $\theta_{ij} = \theta_i - \theta_j$. To ensure the self-duality, we must set $\varepsilon_i = \varepsilon_j = \varepsilon$. The equations for the dual exchange and DM coupling constants are then

$$\widetilde{J}_{ij} = J_{ij}\cos\big(\theta_{ij}\big) + D_{ij}\sin\big(\theta_{ij}\big) \tag{3.13}$$

$$\widetilde{D}_{ij} = -J_{ij}\sin\big(\theta_{ij}\big) + D_{ij}\varepsilon\cos\big(\theta_{ij}\big). \tag{3.14}$$

Next, we have to make sure that the local coupling constants are the same on each bond. Let us consider the constraints imposed on the angles θ_i by the NN inter- and intra-layer interactions. In order for the inter-layer constants to be the same, we set

$$\widetilde{J}_1 = \widetilde{J}_{16} = \widetilde{J}_{62} = \widetilde{J}_{24} = \widetilde{J}_{43} = \widetilde{J}_{35} = \widetilde{J}_{51}, \tag{3.15}$$

$$\widetilde{D}_1 = \widetilde{D}_{16} = \widetilde{D}_{62} = \widetilde{D}_{24} = \widetilde{D}_{43} = \widetilde{D}_{35} = \widetilde{D}_{51}. \tag{3.16}$$

Similarly, for the intra-layer interactions we equate

$$\widetilde{J}_2 = \widetilde{J}_{12} = \widetilde{J}_{23} = \widetilde{J}_{31} = \widetilde{J}_{45} = \widetilde{J}_{56} = \widetilde{J}_{56}, \tag{3.17}$$

$$\widetilde{D}_2 = \widetilde{D}_{12} = \widetilde{D}_{23} = \widetilde{D}_{31} = \widetilde{D}_{45} = \widetilde{D}_{56} = \widetilde{D}_{56}. \tag{3.18}$$

We obtain

$$\theta_1 - \theta_6 = \theta_6 - \theta_2 = \theta_2 - \theta_4 = \theta_4 - \theta_3 = \theta_3 - \theta_5 = \theta_5 - \theta_1, \tag{3.19}$$

$$\theta_1 - \theta_2 = \theta_2 - \theta_3 = \theta_3 - \theta_1 = \theta_4 - \theta_5 = \theta_5 - \theta_6 = \theta_6 - \theta_4. \tag{3.20}$$

These constraints are satisfied if $\theta_i = m\alpha_i$, where m is an integer and α_i are defined in eq. (2.36). With these angles, we obtain self-duality maps

$$\mu_m^{(\varepsilon)} : \begin{cases} J_1 & \longrightarrow J_1\cos\big(\frac{\pi m}{3}\big) + D_1\sin\big(\frac{\pi m}{3}\big), \\ D_1 & \longrightarrow -J_1\sin\big(\frac{\pi m}{3}\big) + D_1\varepsilon\cos\big(\frac{\pi m}{3}\big), \\ J_{2,3} & \longrightarrow J_{2,3}\cos\big(\frac{2\pi m}{3}\big) + D_{2,3}\sin\big(\frac{2\pi m}{3}\big), \\ D_{2,3} & \longrightarrow -J_{2,3}\sin\big(\frac{2\pi m}{3}\big) + D_{2,3}\varepsilon\cos\big(\frac{2\pi m}{3}\big), \\ J_{4,5} & \longrightarrow (-1)^m J_{4,5}. \end{cases} \tag{3.21}$$

Returning now to the out-of-plane components, the local transformation reads

$$\widetilde{A}_{ij}^{(zz)} = r_{ij}^{(z)} \left(J_{ij} + A_{ij}^{(zz)} \right) - \widetilde{J}_{ij} \tag{3.22}$$

$$\widetilde{K}_z = r_{ij}^{(z)} K_z, \tag{3.23}$$

where $r_{ij}^{(z)} = R_i^{(z)} R_j^{(z)}$. Here, the expression for $\widetilde{J}_{ij}$ is determined by the in-plane transformation in eq. (3.21). Following similar arguments as for exchange, we can write the complete the self-duality maps above:

$$\mu_m^{(\varepsilon,\zeta)} : \begin{cases} J_1 & \longrightarrow J_1 \cos\!\left(\frac{\pi m}{3}\right) + D_1 \sin\!\left(\frac{\pi m}{3}\right), \\ D_1 & \longrightarrow -J_1 \sin\!\left(\frac{\pi m}{3}\right) + D_1 \varepsilon \cos\!\left(\frac{\pi m}{3}\right), \\ J_{2,3} & \longrightarrow J_{2,3} \cos\!\left(\frac{2\pi m}{3}\right) + D_{2,3} \sin\!\left(\frac{2\pi m}{3}\right), \\ D_{2,3} & \longrightarrow -J_{2,3} \sin\!\left(\frac{2\pi m}{3}\right) + D_{2,3} \varepsilon \cos\!\left(\frac{2\pi m}{3}\right), \\ J_{4,5} & \longrightarrow (-1)^m J_{4,5}, \\ A_1^{(z)} & \longrightarrow \zeta A_1^{(z)} + J_1 \left(\zeta - \cos\!\left(\frac{\pi m}{3}\right)\right) - D_1 \sin\!\left(\frac{\pi m}{3}\right), \\ A_{2,3}^{(z)} & \longrightarrow \zeta A_{2,3}^{(z)} + J_{2,3} \left(\zeta - \cos\!\left(\frac{2\pi m}{3}\right)\right) - D_{2,3} \sin\!\left(\frac{2\pi m}{3}\right), \\ A_{4,5}^{(z)} & \longrightarrow \zeta A_{4,5}^{(z)} + J_{4,5} \left(\zeta - (-1)^m\right), \\ K_z & \longrightarrow \zeta K_z, \end{cases} \tag{3.24}$$

where $\zeta = \pm 1$. Although the transformation of the z-components of spins is necessary to make the self-duality maps exact, we will show that most magnetic structures in AB-SKL are planar, with spins lying in the kagome planes. Therefore, the maps defined in eq. (3.21) are often sufficient to describe all necessary properties. The corresponding local coordinate frames are shown in fig. 3.1. Note that the integer m characterizes a discrete "winding number" around a fictitious hexagon formed by the xy-positions of the sublattice atoms. On the other hand, the role of the value of ε can be understood by considering the $\mu_0^{(-1,+1)}$ self-duality. The only coupling constants that change under this transformation are the DM parameters, which simply flip the sign. In matrix form, this transformation is equivalent to a mirror symmetry, which explains why it affects the DM interactions. For these reasons, we can view ε as the chirality control parameter.

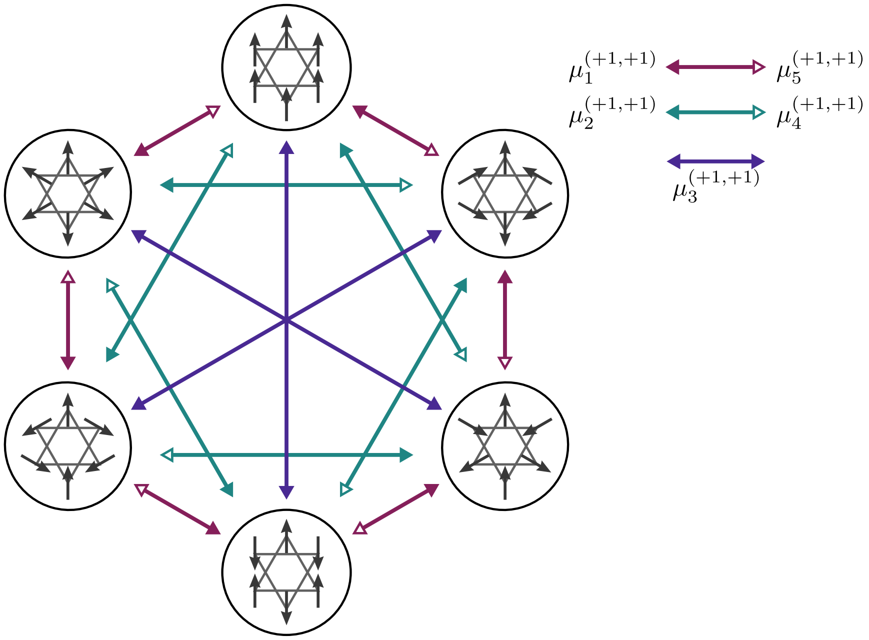

Figure 3.1: An illustration of the $\mu_m^{(+1,+1)}$ self-dualities in the weak-SOC limit. The configurations represent the local coordinate frames, where for the sake of simplicity we only show the local y-axes. The z coordinates point out-of-plane, and the local x-axes can be obtained using the right-hand rule on each site. From the top of the diagram, the winding number starts at zero, and increases by integer increments going counter-clockwise. Application of the $\mu_m^{(+1,+1)}$ transformation is equivalent to moving m steps around the diagram in the counter-clockwise direction.

3.4 Strong-SOC limit

Finally, when we include the in-plane anisotropy, the system loses all continuous rotational symmetries. To indicate this, we will refer to this situation as the strong-SOC limit. Nevertheless, the coupling matrices $\boldsymbol{\mathcal{A}}_{ij}$ remain block-diagonal, and we can still use matrices of the type (3.10) to derive the self-duality transformations.

So far, we have been lucky to have relatively simple equations that constrain the local transformation matrices in order to yield self-duality. The calculations presented in the last section were considerably longer that those for the exchange interactions, but were still tractable. Here, our luck somewhat runs out, since in order to explicitly derive the allowed self-duality transformations for the most general case of the coupling matrix requires a significantly longer analysis. Most of the matrix transformations that result from this analysis have already been derived in the previous section: these correspond to maps $\mu_0^{(+1,\zeta)}$, $\mu_1^{(-1,\zeta)}$, $\mu_3^{(+1,\zeta)}$, $\mu_4^{(-1,\zeta)}$:

$$\mu_0^{(+1,\zeta)}, \mu_4^{(-1,\zeta)} : \begin{cases} A_1^{(xy)} & \longrightarrow \quad A_1^{(xy)}, \\ A_{2,3}^{(xy)} & \longrightarrow \quad A_{2,3}^{(xy)}, \\ A_{4,5}^{(xy)} & \longrightarrow \quad A_{4,5}^{(z)}, \\ K_x & \longrightarrow \quad K_x, \\ K_y & \longrightarrow \quad K_y, \end{cases} \tag{3.25}$$

$$\mu_1^{(-1,\zeta)}, \mu_3^{(+1,\zeta)} : \begin{cases} A_1^{(xy)} & \longrightarrow -A_1^{(xy)}, \\ A_{2,3}^{(xy)} & \longrightarrow \quad A_{2,3}^{(xy)}, \\ A_{4,5}^{(xy)} & \longrightarrow -A_{4,5}^{(xy)}, \\ K_x & \longrightarrow \quad K_x. \end{cases} \tag{3.26}$$

The remaining self-duality transformation corresponds to a global 90-degree rotation around the z-axis:

$$\mathbf{R}_\eta = \begin{bmatrix} 0 & \mp 1 & 0 \\ \pm 1 & 0 & 0 \\ 0 & 0 & 1 \end{bmatrix}, \tag{3.27}$$

which flips the sign of the in-plane anisotropic interactions:

$$\eta : \begin{cases} A_1^{(xy)} & \longrightarrow -A_1^{(xy)}, \\ A_{2,3}^{(xy)} & \longrightarrow -A_{2,3}^{(xy)}, \\ A_{4,5}^{(xy)} & \longrightarrow -A_{4,5}^{(xy)}, \\ K_x & \longrightarrow -K_x. \end{cases} \tag{3.28}$$

The sign of the SIA parameters defines either the easy-axis ($K_\alpha < 0$), or easy-plane ($K_\alpha > 0$) anisotropy for each spin, while the sign of the anisotropic exchange selects the easy-axis for all spins globally. Thus, the self-duality maps above provide connections between phases with different easy-axes.

3.5 Summary of important results and open questions

In this chapter, we introduced self-duality transformations of the magnetic Hamiltonian in the isotropic, weak-, and strong-SOC settings. The derivation provided here can serve as a guide for identifying self-duality in other systems. Interestingly, we see that two limiting SOC cases (isotropic and strong) have fewer transformations than the weak-SOC case, where we get 24 different transformations. In comparison, in 2D kagome only two non-trivial self-duality transformations have been discussed [31, 32]. This illustrates how a simple AB-stacking of kagome layers enriches the magnetic properties of the system. The self-dual properties of AB-SKL demonstrate how changes in the local spin structure, such as winding or chirality, change the model parameters. The smallest number of self-dualities is found in the isotropic limit, where we have a single map $\gamma \equiv \mu_3^{(+1,-1)}$, which reflects the two-sublattice structure of the lattice and persists in all SOC limits.

Let us now conclude by discussing the applications and some unanswered questions regarding the origins of self-duality.

3.5.1 Applications of self-duality

So far, we have focused on deriving the possible self-duality maps but didn't really discuss why they are useful. A simple explanation of the usefulness of self-duality is that *it describes the symmetry of the parameter space.* Given a self-duality transformation, we can apply it to some spin configuration to obtain a new structure with exactly the same energy. Similarly, if we know that at a given point of the parameter space we have a certain ground state structure, we can change the parameters of the model according to a self-duality map and obtain the ground state configuration at this new point via the corresponding local transformation. As a result, self-duality maps are helpful for constructing ground state phase diagrams. By analyzing a small portion of the parameter space and characterizing a subset of phase pockets, we can obtain new phases by applying different self-duality transformations.

The power of self-duality extends far beyond our simple examples of ground state energies. Since the Hamiltonian is self-dual, most[3] properties of the system will

---

[3] There are small caveats that complicate this general discussion. For example, properties that

display the same duality. For example, it is not difficult to show that the self-duality extends to the partition function,

$$Z = \mathrm{Tr}\Big\{e^{-\beta\mathcal{H}}\Big\}, \tag{3.29}$$

where $\beta = \frac{1}{k_B T}$ is inverse temperature (scaled by Boltzmann constant), and the trace implies integration over all degrees of freedom. Therefore, self-duality extends to all of the thermodynamic properties of the system, which allows us to make very general statements about our model. Similarly, the discussion is not limited to the classical systems, since self-duality has been shown in the past to extend to quantum ground states [100, 102].

One of the most common applications of the self-duality is in identifying points of accidental degeneracy. For example, consider applying the self-duality maps on the NN antiferromagnetic kagome model. By the conservation properties, the new points with potentially non-zero anisotropic interactions will also have ground states with macroscopic degeneracy, which may host exotic quantum phases [31]. Another interesting consequence of this is that a fully anisotropic system may develop accidental rotational symmetry, leading to zero-energy excitations, the so-called “pseudo-Goldstone” modes [102].

From an experimental point of view, knowledge of potential self-duality transformations is important when comparing the experimental data to theoretical predictions. Because the measured experimental properties may possess self-duality, several different sets of parameters could produce identical fits to a theoretical model. A case of this has already been reported for an inelastic neutron scattering experiment of a Kitaev system [105]. The solution in this situation is to add constraints to the fit based on other experimental observations that directly sample the local structure (*e.g.* elastic neutron scattering).

---

depend on the local spin structure (such as magnetization) are not generally preserved by the self-duality transformations. Another example is spin dynamics, where the local transformations must preserve the “right-handedness” of the coordinate frames in order to map the dynamics of one structure onto another. In general, these constraints need to be worked out for specific applications. However, in most cases, a lot of the self-duality properties extend to the properties of interest, making these transformations extremely useful.

3.5.2 Improvements of the derivation method

The main disadvantage of the method that we used to determine the possible self-duality transformations is efficiency: for a more complicated system it might not be possible to make good predictions about the correct form of the local transformation matrices. This issue can be resolved by automating the procedure using numerical programs, where the initially random matrices are modified until they satisfy eq. (3.1). Similar algorithms have been proposed for Kitaev systems [100]. However, although the numerical approach would be more thorough, it may be more difficult to gain insight about the bigger picture.

The self-duality transformations derived here were included in Ref. [80]. In the article, the derivation approach is different and is more focused on the connections between the *effective spin symmetry* and self-duality. By the effective spin symmetry we refer to the spin-only transformations that we may have in a system in addition to the space-group symmetries. For example, in the isotropic limit, we gain a full rotational spin symmetry, while in the weak-SOC limit it is reduced to only the axial rotations. These additional symmetries have important effects on the mathematical structure of the symmetry groups, which manifest in different *irreducible representations* (irreps) of these groups. Irreps provide a connection between the abstract symmetry operations and the transformations acting directly on a physical system. It turns out, that the number and type of the irreps in a group is closely related to the number of possible self-duality transformations [80]. However, the details of this derivation require a more sophisticated group-theoretical treatment and are not yet completely general. Obtaining a general connection between the symmetry and self-duality is an important challenge that would help with the characterization of novel systems and could potentially answer some of the long-standing questions, such as origins of accidental degeneracy.

Chapter 4

Monte Carlo simulations

> You insist that there is something a machine cannot do. If you tell me precisely what it is a machine cannot do, then I can always make a machine which will do just that.
>
> John von Neumann

Most modern problems in physics (and, generally, in science) revolve around some form of complexity, which arises from interactions between many[1] variables (objects or bodies). In a great majority of cases, this complexity makes analytical calculations extremely difficult, and often impossible[2]. In this regard, the advances in computational sciences have allowed us to circumvent this problem by studying the many-body problems numerically.

Monte Carlo (MC) methods are a class of algorithms, which use random sampling in order to make numerical estimations of unknown quantities. Since the first applications of computation to physical problems, MC methods have quickly become a widely used technique in physics used to calculate various statistical properties [106, 107]. In this chapter we will review basic principles of MC simulations and introduce the common algorithms used to study continuous spin systems.

---

[1] In physics tradition, the counting generally goes as *one, two, many, infinite.*

[2] The two ends of the spectrum (*i.e. one-* and *infinite*-body problems) usually correspond to the simplest cases, which have been studied for decades, while in the best case scenario, the *two*-body problem is barely solvable. The remaining cases are either impossible to solve or 1) can be shown to be exactly equivalent to the *one*/*infinite*-object problem; 2) have been solved by a frighteningly gifted individual with the help of an obscure field of mathematics, such that the proof would require other scholars more than four years to decipher [94].

4.1 Basic ideas

To start, let the state of a magnetic system be completely determined by the orientations of N normalized spin vectors. In this way, a point in the configuration space can be written as $\nu = \big(\mathbf{S}(\mathbf{r}_1), \mathbf{S}(\mathbf{r}_2), \ldots, \mathbf{S}(\mathbf{r}_N)\big)$. As the directions of the spins in the system fluctuate at some temperature T, ν traces a trajectory in the configuration space, $\nu(t)$, where t represents a time measure. Alternatively, t may label different states of the system, prepared under the same conditions (same model parameters and temperature). The physical properties of the system will change as the trajectory progresses, and the average of some property $G_\nu = G\big(\mathbf{S}(\mathbf{r}_1), \mathbf{S}(\mathbf{r}_2), \ldots, \mathbf{S}(\mathbf{r}_N)\big)$ over the spin configurations visited during a trajectory with τ steps is

$$\langle G \rangle_\tau = \frac{1}{\tau} \sum_{t=1}^{\tau} G_{\nu(t)}. \tag{4.1}$$

The true average of this property is given by $\langle G \rangle = \lim_{\tau \to \infty} \langle G \rangle_\tau$. This limit is taken in order for the sampled distribution to properly account relative frequencies with which different configurations are visited. This is the foundation of MC simulations: the properties of the system are estimated by averaging over a large number of randomly generated system configurations.

In order for the MC method to be useful, however, we must address several issues. Firstly, in order for the states in $\nu(t)$ to be representative of the statistical distribution, we must ensure that the evolution of the trajectory is *ergodic*, *i.e.* that the system can reach every state in the configuration space given enough time. This can be achieved by generating a random configuration at every new step. However, even in the simplest case of binary (Ising) spins, the number of possible configurations increases exponentially with increasing system size and quickly becomes astronomically large, making the straightforward sampling of these states impractical. In models with continuous degrees of freedom, the number of states is, by definition, infinite. For this reason, MC algorithms are designed such that the sampling of new configurations is biased towards the states that are statistically important. This *importance sampling* strategy allows us to make good estimates of physical properties by sampling only a small fraction of the total number of configurations.

In many cases, we are interested in sampling the properties of a system in thermal equilibrium. A sufficient requirement for the existence of stationary equilibrium is the so-called *detailed-balance* condition, which requires that a transition from a configuration ν to a different configuration μ is reversible, or

$$p_\nu P_{\nu\to\mu} = p_\mu P_{\mu\to\nu}, \tag{4.2}$$

where p_ν is the probability of a given state ν, and $P_{\nu\to\mu}$ is the probability of a transition from ν to μ. In thermal equilibrium, the probability distributions are given by the Boltzmann distribution:

$$p_\nu = \frac{e^{-\beta E_\nu}}{Z}, \tag{4.3}$$

where $\beta = \frac{1}{k_B T}$ is inverse temperature (scaled by Boltzmann constant), E_ν is the energy of the configuration, and Z is the partition function:

$$Z = \sum_\nu e^{-\beta E_\nu}. \tag{4.4}$$

Eq. (4.2) can be rearranged to read

$$\frac{P_{\nu\to\mu}}{P_{\mu\to\nu}} = \frac{p_\mu}{p_\nu} = e^{-\beta(E_\mu - E_\nu)} = e^{-\beta\Delta E_{\nu\mu}}. \tag{4.5}$$

A given MC algorithm is then determined by a particular form of the transition probability. The two most common algorithms used for studying spin systems are the *Metropolis* and the *heat-bath* algorithms.

4.2 Metropolis algorithm

Metropolis algorithm [106, 107] was developed in the early days of computer simulations, and it remains one of the most ubiquitous and robust numerical methods in scientific computing. The transition probability is defined in a piece-wise form:

$$P_{\nu\to\mu} = \begin{cases} 1, & \Delta E_{\nu\mu} \le 0, \\ \exp\bigl(-\beta\Delta E_{\nu\mu}\bigr), & \Delta E_{\nu\mu} > 0. \end{cases} \tag{4.6}$$

At each step, the orientation of a randomly chosen spin is modified and the resulting

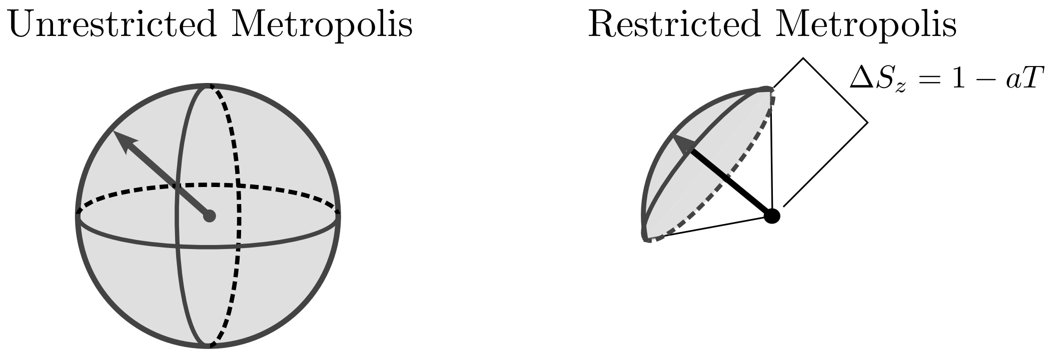

Figure 4.1: Unrestricted and restricted Metropolis steps. The current spin orientation is indicated by the black arrow. In the unrestricted case, the new orientation is sampled uniformly on the unit sphere, resulting in a large number of discarded configurations at low temperatures. On the other hand, in the restricted move scheme, the sampling is restricted to a section of the sphere bounded by the base of the cone, centred around the current spin orientation. The height of the cone is chosen to be $\Delta S_z = 1 - aT$, where $a \sim 1$ is a simulation parameter. At low temperatures, the base of the cone shrinks, leading to higher acceptance rate.

configuration is accepted with probability $P_{\nu \to \mu}$. The Metropolis method for a single MC step is given in algorithm 1 in the Appendix B.

This algorithm works well for systems with one-dimensional spin vectors (*e.g.* Ising model), but becomes less efficient for continuous degrees of freedom, especially at lower temperatures. The reason for this is that at low temperatures the probability of large spin fluctuations becomes very small, and therefore most of the proposed configurations are discarded. The situation can be improved by implementing a restricted-step update [108], whereby a selected spin is rotated within a cone with a given width, as in fig. 4.1. The width of the cone can then be parameterized such that it would monotonically decrease with the decreasing temperature. This restricted update procedure has been shown to be extremely effective in simulations of frustrated XY and Heisenberg models [21].

4.3 Heat-bath algorithm

Heat-bath sampling [109] further improves the sampling statistics by generating new spin orientations from the probability distribution

$$P\left(\mathbf{S}'(\mathbf{r}); \mathbf{H}(\mathbf{r})\right) = \frac{e^{\beta \mathbf{S}'(\mathbf{r}) \cdot \mathbf{H}(\mathbf{r})}}{\int \mathrm{d}\mathbf{S}'(\mathbf{r}) e^{\beta \mathbf{S}'(\mathbf{r}) \cdot \mathbf{H}(\mathbf{r})}} = \frac{e^{\beta \mathbf{S}'(\mathbf{r}) \cdot \mathbf{H}(\mathbf{r})}}{C(\mathbf{r})}, \tag{4.7}$$

where $H_\alpha(\mathbf{r}) = -\frac{\partial \mathcal{H}}{\partial S_\alpha(\mathbf{r})}$ is the effective field acting on spin at site $\mathbf{r}$. In the following, we drop the site labels for clarity. Note that $\mathbf{S}' \cdot \mathbf{H} = H\cos\theta$, such that

$$C = \int_0^{2\pi} \mathrm{d}\phi \int_0^{\pi} \mathrm{d}\theta \sin\theta e^{\beta H \cos\theta} = \frac{4\pi \sinh(\beta H)}{\beta H}, \tag{4.8}$$

where $H = |\mathbf{H}|$, and θ is the angle between $\mathbf{H}$ and $\mathbf{S}'$. The probability distribution can be written in terms of two independent distributions, $P(\phi)$ and $P(\cos\theta)$:

$$P(\phi) = \frac{1}{2\pi}, \tag{4.9}$$

$$P(\cos\theta) = \frac{\beta H e^{\beta H \cos\theta}}{2\sinh(\beta H)}, \tag{4.10}$$

$$P\left(\mathbf{S}'; \mathbf{H}\right) = P(\phi)P(\cos\theta). \tag{4.11}$$

For any random variable x with probability distribution $P(x)$, the cumulative distribution function $F(x')$ represents the probability of choosing the value of x to be less than or equal to x':

$$F(x') = \int_{-\infty}^{x'} \mathrm{d}x P(x). \tag{4.12}$$

For $P(\phi)$ and $P(\cos\theta)$ Eq. (4.12) becomes

$$F(\phi) = \frac{1}{2\pi}\int_0^{\phi} \mathrm{d}\phi' = \frac{\phi}{2\pi} = r_1, \tag{4.13}$$

$$F(\cos\theta) = \frac{\beta H}{2\sinh(\beta H)} \int_{-1}^{\cos\theta} \mathrm{d}\cos\theta' e^{\beta H \cos\theta'} = \frac{e^{\beta H\cos\theta} - e^{-\beta H}}{2\sinh(\beta H)} = r_2. \tag{4.14}$$

When r_1 and r_2 are uniformly distributed on $[0,1)$, the equations above translate into

$$\phi = 2\pi r_1, \tag{4.15}$$

$$\cos\theta = 1 + \frac{1}{\beta H} \ln\left(r_2 + (1-r_2)e^{-2\beta H}\right). \tag{4.16}$$

Thus, by generating two random numbers, r_1 and r_2, it is possible to determine the new orientation of spin $\mathbf{S}(\mathbf{r})$ with respect to its effective field $\mathbf{H}(\mathbf{r})$. This procedure is summarized in algorithm 2 in the Appendix B.

At low temperatures, the exponential term vanishes leading to

$$\cos\theta \approx \frac{1}{\beta H}\ln(r_2). \tag{4.17}$$

This simplified equation can be used to speed up the program at low temperatures (since we do not have to calculate computationally "expensive" exponential functions). However, one should be cautious of numerical errors at very small values of ${r_2}^3$.

The heat-bath algorithm works well for the continuous spin systems, where the ground state has zero-energy excitations (*i.e.* the Goldstone modes). Crucially, the closed form solutions of the integrals in (4.8) and (4.14) above depend on the fact that the effective field on a given site is independent of the orientation of the spin on the same site. When this condition is not satisfied (for example in a system with non-zero SIA), the algorithm can lead to significant errors,[4] and thus Metropolis algorithm should be used instead.

4.4 Microcanonical updates

Although the heat-bath algorithm improves the sampling at low temperatures in models with continuous degrees of freedom, the system may still get stuck in a single state. Physically speaking, at low temperatures the dominant spin excitations (spin waves), are the small-frequency Goldstone modes, which correspond to zero-energy global spin rotations. To improve the sampling and allow the system to explore a larger portion of the phase space, we can introduce intermediate *microcanonical* updates, *i.e.* updates that do not change the energy of the system.

Note that we may write a spin vector $\mathbf{S}(\mathbf{r})$ in terms of components parallel and perpendicular to the local field $\mathbf{H}(\mathbf{r})$:

$$\mathbf{S}(\mathbf{r}) = S_{\parallel}(\mathbf{r})\hat{\mathbf{s}}_{\parallel}(\mathbf{r}) + S_{\perp}(\mathbf{r})\hat{\mathbf{s}}_{\perp}(\mathbf{r}), \tag{4.18}$$

where

---

[3] When $\beta H \leq 0.2$, eq. (4.17) is valid for $r_2 \geq 5 \times 10^{-5}$.

[4] For example, if the SIA coefficient is positive (easy-plane anisotropy) the heat-bath algorithm defined here will tend to maximize the energy, instead of minimizing it.

$$S_{\parallel}(\mathbf{r})\hat{\mathbf{s}}_{\parallel}(\mathbf{r}) = \frac{\mathbf{S}(\mathbf{r}) \cdot \mathbf{H}(\mathbf{r})}{H^2(\mathbf{r})}\mathbf{H}(\mathbf{r}). \tag{4.19}$$

Since the perpendicular component of the spin $S_{\perp}(\mathbf{r})\hat{\mathbf{s}}_{\perp}(\mathbf{r})$ does not contribute to the dot product, it also does not contribute to the energy of the system. Therefore, a rotation of spin around its local field does not cost any energy. A microcanonical move may then consist of such a rotation, according to the Landau-Lifshitz dynamic equation:

$$\frac{d}{dt}\mathbf{S}(\mathbf{r}) = \mathbf{H}(\mathbf{r}) \times \mathbf{S}(\mathbf{r}). \tag{4.20}$$

This microcanonical update is often referred to as over-relaxation method [107, 110]. In order to move the system away from the current configuration, each update should rotate the spin by 180 degrees around the local field, which corresponds to flipping the sign of the perpendicular spin component. Thus, the new value of spin is

$$\begin{aligned}
\mathbf{S}'(\mathbf{r}) &= S_{\parallel}(\mathbf{r})\hat{\mathbf{s}}_{\parallel}(\mathbf{r}) - S_{\perp}(\mathbf{r})\hat{\mathbf{s}}_{\perp}(\mathbf{r}) \\
&= 2S_{\parallel}(\mathbf{r})\hat{\mathbf{s}}_{\parallel}(\mathbf{r}) - \mathbf{S}(\mathbf{r}) \\
&= \frac{2\mathbf{S}(\mathbf{r}) \cdot \mathbf{H}(\mathbf{r})}{H^2(\mathbf{r})}\mathbf{H}(\mathbf{r}) - \mathbf{S}(\mathbf{r}),
\end{aligned} \tag{4.21}$$

where $\mathbf{S}(\mathbf{r})$ and $\mathbf{S}'(\mathbf{r})$ represent the old and new orientations of the spin[5].

Over-relaxation method is deterministic and therefore should be applied in combination with algorithms discussed above (Metropolis or heat-bath) in order to produce a valid canonical distribution. Typically, one performs a single (stochastic) update of the system, followed by several (5-10) microcanonical updates of the lattice (see Algorithm 3 in Appendix B). This strategy is often used when studying complicated structures in continuous models, where the system tends to get stuck in local minima [21, 111, 112].

---

[5] As before, one should be cautious in applying this method when the model includes the SIA interactions.

Chapter 5

Ground state phase diagrams

> If people do not believe that mathematics is simple, it is only because they do not realize how complicated life is.
>
> John von Neumann

Having determined the symmetry allowed magnetic interactions in the AB-SKL, we can now explore the magnetic ground state structures that these couplings stabilize. As there are many parameters in the model (2.30), it makes sense to start the analysis with a simplified model and then gradually add other interactions. From this point on, we also ignore the breathing anisotropy by setting $\mathcal{A}_3 = \mathcal{A}_2$ and $\mathcal{A}_5 = \mathcal{A}_4$, where $\mathcal{A}_k = \{J_k, D_k, A_k^{(xy)}, A_k^{(z)}\}$ is a shortened representation of the coupling matrices $\mathcal{A}_{ij}(\mathbf{r}-\mathbf{r}')$, and k denotes the k^{th} neighbours. We will explore the properties of our model by starting with an isotropic limit (exchange only) and then "turning on" the SOC and considering the weak (DM and out-of-plane anisotropy) and strong (in-plane anisotropy) limits.

5.1 Methods

5.1.1 Details of the MC simulations

In the following, we will present the ground state phase diagrams, obtained from low-temperature MC simulations, discussed in Chapter 4[1]. To reduce the total number

---

[1] In principle, the task of obtaining the ground state of the model is a simple energy minimization problem. The stochastic nature of the MC methods allows them to more effectively avoid local energy minima and converge to the true ground state of the system. However there is no numerical method that would guarantee a convergence to a global minimum, and MC may fail in cases where the energy landscape has many local minima with similar energies (see Sec. 5.2).

of parameters, we set $|J_2| = 1$. This defines the energy scale of the system and we redefine the Hamiltonian and the temperature as $\mathcal{H} = \mathcal{H}/|J_2|$ and $T = k_B T/|J_2|$ (*i.e.* also setting $k_B = 1$). In all cases, we cooled down the system down to $T = 10^{-6}$ and used $\sim 10^4$ MC heat-bath updates per temperature to ensure convergence to the global energy minimum. We also considered systems with L^3 unit cells with L as small as 6 and as large as 18 to account for a large number periodic structures.

For most phase diagrams, we used the self-duality properties discussed in Chapter 3, to reduce the simulation time. The boundaries and structures of the dual phases were verified by additional numerical calculations and were always in perfect agreement with the ones obtained via the self-dual transformations.

5.1.2 Tools for identifying distinct magnetic phases

Even with the help of self-duality maps, an extensive description of the parameter phase space requires a large number of simulations. To characterize the ground state phase pockets, we perform scans along one or two parameters at a time, generating data for each point of the discretized parameter space. This leads to a very large amount of data (thousands of spin structures), which often corresponds to only a few distinct phases. Furthermore, the spin configurations are often periodic, meaning that storing the full spin structure is often unnecessary.

To resolve these issues, we choose a set of representative quantities that help us to identify the phase boundaries. The simplest such quantity is the ground state energy $E(\mathcal{A}_k)$. The ground state energy is continuous at the boundary of two phases, but its derivatives with respect to the parameters, $\frac{\partial E}{\partial \mathcal{A}_k}$ often become discontinuous at these points[2]. Note that if the change in the spin structure is continuous, one might require higher order derivatives of energy to identify the transition boundary. To extract the useful information about the spin structure, we calculate the Fourier transform of the form

---

[2] Consider a square lattice model with NN exchange interactions defined by a coupling constant J. For $J < 0$ ($J > 0$) the ground state is ferromagnetic (antiferromagnetic) with ground state energy $E_g = -2|J|N$. The E_g is a continuous function of J, while $\frac{\partial E_g}{\partial J} = -2N\text{sgn}(J)$ has a discontinuity at $J = 0$.

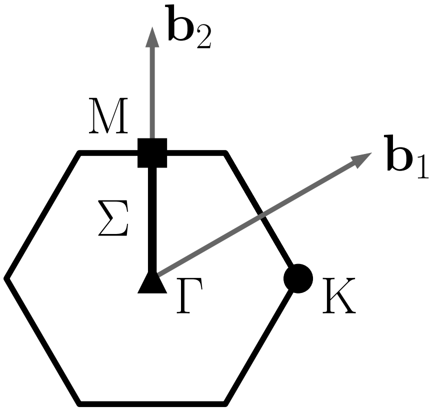

Figure 5.1: First Brillouin zone of the hexagonal lattice. The arrows represent the reciprocal lattice vectors $\mathbf{b}_1$ and $\mathbf{b}_2$, while the markers denote the relevant high-symmetry points. The bold black line from Γ to M point represents one of the six Σ lines.

$$\mathbf{S}_i(\mathbf{q}) = \frac{1}{\sqrt{N}} \sum_{\mathbf{r}} \mathbf{S}_i(\mathbf{r}) e^{-i\mathbf{q}\cdot\mathbf{r}}, \tag{5.1}$$

where the sum is over the Bravais lattice vectors (see Sec. 2.3), N is the total number of unit cells, and $\mathbf{q}$ are the points in the reciprocal space. From these, we calculate the effective[3] structure factor

$$\mathcal{S}(\mathbf{q}) = \frac{1}{6} \sum_i |\mathbf{S}_i(\mathbf{q})|^2, \tag{5.2}$$

where the prefactor of the sum represents dividing by the number of sublattices. If the configuration is periodic, $\mathcal{S}(\mathbf{q})$ will consist of one or several[4] delta functions or *magnetic Bragg peaks* at wavevectors $\mathbf{Q}_i$ lying in the first Brillouin zone, which is shown in fig. 5.1.

Therefore, in a given MC simulation, we calculate $\mathcal{S}(\mathbf{q})$, and then identify and store the positions and the values of its maxima. These quantities are used to identify

---

[3] The true structure factor is calculated as $\mathcal{S}(\mathbf{q}) = \frac{1}{6}\sum_{ij} \mathbf{S}_i(\mathbf{q}) \cdot \mathbf{S}_j(-\mathbf{q}) e^{-i\mathbf{q}\cdot(\mathbf{r}_i - \mathbf{r}_j)}$. This equation takes into the account the magnetic form factor, which reflects the spin structure inside a single unit cell. However, this quantity is more cumbersome to calculate, and the periods become harder to extract.

[4] Since the spin vectors are real, the $\mathcal{S}(\pm\mathbf{Q})$ will have the same values. Therefore, generally, the magnetic structure factors are symmetric with respect to the origin of the Brillouin zone.

the phase boundaries and to choose the appropriate system size for spin structure identification.

5.1.3 Visualizing spin configurations

Real-space spin configurations often provide valuable information about the properties of the system. Nevertheless, in some cases, simply plotting a spin configuration does not provide enough information for identifying the hidden structural patterns. The key to a useful visualization of a spin structure is then to take advantage of colour in order to effectively highlight the most useful features of a given configuration. To achieve this, one must design a "filter" function that brings out the important details that characterize the structure. Unfortunately[5], there is no "universal" filter that yields helpful information for any given spin structure, and so engineering the effective visualization tools is often an empirical process, based on trial and error. However, there are two visualization methods that were designed and used extensively for studying the magnetic phases in AB-SKL, and which can in principle be employed in any system. To demonstrate the effectiveness of these methods, we will apply the different filters to a spin configurations of the Ising-like phase Λ_4, which will be introduced in the next section.

The first method consists of highlighting features defined globally for all spins. The simplest examples of these are the x, y, and z components of spin vectors defined with respect to global coordinates. Often, these filters fail to identify the global ordering pattern, but provide some information about the local structure (*e.g.* spin configurations inside individual unit cells). These filters are also useful for determining if the structure is collinear, coplanar, or non-coplanar. Fig. 5.2 (a) illustrates this for the Ising-like structure. We see that although highlighting the x and y components does not yield much useful information, the z-component filter reveals that the spins lie in the plane of the kagome layers. In some cases, it is also useful to set the colours to $\mathbf{S}(\mathbf{r}) \cdot \mathbf{S}(0)$ (or $\mathbf{S}_i(\mathbf{r}) \cdot \mathbf{S}_1(0)$ in systems with sublattices), which then represents spatial correlations.

---

[5] Or, probably, fortunately, since the diversity of structures brings out the beauty of a physical system.

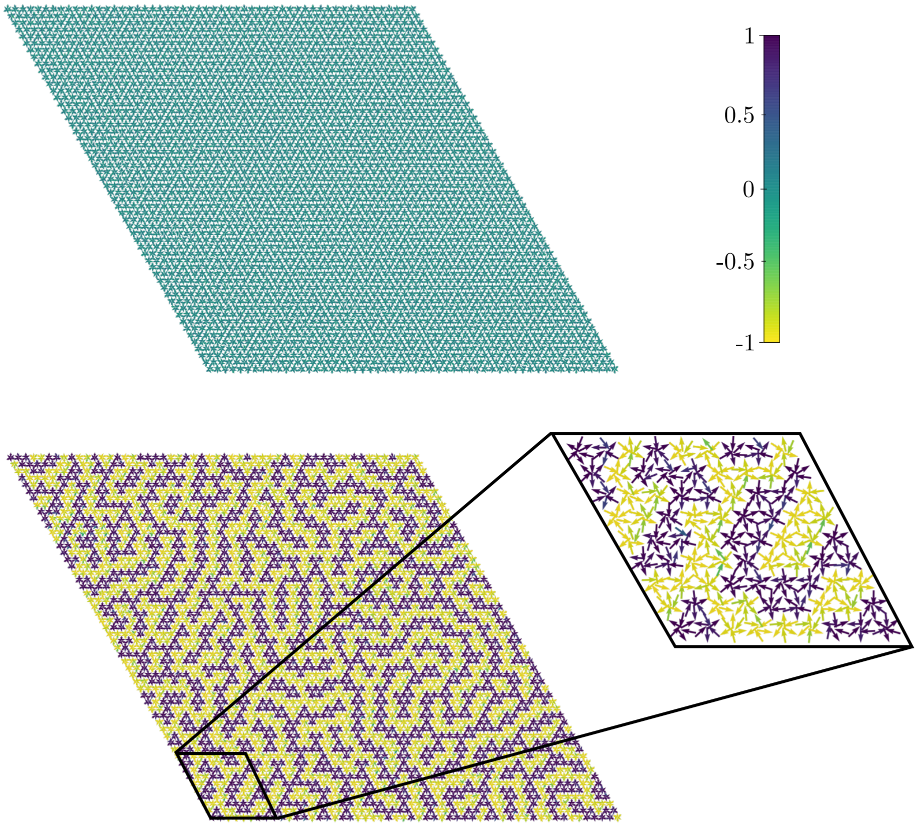

Figure 5.2: Designing filters to determine the structure of the $\mathbf{\Lambda}_4$ Ising-like phases. For all cases, the colours correspond to the values on the bar at the top right of the figure. (a) Highlighting the global z-components of spins reveals that they are uniformly zero, such that the structure lies in the plane of the kagome layers. (b) Ultimately, a filter of the form $\mathbf{S}_i(\mathbf{r}) \cdot \mathbf{S}_i(0)$, which discards the microscopic details of the intra-cell structure, is able to extract the unusual global structure, revealing non-periodic patterns.

The second method involves designing filters that highlight global features. In AB-SKL, and, more generally for systems with sublattices, the noisy details of the local structure are often easy to hide using the local anisotropic axes. However, an even simpler approach is to use $\mathbf{S}_i(\mathbf{r}) \cdot \mathbf{S}_i(0)$ function, which describes an overlap of spins on each site with spins on the same sublattice i in the 0^{th} unit cell. Although these types of correlations is blind to the structure inside of individual unit cells, it reveals the global variations going from one cell to the other. This is clearly demonstrated in fig. 5.2 (b), where the local filters reveal complicated spatial patterns.

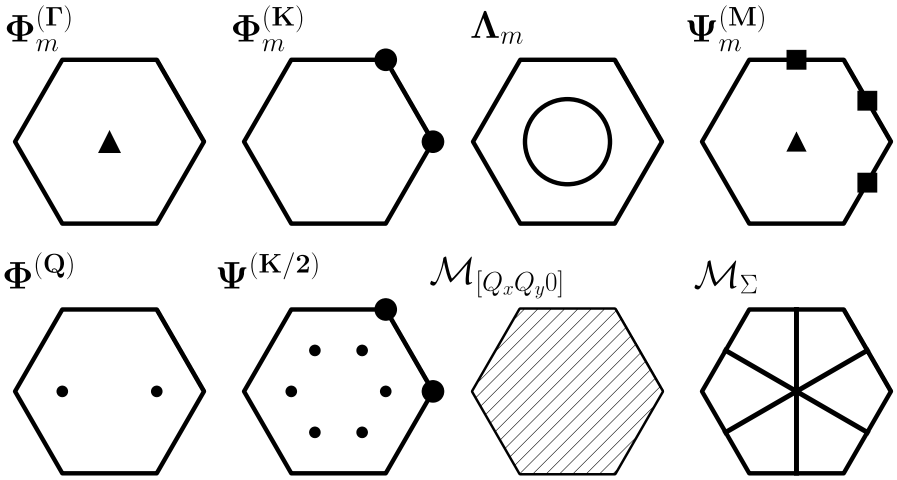

Figure 5.3: Sketches of the Fourier transforms of the spin configurations discussed in this chapter. The four most common phases are shown on the top row, while the less frequently occurring states are shown on the bottom. The markers represent Bragg peaks, solid lines in diagrams for $\mathbf{\Lambda}_m$ and $\mathcal{M}_{\Sigma}$ phases represent 1D degenerate manifolds, and the shaded Brillouin zone corresponding to the $\mathcal{M}_{[Q_xQ_y0]}$ represents a 2D degenerate manifold in the $Q_z = 0$ plane.

5.2 Magnetic structures

Before looking at the phase diagrams obtained by the MC simulations, it is worth describing the magnetic structures observed in our studies. As discussed in Chapter 3, the self-duality transformations provide mappings between phases with different spin structures. Since the weak-SOC limit provides the largest number of such mappings, and, as a result, the largest number of dual structures, it is convenient to present the magnetic phases observed in this limit as “basis” structures. The phases in the the decoupled and strong-SOC limits can then be described as linear combinations of these configurations.

The periodicity of a given magnetic structure is determined with respect to the underlying lattice. A spin configuration will either have the same period as the lattice, or form a *magnetic superlattice* with a period extending over several unit cells, or can even be incommensurate to the lattice period. As discussed before, the periodicity of a magnetic structure is captured by the Fourier transform of the magnetic structure. The Fourier transforms of all phases discussed below are presented in fig. 5.3. In these studies, all structures obtained in the numerical simulations have $Q_z = 0$, *i.e.* every

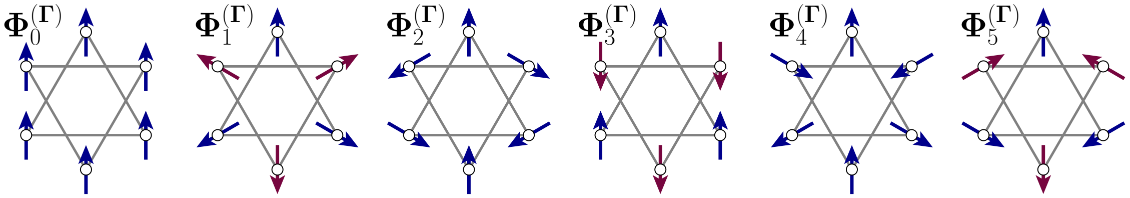

Figure 5.4: Spin structure of the $\mathbf{\Phi}_m^{(\mathbf{\Gamma})}$ phases. Red-coloured spins are used to indicate structures with antiferromagnetically stacked A and B triangles. Note that in the isotropic and weak-SOC limits, these structures are defined up to an arbitrary in-plane rotation.

AB bilayer appears exactly the same.

5.2.1 Q=Γ and Q=K structures

The simplest type of magnetic ordering corresponds to spin configurations with the same periodicity as the underlying lattice. Such structures have a single Bragg peak at $\mathbf{Q} = \Gamma$, which is at the center of the Brillouin zone. In this case, we only have to consider the possible structures on a single unit cell. In AB-SKL, all $\mathbf{Q} = \Gamma$ structures can be obtained by applying the $\mu_m^{(+1,+1)}$ self-duality maps from Sec. 3.3 to the ferromagnetic configurations where spins lie either parallel or perpendicular to the kagome planes. We label these as $\mathbf{\Phi}_m^{(\mathbf{\Gamma})}$ and present them in fig. 5.4. The

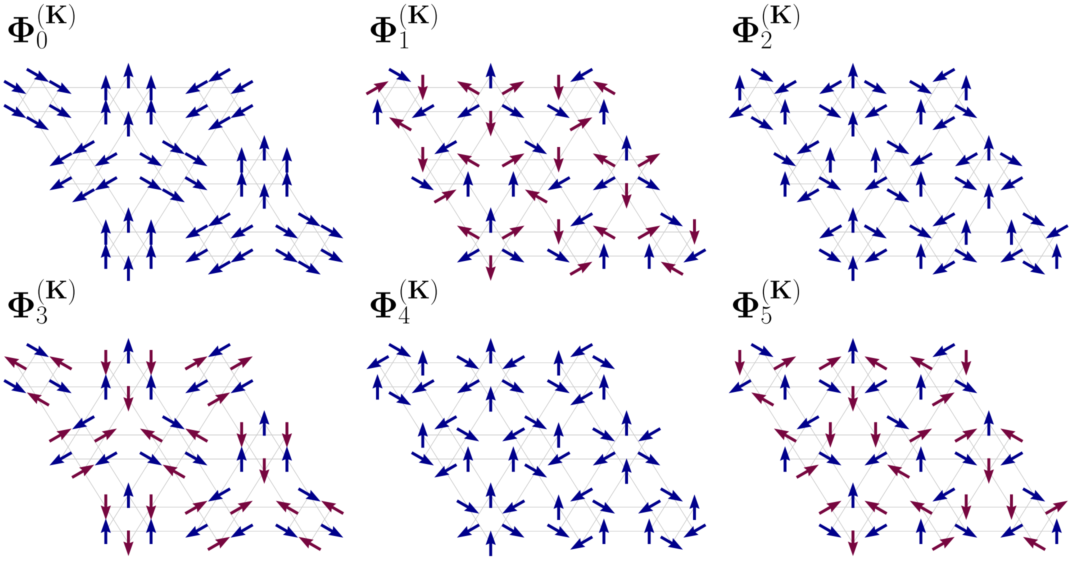

Figure 5.5: Spin structure of the $\mathbf{\Phi}_m^{(\mathbf{K})}$ phases. The colouring scheme is the same as in fig. 5.4.

meaning of the m-index is the same as in Sec. 3.3: it corresponds to the winding number around the hexagon. The $\mathbf{\Phi}_0^{(\mathbf{\Gamma})}$ and $\mathbf{\Phi}_3^{(\mathbf{\Gamma})}$ configurations are special because they are the only collinear structures (ferro- and antiferromagnetic, respectively). The remaining non-collinear configurations lie in the plane of the kagome layers and correspond to the 120 degree configurations on the A and B triangles stacked ferro- or antiferromagnetically.

The next set of magnetic phases consists of periodic structures described by $\mathbf{Q} =$ K, which lies on the corners of the Brillouin zone (fig. 5.3). These configurations have a period equal to three unit cells. However, the spin structure in each crystal unit cell is the same as in fig. 5.4 for $\mathbf{Q} = \Gamma$, except rotated by 120 degrees with respect to the spins in the neighbouring cells, as shown in fig. 5.5. To emphasize this similarity, we label these phases as $\mathbf{\Phi}_m^{(\mathbf{K})}$.

5.2.2 Ising-like structures

Another family of dual magnetic phases where at the level of individual unit cell the spin structure is approximately the same as $\mathbf{\Phi}_m^{(\mathbf{\Gamma})}$ describes Ising-like configurations, labelled generically as $\mathbf{\Lambda}_m$. Unlike $\mathbf{\Phi}_m^{(\mathbf{K})}$, these structures generally lack well-defined long-range order, but sometimes display stripe correlations, as shown in fig. 5.2 (b). Note that configurations with $m \neq 4$ are obtained by changing the unit cell sublattice spin structure to the corresponding order in fig. 5.4. The Fourier transform of an Ising-like structure is characterized by a ring of incommensurate wavevectors (fig. 5.3).

The disordered structure of the $\mathbf{\Lambda}_m$ phases is peculiar, and was proven to be difficult to study. Therefore we will dedicate Chapters 7 and 8 to the analytical and numerical analysis of these structures at finite temperatures.

5.2.3 Other magnetic structures

There are several other spin structures that are stabilized in certain regions of the parameter space, which we will briefly discuss here. Most of these phases are ordered and have well-defined periods. The most prominent of them are the **M-star** structures, where the spin configurations are defined by four Bragg peaks in the Brillouin zone: three at the distinct M points, and one at the Γ point, as shown in fig. 5.3. The spin

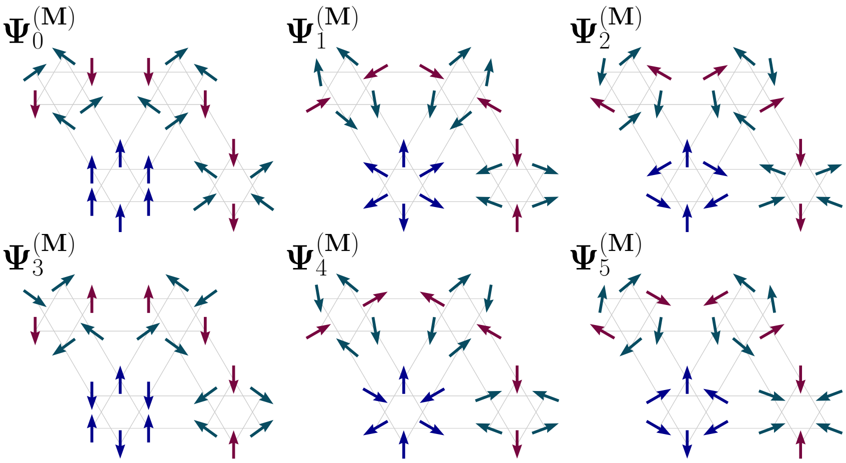

Figure 5.6: Spin structure of the $\mathbf{\Psi}_m^{(\mathbf{M})}$ phases. Different colours indicate spins related by the rotational symmetry.

configurations of these phases, labelled as $\mathbf{\Psi}_m^{(\mathbf{M})}$, are shown in fig. 5.6. The M-star configurations have been reported in other systems, including Kitaev-Heisenberg models on honeycomb lattice [113]. The $\mathbf{\Psi}_m^{(\mathbf{M})}$ are examples of the multiple-**Q** structures, since their Fourier transforms are defined by more than one inequivalent wavevectors. The most famous examples of multiple-**Q** configurations are the skyrmion textures[6], which are actively studied due to their topological properties [26, 27].

The remaining spin configurations appear very infrequently in our MC simulations, often close to the phase boundaries, where the energetic competitions are strongest. As a result, we will simply describe their Fourier structure, without going into details about the spin configurations. Here, we will give these structures a general labels that reflect their Fourier structure, but it is important to keep in mind that there are always dual copies of such phases in other parts of the parameter space.

Incommensurate single-Q structures. In typical helical magnets, the spins rotate throughout the lattice, forming wave-like patterns, characterized by a single **Q** vector.

---

[6] Categorizing skyrmions as multiple-**Q** structures remains controversial in the literature. Although a Fourier transform of a skyrmion lattice produces three inequivalent Bragg peaks, the defining property of skyrmions is their topology, characterized by a non-zero winding number [114]. Because not every triple-**Q** structure has non-trivial topology, skyrmions are often grouped separately. Since our discussion here does not concern topological textures, we consider all magnetic phases defined by multiple wavevectors to be multiple-**Q** configurations.

In a system with sublattice structure, the spins in a given unit cell can have more complicated arrangements, which then rotate as we go from one cell to the next. As already discussed for $\mathbf{\Phi}_m^{(\mathbf{K})}$, in AB-SKL we sometimes observe spatially non-uniform structures where in the individual unit cells the spin arrangements are identical to the $\mathbf{\Phi}_m^{(\mathbf{\Gamma})}$ structures. In $\mathbf{\Phi}_m^{(\mathbf{K})}$, the spatial patterns are commensurate, meaning that the period of the magnetic structure is an integer multiple of the crystal period, but in some rare cases we may also have incommensurate patterns, where the magnetic period is equal to a non-integer multiple of the crystal period. These structures are generally labelled as $\mathbf{\Phi}^{(\mathbf{Q})}$.

Multiple-Q structures. There is at least one other multiple-$\mathbf{Q}$ configuration that appears in our MC simulations: the $\frac{1}{2}$**K-star** structure, defined by Bragg peaks at the $\frac{1}{2}$K and K points. These phases are periodic in the kagome plane, with the period equal to six crystal unit cells. Similar to the M-star phases, we give these a general label $\mathbf{\Psi}^{(\mathbf{K/2})}$.

Degenerate ground state manifolds. There are two types of highly degenerate spin configurations, defined by a very large number of magnetic wavevectors. In the first case, all wavevectors $\mathbf{Q} = [Q_x, Q_y, 0]$ are degenerate, giving a 2D ground state manifold, similar to the antiferromagnetic kagome lattice. In the second case, the degeneracy occurs along the Γ-M lines (or Σ lines), producing a 1D ground state manifold. These are denoted as $\mathcal{M}_{[Q_xQ_y0]}$ and $\mathcal{M}_\Sigma$ respectively.

5.3 Isotropic limit

Since exchange interactions are always present in magnetic systems and are typically the largest contribution to the energy, an isotropic system is a reasonable starting point for the analysis of magnetic properties of AB-SKL. Ignoring the breathing anisotropy, we have three parameters: J_1, J_2, and J_4. Recall that for $J_1 = J_4 = 0$, the problem reduces to either ferromagnetic ($J_2 < 0$) or antiferromagnetic ($J_2 > 0$) decoupled kagome layers. Therefore, in fig. 5.7 we present the $J_1 - J_4$ phase diagrams for negative and positive values of J_2. Before discussing the structure of these diagrams, we note that they display the “inversion” symmetry, corresponding

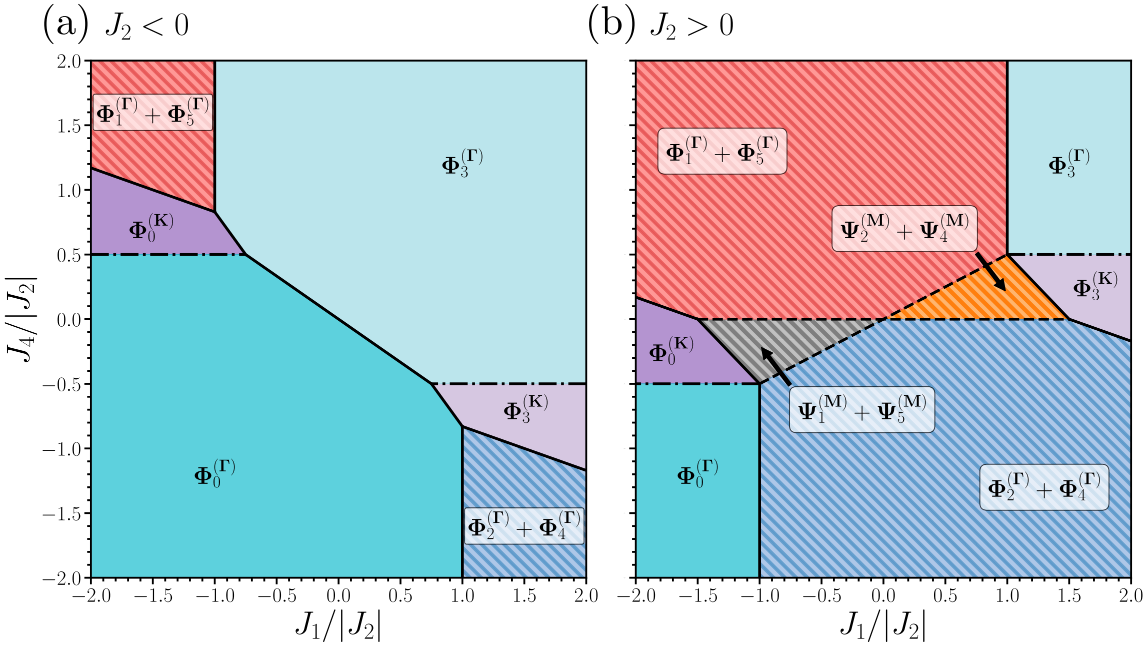

Figure 5.7: Magnetic phase diagrams of the AB-SKL in the isotropic limit. (a) and (b) correspond to ferromagnetic and antiferromagnetic intra-layer exchange (J_2) values. The stripy regions correspond to phases with mixed chirality, as discussed in the text. The dashed and dash-dotted lines correspond to the highly degenerate states $\mathcal{M}_\Sigma$ and $\mathcal{M}_{[Q_xQ_y0]}$, respectively.

to changing the signs of both J_1 and J_4. This is consistent with the γ self-duality, as derived in Sec. 3.2.

Since the AB-stacking results in two independent sublattices, the first effect that the inter-layer couplings have on the magnetic structure is fixing the relative ordering of the A and B layers (either ferromagnetic or antiferromagnetic). The simplest case correspond to the two possible collinear phases and occurs when J_1 and J_4 have the same sign and $J_2 < 0$ (fig. 5.7 (a)): the individual kagome planes realize ferromagnetic order and the A and B layers are either ferromagnetic $J_1, J_4 < 0$ or antiferromagnetic $J_1, J_4 > 0$, leading to $\mathbf{\Phi}_0^{(\mathbf{\Gamma})}$ and $\mathbf{\Phi}_3^{(\mathbf{\Gamma})}$ phases, respectively. When $J_2 < 0$ and the signs of the J_1 and J_4 are different, the system becomes frustrated and at large values of both inter-layer coupling constants, it stabilizes non-collinear 120 degree structures. Since the exchange interactions do not differentiate between the two types of chirality, we get degenerate $\mathbf{\Phi}_1^{(\mathbf{\Gamma})}$, $\mathbf{\Phi}_5^{(\mathbf{\Gamma})}$ states for ($J_1 < 0$, $J_4 > 0$), and $\mathbf{\Phi}_2^{(\mathbf{\Gamma})}$, $\mathbf{\Phi}_4^{(\mathbf{\Gamma})}$ states for ($J_1 > 0$, $J_4 < 0$). Interestingly, at intermediate values of J_1 and J_4 in the competing regime, the competitions "compromise" by stabilizing the period 3 structures $\mathbf{\Phi}_0^{(\mathbf{K})}$

and $\mathbf{\Phi}_3^{(\mathbf{K})}$. This compromise satisfies the J_1 and J_2 interactions, as well as the inter-cell J_4 interactions, but frustrates the intra-cell J_4 interactions.

When $J_2 > 0$ in the decoupled limit we realize a 120 degree state with macroscopic degeneracy. Inter-layer couplings generally remove this degeneracy, as seen from the phase diagram in fig. 5.7 (b). As in the previous case of the ferromagnetic J_2, for large values of the inter-layer couplings, the system stabilizes either collinear (if J_1 and J_4 have the same sign), or 120 degree (if J_1 and J_4 have different signs) spin structures. The more interesting phases occur for intermediate values of these couplings. From the phase diagram in fig. 5.7 (b) we see that when $-\frac{1}{2} \leq J_4 \geq \frac{1}{2}$, the system can stabilize the multiple-$\mathbf{Q}$ structures $\mathbf{\Psi}_m^{(\mathbf{M})}$ ($m \neq 0, 3$), or, like in the case of $J_2 < 0$, period 3 configurations $\mathbf{\Phi}_0^{(\mathbf{K})}$ and $\mathbf{\Phi}_3^{(\mathbf{K})}$. These results indicate that the degenerate ground state in the decoupled limit permits stabilization of complex phases when the system is further frustrated by the inter-layer couplings.

Before turning to anisotropic interactions, we note that it is still possible to obtain states with macroscopic ground state degeneracy in the stacked limit. These phases occur at certain phase boundaries, where the competitions between different interactions are strongest. For example, the boundaries between the $\mathbf{\Phi}_0^{(\mathbf{K})}$ ($\mathbf{\Phi}_3^{(\mathbf{K})}$) and $\mathbf{\Phi}_0^{(\mathbf{\Gamma})}$ ($\mathbf{\Phi}_3^{(\mathbf{\Gamma})}$) result in $\mathcal{M}_{[Q_xQ_y0]}$ states, where within each unit cell the spins are collinear to each other, with ferromagnetic (antiferromagnetic) inter-layer ordering. Another highly degenerate ground state occurs at the boundaries of the $\mathbf{\Psi}_m^{(\mathbf{M})}$ and the non-collinear $\mathbf{\Phi}_m^{(\mathbf{\Gamma})}$ phases. In these cases, the spin configurations correspond to the 120 degree structures in each unit cell and display degeneracy along the Σ lines in the Brillouin zone, leading to the $\mathcal{M}_\Sigma$ ground state. These states should be of interest for potential realizations of the exotic spin liquid phases in 3D kagome materials, but further analysis is required to fully understand their properties in the AB-SKL systems.

5.4 Weak-SOC limit

Next, we would like to go from the fully isotropic to the weak-SOC limit, which preserves the axial rotations around the z-axis. In principle, this lets us introduce the DM, as well as the z-component SIA and anisotropic exchange interactions. In practice, however, this creates too many free parameters, making the exploration of

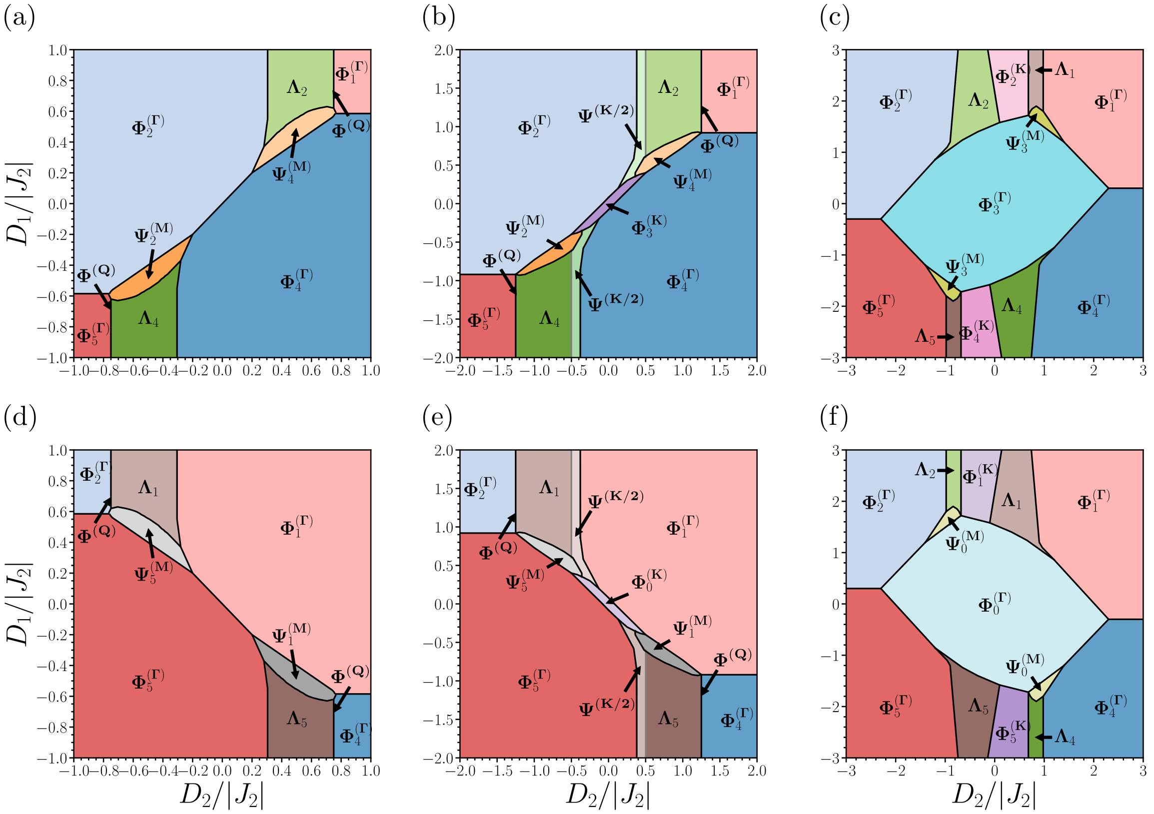

Figure 5.8: Examples of magnetic phase diagrams of the AB-SKL in the weak-SOC limit. The exchange parameters used to construct these diagrams were (written in the form $(J_1,\ J_2)$): (a) (1,1), (b) (1.6,1), (c) (0.5,-1), (d) (-1,1), (e) (-1.6,1), and (f) (-0.5,-1).

the parameter space intractable. From the preliminary calculations we were able to conclude that the SIA and the anisotropic exchange interactions lead to very similar effects and generally only induce trivial changes of the spin structure. Therefore, we focus in this section only on the effects of the D_1 and D_2 interactions. To simplify matters even further, we fix the value of $J_4 = 0$, since it produces most of the expected phases.

The resulting $D_1 - D_2$ phase diagrams are shown in fig. 5.8. There are a few general remarks that can be made about all of these diagrams. First, note that there is again an "inversion" symmetry in each diagram, which this time changes the signs of the DM constants. This comes as a result of the $\mu_0^{(-1,+1)}$ self-duality map, which reverses the chirality of the spin structures. Furthermore, comparing figs. 5.8 (a)-(c) and (d)-(f), we still see the manifestation of the $\gamma = \mu_3^{(+1,+1)}$ self-duality, originating from the sign reversal of J_1. Second, note that since the DM interactions select configurations with specific chirality, there is no longer ambiguity between the structures with $m = 1, 5$ or $m = 2, 4$. In fact, we see that when the magnitudes of both D_1 and D_2 are large, the ground state is always a non-collinear $\mathbf{Q} = \Gamma$ state, where the sign of D_1 determines if the ordering of the A and B triangles is ferromagnetic or antiferromagnetic, while the sign of D_2 specifies the chirality of the 120 degree structure. However, it is the intermediate values of these coupling constants that seem to stabilize the more complicated magnetic structures.

The DM interactions in AB-SKL systems result in a number of complex phases, some of which we have already observed in the isotropic limit: these are the commensurate $\mathbf{\Phi}_m^{(\mathbf{K})}$ and $\mathbf{\Psi}_m^{(\mathbf{K})}$ phases. However, specific to the competitions between the exchange and DM couplings are the unusual $\mathbf{\Lambda}_m$ structures. Depending on the strength of the exchange, these phases are typically stabilized at intermediate values of D_2 and extend to very large (or even indefinite) magnitudes of D_1. We will provide a more detailed discussion of the properties of these phases in Chapters 7 and 8. Close to the phase boundaries of the $\mathbf{\Lambda}_m$ phases we often find other interesting phases. For example, the $\mathbf{\Phi}^{(\mathbf{Q})}$ are stabilized at the boundary of $\mathbf{\Phi}_5^{(\mathbf{\Gamma})}$ and $\mathbf{\Lambda}_4$ (fig. 5.8 (a), (b), (d), (f)), while $\mathbf{\Psi}^{(\mathbf{K}/2)}$ are found in small regions between $\mathbf{\Lambda}_4$ and $\mathbf{\Phi}_4^{(\mathbf{\Gamma})}$ (as well as the equivalent dual phase boundaries). This rich phase behaviour further indicates strong competitions as a result of high geometric frustration and DM interactions.

The last thing that is worth addressing is the effects of the DM interactions on the collinear phases, *i.e.* when $J_2 < 0$ (figs. 5.8 (c), (f)). Note that it takes very large values of DM constants to suppress the collinear structure. Since the energy of the collinear structures is exactly independent of D_1 and D_2 (because the spin cross-products are equivalently zero), to a good approximation, the DM interactions should have no effect on the collinear phases in any reasonable physical system[7].

---

[7] This statement is not exactly correct due to the so-called *order-by-disorder*. This phenomenon describes a situation where in a degenerate system the fluctuations stabilize one of the degenerate configurations over the others [18, 115, 116]. In the context of DM interactions and the collinear phases in AB-SKL, thermal order-by-disorder (or entropy) breaks the full rotational symmetry of these structures and forces the spins to point along the z-axis [80]. However, in a physical system there will always be some amount of SIA or exchange anisotropy, which will determine either the

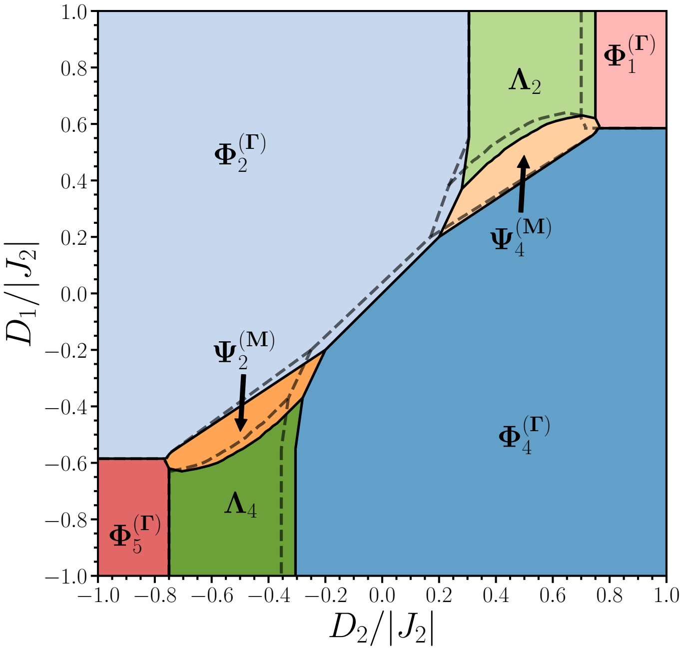

Figure 5.9: Effects of the in-plane anisotropy on the structure of the phase diagram in fig. 5.8 (a). The grey dashed lines indicate the new phase boundaries, calculated by adding SIA with $K_x = -0.1$.

5.5 Strong-SOC limit

Finally, let us briefly discuss what happens when we add the in-plane anisotropy to our model. As discussed previously, these interactions select a set of preferred orientations (fig. 2.6) in the plane of the kagome layers thus breaking the axial rotation symmetry. In this section, we would like to analyze how such anisotropic perturbations[8] modify the overall structure of a given phase diagram. This is important because we would like to test how the exotic phases discussed in the previous sections respond to symmetry-breaking terms in our model. If the phases of interest persist, there is a higher chance that they may be discovered experimentally in realistic physical systems.

The effects of the in-plane anisotropy on the spin structure of $\mathbf{Q} = \Gamma$ phases will

---

in- or out-of-plane ground state.

[8] There are cases in certain compounds, such as magnetic pyrochlore oxides, when the strength of the SIA becomes even larger than the exchange [117]. Such systems are better modelled by Ising-type interactions. Although these systems are interesting on their own, there is no experimental evidence that any of the known AB-SKL compounds possess such strong in-plane anisotropy.

be discussed in detail in the next chapter. Intuitively, however, we expect that the spin configurations in which most of the spins point along the relevant anisotropic axes would be favoured by the in-plane SIA and anisotropic exchange. This turns out to be true, as seen from the phase diagram in fig. 5.9 calculated using a weak SIA interactions[9]. We see that the stability regions of the $\mathbf{\Phi}_m^{(\mathbf{\Gamma})}$ $(m = 1, 4)$ are extended the most, since the corresponding spin structures align the most with the local anisotropic axes. Note that the application of SIA breaks the $\mu_0^{(+1,+1)}$ self-duality, which complicates the calculations of the phase diagram. Nevertheless, the overall structure of the diagram remains similar to that in the weak-SOC limit. We also confirm that the spin configurations remain nearly identical before and after application of the SIA, which suggests that the phases observed in our simulations are robust against the perturbations and may be stabilized in experimental systems.

5.6 Summary of important results and open questions

In this chapter we presented a near-extensive overview of ground state properties of the magnetic model for AB-SKL in eq. (2.30). Our results yielded an extremely rich phase behaviour, which we attributed to different types of energetic competitions that occur in our system. The results of this chapter are summarized in Ref. [80]. Note that this publication did not include some of the rare multiple-$\mathbf{Q}$ structures that occur close to the phase boundaries.

Here, we considered the effects of gradually increasing the strength of the SOC by first describing the properties of an isotropic system, then adding the DM interactions, and finally including the in-plane anisotropy. Our numerical calculations have determined that there is a large number of interesting phases, some of which correspond to the multiple-$\mathbf{Q}$ structures. Importantly, we were able to show that many of such exotic phases are stabilized in large pockets of parameter space and persist against various perturbations, such as the in-plane anisotropy. The numerical data also confirmed the existence of symmetry in the several phase diagrams, as a result of the self-duality transformations introduced in Chapter 3. Overall, self-duality was found to be an extremely helpful tool for studying the ground state properties of our

---

[9] Independently, we also calculated the phase diagram with a small exchange anisotropy, but the resulting phase boundaries looked nearly identical to fig. 5.9.

model.

One parameter that we have left unexplored is the applied magnetic field. How the different structures change in the non-zero field is an important question for experimental studies, and would be a logical next step in investigating the magnetic phases presented here. We have performed some preliminary calculations in the weak-SOC limit with fields oriented parallel and perpendicular to the kagome layers. In some cases, the magnetic configurations evolved smoothly until ferromagnetic saturation, while in other cases, the fields stabilized unusual intermediate structures. As a result these results require further analysis and will hopefully result in a separate study.

Chapter 6

Effects of the in-plane anisotropy on the structure of Q=Γ phases

> Most important part of doing physics is the knowledge of approximation.
>
> Lev Landau

At the end of the last chapter, we analyzed how the in-plane SIA modifies the structure of the magnetic phase diagrams. Including these interactions results in more free parameters in our model, which complicates the general analysis. However, as discussed in Sec. 1.2, magnetic anisotropy originates from the symmetry of the crystal environment, and is therefore always present in some capacity in real compounds. As a result, understanding how the anisotropic interactions influence the magnetic properties may be important for an accurate description of experimental results. For example, in Mn_3X compounds, the significant role of the SIA has been established early on [90, 118, 119]. However, until recently, the exact effects of this anisotropy on the $\mathbf{Q} = \Gamma$ ground state spin structure remained controversial [71–75]. Ref. [71] provides a derivation of the six-fold anisotropy and the induced magnetic moment in Mn_3X compounds ($m = 2$). Nevertheless, the impact of anisotropic exchange in these systems has not been considered at all, prior to our study in Ref. [75]. For these reasons, the goal of this chapter is to demonstrate how the perturbations in the form of the SIA and the anisotropic exchange modify the structure of the $\mathbf{\Phi}_m^{(\mathbf{\Gamma})}$ phases with any value of m.

6.1 Anisotropic energies of fixed structures

The first question that we would like to answer is how do the energies of the $\mathbf{Q} = \Gamma$ structures change when we apply the in-plane anisotropy? For clarity, we recall that we are considering the structures in fig. 5.4, which we allow to rotate in the plane of the kagome layers. In the previous chapter, we used simple reasoning to deduce that $\mathbf{Q} = \Gamma$ phases with $m = 1, 4$ would be stabilized the most by these interactions relative to the other phases. We can now demonstrate this analytically, by substituting the spin configurations into the energy expressions. (2.33) and (2.34). We will assume that the spins lie in the plane of the kagome layers, *e.g.* as a result of the DM interactions. First, as a crude approximation, we will calculate the anisotropic energy for each configuration assuming that the anisotropy does not modify the spin structure. Writing the spins in the polar form (*i.e.* substituting $\phi_i(\mathbf{r}) = \frac{\pi}{2}$ in eq. (2.38)) and using the expressions for the local anisotropic axes in eq. (2.35), we obtain through some algebraic manipulations

$$\begin{aligned}
E_K^{(m)}(\theta) &= K_x \sum_{\mathbf{r}} \sum_{i} \left(\mathbf{S}_i(\mathbf{r}) \cdot \hat{\mathbf{n}}_{ix}\right)^2 \\
&= K_x \sum_{\mathbf{r}} \sum_{i} \cos^2\left(\theta_i(\mathbf{r}) - \alpha_i\right) \\
&= N K_x \sum_{i} \cos^2\left(\frac{\pi l_i}{3}(m-1) + \theta\right), \qquad (6.1) \\
E_{A_k}^{(m)}(\theta) &= A_k^{(xy)} \sum_{\langle \mathbf{r}\mathbf{r}\rangle_k} \sum_{\langle ij\rangle_k} \left(\mathbf{S}_i(\mathbf{r}) \cdot \hat{\mathbf{n}}_{ix}\right)\left(\mathbf{S}_j(\mathbf{r}') \cdot \hat{\mathbf{n}}_{jx}\right) - \left(\mathbf{S}_i(\mathbf{r}) \cdot \hat{\mathbf{n}}_{iy}\right)\left(\mathbf{S}_j(\mathbf{r}') \cdot \hat{\mathbf{n}}_{jy}\right) \\
&= A_k^{(xy)} \sum_{\langle \mathbf{r}\mathbf{r}\rangle_k} \sum_{\langle ij\rangle_k} \cos\left(\theta_i(\mathbf{r}) + \theta_j(\mathbf{r}') - \alpha_i - \alpha_j\right) \\
&= 2N A_k^{(xy)} \sum_{\langle ij\rangle_k} \cos\left(\frac{\pi}{3}(l_i + l_j)(m-1) + 2\theta\right), \qquad (6.2)
\end{aligned}$$

where N is the total number of unit cells in the crystal, and we imposed the $\mathbf{Q} = \Gamma$ structure by setting $\theta_i(\mathbf{r}) = \frac{\pi l_i m}{3} + \theta$, with θ representing the in-plane rotations. The $A_k^{(xy)}$ are the anisotropic exchange constants and $\langle \ldots \rangle_k$ indicates the summation over k^{th} NN. Table 6.1 shows these energetic contributions for the six $\mathbf{\Phi}_m^{(\mathbf{\Gamma})}$ phases. These values lead to a few interesting observations. First, in agreement with our predictions, we see that the $m = 1, 4$ phases are always stabilized by the anisotropic interactions (after adjusting the global phase θ), regardless of the signs of the coupling constants.

In the other four states ($m = 0, 2, 3, 5$), most of the spins are not aligned with the corresponding local anisotropic axes (see fig. 6.1), leading to higher energetic

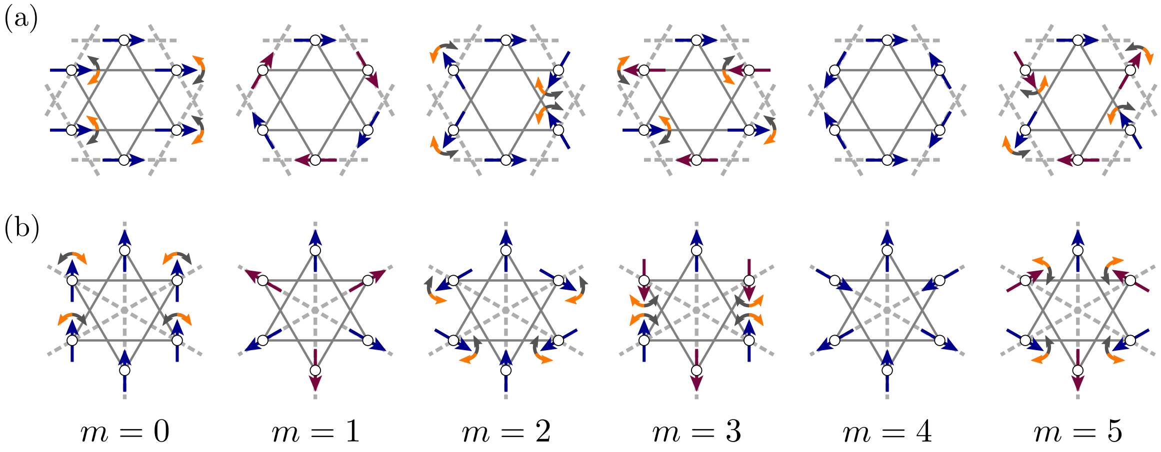

Figure 6.1: Effects of anisotropy on the $\mathbf{\Phi}_m^{(\mathbf{\Gamma})}$ spin configurations corresponding to (a) $\theta = 0$ and (b) $\theta = \frac{\pi}{2}$. The vectors are coloured in the same way as in fig. 5.4. The grey dashed lines represent the local (a) x and (b) y anisotropic axes. The curved arrows indicate the directions of the spin distortion when the values of g_m in eqs. (6.18 - 6.23) are positive (orange) and negative (dark grey).

m	0	1	2	3	4	5
$\frac{1}{N}E_K^{(m)}(\theta)$	$3K_x$	$6K_x\cos^2(\theta)$	$3K_x$	$3K_x$	$6K_x\cos^2(\theta)$	$3K_x$
$\frac{1}{N}E_{A_1}^{(m)}(\theta)$	0	$12A_1^{(xy)}\cos(2\theta)$	0	0	$-12A_1^{(xy)}\cos(2\theta)$	0
$\frac{1}{N}E_{A_2}^{(m)}(\theta)$	0	$12A_2^{(xy)}\cos(2\theta)$	0	0	$12A_2^{(xy)}\cos(2\theta)$	0

Table 6.1: Approximate anisotropic energies of the $\mathbf{\Phi}_m^{(\mathbf{\Gamma})}$ phases calculated using eqs. (6.1) and (6.2). Note that these values are inexact since we ignored the distortion of the spin structure.

penalties. Since the misalignment angle is always at 60 degrees to the anisotropy axis, the energies of these four states turn out to be the same. Yet, it comes as a surprise that the anisotropic energies of the $\mathbf{\Phi}_m^{(\mathbf{\Gamma})}$ structures with $m = 0, 2, 3, 5$ are independent of their in-plane orientations, determined by θ. In other words, the results in table 6.1 suggest that these four structures retain axial rotational symmetry. However, these predictions fall short when compared to the experimental data. For example, the ground state structure of the Mn_3Sn and Mn_3Ge has been experimentally established to be the $\mathbf{\Phi}_2^{(\mathbf{\Gamma})}$ phase with $\theta = 0$ and $\theta = \frac{\pi}{2}$ respectively [118, 120–124]. If this structure was in fact degenerate with respect to the in-plane rotations (as per column $m = 2$ in table 6.1), the excitation spectrum, measured by inelastic neutron scattering experiments, would be *gapless*, *i.e.* the in-plane rotations would yield zero-excitation energy. However, these experiments do, in fact, show a gap in the excitation spectrum, meaning that it costs a finite amount of energy to rotate the spins [72, 90, 125]. To explain this discrepancy between the experiment and theory, several works suggested a sixth-order SIA term in the model, which ultimately does produce energy spitting [71, 72, 90, 118]. The issue with this explanation is that in order to reproduce the experimental results, the sixth-order anisotropy must be quite large, which is highly unusual. These controversies prompt us to reconsider the above analysis in hopes of restoring the consistency with the experimental data.

6.2 Distortions of spin structure induced by anisotropy

The main flaw of the analysis in the previous section is that it assumes that the spin configurations remain unchanged when subjected to the in-plane anisotropy. In practice, for $m = 0, 2, 3, 5$ phases, these couplings introduce energetic competitions that result in tilting of the spins toward the anisotropic axes. Such distortion of the spin structure has been reported in the Mn_3X very early on, as it manifests in a small magnetic moment [118, 126, 127].

We can show that the anisotropic interactions distort certain spin structures analytically by considering the full energy of a planar spin configuration. We will keep the derivation general for all values of m to make sure that our predictions are sensible. The relevant terms in the model can then be written as

$$\mathcal{H} = \mathcal{H}_J + \mathcal{H}_D + \mathcal{H}_K + \mathcal{H}_A, \tag{6.3}$$

$$\mathcal{H}_J = \frac{1}{2}\sum_{\mathbf{r}\mathbf{r}'}\sum_{ij} J_{ij}(\mathbf{r}-\mathbf{r}')\cos\bigl(\theta_{ij}(\mathbf{r};\mathbf{r}')\bigr), \tag{6.4}$$

$$\mathcal{H}_D = -\frac{1}{2}\sum_{\mathbf{r}\mathbf{r}'}\sum_{ij} D_{ij}(\mathbf{r}-\mathbf{r}')\sin\bigl(\theta_{ij}(\mathbf{r};\mathbf{r}')\bigr), \tag{6.5}$$

$$\mathcal{H}_K = K_x\sum_{\mathbf{r}}\sum_{i} \cos^2(\theta_i(\mathbf{r}) - \alpha_i), \tag{6.6}$$

$$\mathcal{H}_A = \frac{1}{2}\sum_{\mathbf{r}\mathbf{r}'}\sum_{ij} A_{ij}^{(xy)}(\mathbf{r}-\mathbf{r}')\cos\bigl(\bar{\theta}_{ij}(\mathbf{r};\mathbf{r}') - \bar{\alpha}_{ij}\bigr), \tag{6.7}$$

where $\theta_{ij}(\mathbf{r};\mathbf{r}') = \theta_i(\mathbf{r}) - \theta_j(\mathbf{r}')$, $\bar{\theta}_{ij}(\mathbf{r};\mathbf{r}') = \theta_i(\mathbf{r}) + \theta_j(\mathbf{r}')$, and $\bar{\alpha}_{ij} = \alpha_i + \alpha_j$. Next, we can set

$$\theta_i(\mathbf{r}) = \frac{\pi l_i m}{3} + \theta + \delta\theta_i, \tag{6.8}$$

where θ again describes the in-plane rotations and $\delta\theta_i$ are small deviations from the unperturbed state structures. We will use these deviations to write down a harmonic expansion of the energy. To further simplify the analysis, we assume that the anisotropic interactions are of the order $\sim \delta\theta_i$. We obtain the following harmonic expansion of the energy per spin:

$$\begin{aligned}\frac{1}{N}E^{(m)}\Big(\theta;\{\delta\theta_i\}\Big) &= E_0^{(m)}(\theta) + \sum_i g_i^{(m)}(\theta)\delta\theta_i + \frac{1}{2}\sum_{ij} h_{ij}^{(m)}\delta\theta_i\delta\theta_j \\ &= E_0^{(m)}(\theta) + \mathbf{g}^{(m)}(\theta)\cdot\boldsymbol{\delta\theta} + \frac{1}{2}\boldsymbol{\delta\theta}^T\mathbf{h}^{(m)}\boldsymbol{\delta\theta}.\end{aligned} \tag{6.9}$$

The constant in eq. (6.9) is equal to

$$E_0^{(m)}(\theta) = 12J_1^{(m)} + 12J_2^{(m)} + E_K^{(m)}(\theta) + E_{A_1}^{(m)}(\theta) + E_{A_2}^{(m)}(\theta), \tag{6.10}$$

where $J_1^{(m)}$ and $J_2^{(m)}$ are defined exactly the same as for duality transformations $\mu_m^{(+1,+1)}$ in eq. (3.24). The Hessian matrices can be written in a compact form as

$$\mathbf{h}^{(m)} = \begin{bmatrix} \mathbf{h}_1^{(m)} & \mathbf{h}_2^{(m)} \\ \mathbf{h}_2^{(m)} & \mathbf{h}_1^{(m)} \end{bmatrix}, \tag{6.11}$$

$$\mathbf{h}_1^{(m)} = \begin{bmatrix} -4J_1^{(m)} - 4J_2^{(m)} & 2J_2^{(m)} & 2J_2^{(m)} \\ 2J_2^{(m)} & -4J_1^{(m)} - 4J_2^{(m)} & 2J_2^{(m)} \\ 2J_2^{(m)} & 2J_2^{(m)} & -4J_1^{(m)} - 4J_2^{(m)} \end{bmatrix}, \tag{6.12}$$

$$\mathbf{h}_2^{(m)} = \begin{bmatrix} 0 & 2J_1^{(m)} & 2J_1^{(m)} \\ 2J_1^{(m)} & 0 & 2J_1^{(m)} \\ 2J_1^{(m)} & 2J_1^{(m)} & 0 \end{bmatrix}. \tag{6.13}$$

Eq. (6.9) describes a generalized quadratic function which can be minimized according to the procedure in the Appendix C. We can diagonalize the Hessian matrices simultaneously using an orthogonal matrix $\mathbf{R}$:

$$\mathbf{R} = \begin{bmatrix} \frac{1}{\sqrt{6}} & \frac{1}{\sqrt{3}} & 0 & \frac{1}{\sqrt{6}} & \frac{1}{\sqrt{3}} & 0 \\ \frac{1}{\sqrt{6}} & -\frac{1}{\sqrt{12}} & \frac{1}{2} & \frac{1}{\sqrt{6}} & -\frac{1}{\sqrt{12}} & \frac{1}{2} \\ \frac{1}{\sqrt{6}} & -\frac{1}{\sqrt{12}} & -\frac{1}{2} & \frac{1}{\sqrt{6}} & -\frac{1}{\sqrt{12}} & -\frac{1}{2} \\ \frac{1}{\sqrt{6}} & \frac{1}{\sqrt{3}} & 0 & -\frac{1}{\sqrt{6}} & -\frac{1}{\sqrt{3}} & 0 \\ \frac{1}{\sqrt{6}} & -\frac{1}{\sqrt{12}} & \frac{1}{2} & -\frac{1}{\sqrt{6}} & \frac{1}{\sqrt{12}} & -\frac{1}{2} \\ \frac{1}{\sqrt{6}} & -\frac{1}{\sqrt{12}} & -\frac{1}{2} & -\frac{1}{\sqrt{6}} & \frac{1}{\sqrt{12}} & \frac{1}{2} \end{bmatrix}. \tag{6.14}$$

The columns of matrix $\mathbf{R}$ in eq. (6.14) represent normal rotation modes of the spins in each unit cell. Note, however, that the first column describes a uniform rotation of spins in the plane. Since we already designated this mode to θ, we will remove it from further calculations. The remaining five modes describe different kinds of distortions of the spin structure. The eigenvalues of $\mathbf{h}^{(m)}$ corresponding to these five modes are

$$\operatorname{diag}(\mathbf{R}^T\mathbf{h}^{(m)}\mathbf{R}) = \begin{bmatrix} -6J_1^{(m)} - 6J_2^{(m)} \\ -6J_1^{(m)} - 6J_2^{(m)} \\ -8J_1^{(m)} \\ -2J_1^{(m)} - 6J_2^{(m)} \\ -2J_1^{(m)} - 6J_2^{(m)} \end{bmatrix}. \tag{6.15}$$

One can verify that in the regions of parameter space where $\mathbf{\Phi}_m^{(\mathbf{\Gamma})}$ are stable, the eigenvalues of the Hessian are positive, meaning that the matrix is positive-definite. Next, we obtain

$$\mathbf{R}^T\mathbf{g}^{(m)} = -g_m \begin{bmatrix} \sin(2\theta) \\ \epsilon_m \cos(2\theta) \\ 0 \\ 0 \\ 0 \end{bmatrix}, \tag{6.16}$$

where

$$\epsilon_m = \begin{cases} +1 & \text{if } m = 0, 1, 3, 4 \\ -1 & \text{if } m = 2, 5, \end{cases} \tag{6.17}$$

$$g_0 = \sqrt{3}(K_x + 2A_1^{(xy)} - 2A_2^{(xy)}), \tag{6.18}$$

$$g_1 = 0, \tag{6.19}$$

$$g_2 = \sqrt{3}(K_x + 2A_1^{(xy)} - 2A_2^{(xy)}), \tag{6.20}$$

$$g_3 = \sqrt{3}(K_x - 2A_1^{(xy)} - 2A_2^{(xy)}), \tag{6.21}$$

$$g_4 = 0, \tag{6.22}$$

$$g_5 = \sqrt{3}(K_x - 2A_1^{(xy)} - 2A_2^{(xy)}). \tag{6.23}$$

Unsurprisingly, the gradients for $m = 1, 4$ structures are zero. In the remaining cases, minimization of the energy yields a distortion

$$\mathbf{R}^T \delta\boldsymbol{\theta}^{(m)} = -\frac{g_m}{j_m} \begin{bmatrix} \sin(2\theta) \\ \epsilon_m \cos(2\theta) \\ 0 \\ 0 \\ 0 \end{bmatrix}, \tag{6.24}$$

where $j_m = 6(J_1^{(m)} + J_2^{(m)})$. As expected, this distortion rotates the "misalligned" spins in the $m = 0, 2, 3, 5$ structures towards the anisotropic axes, as shown in fig. 6.1 for the specific cases of $\theta = 0, \frac{\pi}{2}$.

6.3 Consequences of the anisotropic distortion

We have shown in the previous section that the in-plane anisotropy leads to the expected distortion of some of the spin structures. From eq. (C.6) in Appendix C we conclude that the energetic contribution of the anisotropy-induced distortion is simply

$$\delta E^{(m)}(\theta) = \frac{g_m^2}{2j_m}, \tag{6.25}$$

which is negative (since we've established that the eigenvalue $-6(J_1^{(m)} + J_2^{(m)})$ is positive). This expression is still independent of the in-plane rotation angle, θ. Therefore, in order to demonstrate that the structural distortion removes the accidental axial rotational degeneracy, we must include the anisotropic couplings in the Hessian. To simplify things, we will only consider the relevant structures with $m = 0, 2, 3, 5$. This changes the form of the matrix from diagonal to block-diagonal:

$$\mathbf{R}^T\mathbf{h}\mathbf{R} = \begin{bmatrix} \bar{\mathbf{h}}_{2\times 2} & \mathbf{0}_{2\times 3} \\ \mathbf{0}_{3\times 2} & \tilde{\mathbf{h}}_{3\times 3} \end{bmatrix}, \tag{6.26}$$

where $\mathbf{0}_{i\times j}$ is a zero matrix with i rows and j columns. We see that the anisotropy introduces cross-coupling between the two relevant modes, but luckily, they remain uncoupled to the remaining three modes of the Hessian. Since the inverse of a block-diagonal matrix is calculated by independently inverting the blocks, we can focus solely on $\bar{\mathbf{h}}_{2\times 2}$:

$$\bar{\mathbf{h}}_{2\times 2} = \begin{bmatrix} -j_m - f_m\cos(2\theta) & -\epsilon_m f_m \sin(2\theta) \\ -\epsilon_m f_m \sin(2\theta) & -j_m + f_m\cos(2\theta) \end{bmatrix}, \tag{6.27}$$

where

$$f_0 = K_x - A_1^{(xy)} + A_2^{(xy)}, \tag{6.28}$$

$$f_2 = K_x - A_1^{(xy)} + A_2^{(xy)}, \tag{6.29}$$

$$f_3 = K_x + A_1^{(xy)} + A_2^{(xy)}, \tag{6.30}$$

$$f_5 = K_x + A_1^{(xy)} + A_2^{(xy)}. \tag{6.31}$$

After inverting the Hessian and simplifying the expressions through some tedious algebra, we can obtain the new value of the distortion energy, using eq. (C.6) in Appendix C and assuming $|J_m| \gg |f_m|$:

$$\delta E^{(m)}(\theta) = \frac{g_m^2}{2j_m} + \frac{g_m^2 f_m}{2j_m^2}\cos(6\theta). \tag{6.32}$$

This simple equation elegantly demonstrates how the anisotropy-induced distortions in the spin structure break the continuous rotational symmetry and simultaneously establish the six-fold crystal symmetry. Similar equation has been derived for the $m =$

2 ground state of the Mn_3X compounds by Liu and Balents in Ref. [71]. Importantly, the rotational symmetry is broken at a cubic order of the anisotropic parameters, which means that one requires a fairly large in-plane anisotropy in order to gap the $m = 0, 2, 3, 5$ $\mathbf{Q} = \Gamma$ structures.

Let us now discuss the implications of this equation. In a given structure, the sign of f_m determines if the spin configuration aligns with the local x axes ($f_m < 0$, $\theta = \frac{n\pi}{3}$) or the local y-axes ($f_m > 0$, $\theta = \frac{(2n+1)\pi}{6}$). Once this direction is specified, g_m controls the distortion of the spin structure, as per eq. (6.24). The expressions for g_m in eqs. (6.18), (6.20), (6.21), and (6.23) lead to two interesting observations. Firstly, note that the anisotropic exchange parameters result in distortions that are twice as large as the distortions due to the SIA of equivalent strength. This difference comes from the fact that the former are two-site interactions and benefit from anisotropic stabilization on the neighbouring atoms. As a result, a small exchange anisotropy may produce a more noticeable distortion in the spin structure than a small SIA perturbation. Secondly, we note that K_x and $A_2^{(xy)}$ have opposite signs in all relevant expressions for g_m, and simultaneously have the same signs in the expressions for f_m in eqs. (6.28 - 6.31). This means that while these parameters favour the same type of anisotropic axes (local x-axes for $K_x < 0$ and $A_2^{(xy)} < 0$ and local y-axes for $K_x > 0$ and $A_2^{(xy)} > 0$), they lead to deviations in the opposite directions, as presented in fig. 6.1. This provides a signature for the two types of interactions on a kagome lattice, which can be observed in experiments, such as elastic neutron scattering.

6.4 Implications for the ground state of Mn_3X

As discussed in the beginning of this chapter, the results derived in the previous section are relevant to the properties of the magnetic ground state of the Mn_3X systems. The anisotropic gap follows from eq. (6.32) and can also be obtained using the spin-wave approach [75].

The magnetic moment per spin in Mn_3X induced by the anisotropic distortion of the spin structure has been shown to be equal to

$$|\mathbf{M}| = \frac{1}{3}\left|1 + 2\cos\left(\frac{2\pi}{3} - \frac{g_2}{2j_2}\right)\right|, \tag{6.33}$$

where the distortion is written to linear order in the anisotropic parameters [71]. The orientation of the magnetic moment is controlled by the signs and relative values of K_x, $A_1^{(xy)}$, and $A_2^{(xy)}$, as discussed previously. Since the magnetic moment is relatively easy to measure in experiments, it can be used to estimate the relative contributions of the anisotropic interactions. To aid the experimental studies, Ref. [75] presents numerical results showing how the value of the magnetic moment changes with varying model parameters. This work also shows calculations of the static and dynamic structure factors, relevant to the elastic and inelastic neutron scattering experiments. Notably, the spin wave excitations were shown to be more sensitive to the small changes in the spin structure, which can hopefully be utilized in establishing the role of the anisotropic exchange in these systems.

6.5 Summary of important results and open questions

This chapter presents an analytic study of in-plane anisotropy in AB-SKL, as applied to the $\mathbf{Q} = \Gamma$ ground states. We compare the effects of anisotropic interactions on the spin structures of the six characteristic configurations and demonstrate that in four of these phases this anisotropy induces a distortion, which pins these structures to the local anisotropy axes. This study is unique in that it includes exchange anisotropy, which has been traditionally neglected from the discussion. We show that although the application of SIA and exchange anisotropy leads to qualitatively the same results, the specific structural changes that they produce may be very different.

A version of the above analysis applied to $m = 2$ ground states of the Mn_3X was published in Ref. [75], and the generalization to other values of m was discussed in Ref. [80]. The derivation presented in this thesis provides a consistent approach for studying the effects of the in-plane anisotropy in the $\mathbf{Q} = \Gamma$ structures summarized in a compact form in eq. (6.32). Many of the previous attempts at explaining the anisotropy in the Mn_3X systems relied on group-theoretical classification of different structures, attempting to describe the induced magnetic moment as a linear combination of the $m = 0$ and $m = 2$ states [73]. Although this approach is extremely useful for systematic studies of magnetic configurations, it fails to take into account the normalization of spin vectors ($|\mathbf{S}(\mathbf{r})|^2 = 1$), which inevitably lead to the erroneous conclusion that the second-order SIA does not gap the in-plane rotations. Before

Ref. [75], this mistake was also pointed out in [74, 92].

To conclude, we note that like in the previous chapter, the most logical extension of this work is in adding external magnetic fields. This only slightly modifies the harmonic energy in eq. (6.9) and should add an energetic dependence on $\cos(\theta)$ and $\sin(\theta)$. This generalization is very important for the experimental studies, since in most magnetic experiments the spin structure is studied with applied external fields. Furthermore, analyzing these properties at finite temperatures is another important problem, since large enough thermal fluctuations may reduce the anisotropic pinning.

The author would like to express a special gratitude to Jason McCoombs, who first realized the inconsistency of the linear combinations of $m = 0, 2$ states with the creation of the anisotropic energy gap. The work outlined in this chapter is a consequence of many fruitful discussions with Jason about the effects of the SIA in the Mn_3X compounds.

Chapter 7

The mysterious Ising-like phases

> The beginning of knowledge is the discovery of something we do not understand.
>
> Frank Herbert

Among the magnetic structures presented in Chapter 5, the properties of the $\mathbf{\Lambda}_m$ phases stand out for several reasons. The most striking difference between these structures and other magnetic configurations revealed in our numerical simulations is the absence of a conventional long-range order. Absence of translational symmetry in the magnetic structure indicates large degeneracy and often points to exotic physical phenomena, as in the case of the 2D kagome antiferromagnet (Sec. 1.1.3). Secondly, the Ising-like structure of these phases is surprising, since we are dealing with continuous spin vectors, and since the exchange and DM interactions allow for continuous spin rotations in the kagome plane. Typically, phases with incommensurate wavevectors manifest in structures with continuously varying spins, such as simple spiral states, rather than sharp, domain-like arrangements.

It took the author over two years to come up with a coherent story that could explain why these structures appear in the AB-SKL, and still, some questions remain unanswered. In this chapter, we would like to use analytical methods in order to provide explanations for the nature of their unusual ordering. These results will allow us to better understand the numerical results in Chapter 8, where we will consider the finite-temperature properties of the Ising-like phases.

7.1 Why should we study Ising-like phases

Here, we are proposing to conduct a study of exotic magnetic structures, which, however, have not yet been observed experimentally. In the introductory paragraph above we mentioned several reasons for why these phases are interesting from a theoretical standpoint, but we have not provided any reasoning for why one should pursue further in-depth studies. After all, there is a great number of magnetic systems where it is possible to stabilize various exotic magnetic structures.

The main reason for studying these Ising-like phases is the relatively high probability of experimental discovery. Let us justify this with an example. Currently, some of the most intriguing magnetic states are the spin liquids, which do not display any long-range order down to zero temperature. To this day, experimental studies have identified dozens of spin liquid candidate compounds, but an actual experimental discovery of this phase has not been declared so far. The two most famous examples of theoretical predictions of spin liquids are the 2D kagome antiferromagnet, which we have discussed in Sec. 1.1.3, and the Kitaev model on a honeycomb lattice, where the disordered ground state is established by unique anisotropic interactions [30]. The main challenge with both of these examples is that the exotic properties only hold in a very narrow region of parameter space[1]. For example, the degeneracy in the 2D kagome is easily removed by introducing anisotropic interactions, while the addition of exchange completely removes the spin liquid phase in Kitaev systems. As a result, these exotic states are very difficult to access experimentally, since one can never fully control the interactions in a given compound[2]. This weakness is shared among most frustrated systems that manifest complex structures with large degeneracy: it is very unusual for such phases to persist over a wide range of model parameters.

On the contrary, we have seen in Sec. 5.4 and 5.5 that the Ising-like phases are stable with respect to variation of different model parameters and occupy a relatively large total volume of the parameter space. The fact that these structures do not require fine-tuning of parameters and persist even in the presence of SIA and anisotropic exchange makes the prospects of experimental realization of these structures very promising. Additionally, the self-duality properties of the model discussed

---

[1] Both examples given in the text describe exotic phases that exist as isolated *points* in the parameter space. Yet, a considerable experimental effort has been put forward to search for these states in hopes that these phases might persist beyond the theoretically established boundaries.

[2] In addition, experimental systems often introduce other perturbing factors, such as structural disorder and impurities.

in Chapter 3 even further increases the chances of discovering these structures in real compounds.

Before proceeding to our analysis, it is useful to identify the objectives for this chapter. We have discussed two interesting features of Ising-like phases: absence of long-range order and binary (Ising-like) character of the spin structures. In this chapter, we will provide an explanation for the second property using analytical analysis of the Hamiltonian. The origin of disorder turns out to be a more difficult question. We will therefore limit our discussion to hints obtained from the numerical simulations, which will hopefully guide the future studies of this question.

7.2 First attempt: ignoring the spin deviations

To simplify our analysis, we will focus on a simplified Hamiltonian of the form

$$\mathcal{H} = \mathcal{H}_J + \mathcal{H}_D, \tag{7.1}$$

where both exchange and DM interactions are restricted to NN. Furthermore, since we have seen in fig. 5.2 (a) that the spin configurations lie in the plane of the kagome layers, we will ignore the z components of spins. Finally, since all structures in this work are characterized by $Q_z = 0$, we will only consider a single AB bilayer. This leads to simplified expressions for $\mathcal{H}_J$ and $\mathcal{H}_D$ as given by eqs. (6.4) and (6.5) respectively.

Consider different $\mathbf{\Lambda}_4$ spin configurations, shown in fig. 7.1, which were calculated by varying the values of D_1 and D_2. As noted previously, the spin arrangements in each unit cell are approximately the same as those of the $\mathbf{\Phi}_4^{(\mathbf{\Gamma})}$. Therefore, as a first approximation, we may set

$$\theta_i(\mathbf{r}) = \frac{\pi l_i m}{3} + \theta(\mathbf{r}), \tag{7.2}$$

where the $\theta(\mathbf{r})$ describe the rotations of the sublattice spin configurations in each unit cell. Thus, we reduce the total number of degrees of freedom from $6N$ (where N is the number of unit cells) to N. Such a procedure of eliminating the microscopic details of the model is typically referred to as *coarse-graining*[3]. The resulting Hamiltonian can be shown to reduce down to

---

[3] Technically speaking, the analysis in the previous chapter was an extreme case of coarse-graining: we reduced $6N$ degrees of freedom to a single one (in-plane rotations, described by θ).

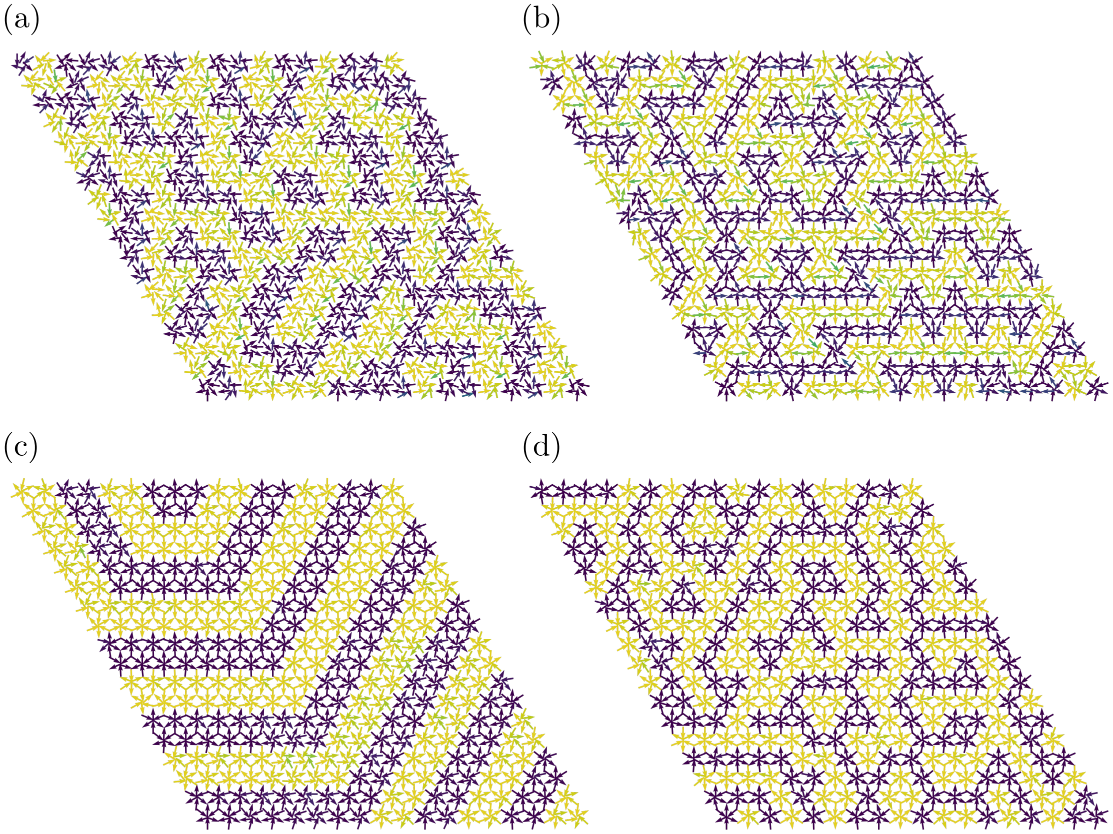

Figure 7.1: Examples of $\mathbf{\Lambda}_4$ spin configurations, calculated using MC simulations. The parameters used to obtain these structures were $J_1 = 1$, $J_2 = 1$ and $(D_1,\ D_2)$ equal to (a) (-1,-0.5), (b) (-1,-0.6), (c) (-4, -0.5), and (d) (-4,-0.6). The colours are chosen in the same way as in fig. 5.2.

$$E_0^{(m)}(\mathbf{r}) = E_0^{(m)} + J_2^{(m)} \sum_{\langle \mathbf{r}\mathbf{r}' \rangle} \cos\big(\theta(\mathbf{r};\mathbf{r}')\big), \tag{7.3}$$

where $E_0^{(m)} = 6J_1^{(m)} + 6J_2^{(m)}$, $\langle \cdots \rangle$ implies summation over the nearest-neighbours of a triangular lattice, and $\theta(\mathbf{r};\mathbf{r}') = \theta(\mathbf{r}) - \theta(\mathbf{r}')$. As in the previous chapter, the $J_1^{(m)}$, $J_2^{(m)}$, $D_1^{(m)}$, and $D_2^{(m)}$ can be calculated from the corresponding $\mu_m^{(+1,+1)}$ duality transformations in eq. (3.24). Let us define a unit vector $\hat{\mathbf{A}}(\mathbf{r})$ on each site of the triangular lattice, described by $\mathbf{r}$, such that

$$\hat{\mathbf{A}}(\mathbf{r}) = \begin{bmatrix} \cos\big(\theta(\mathbf{r})\big) \\ \sin\big(\theta(\mathbf{r})\big) \end{bmatrix}. \tag{7.4}$$

Then, eq. (7.3) can be re-written as

$$E_0^{(m)}(\{\theta(\mathbf{r})\}) = E_0^{(m)} + J_2^{(m)} \sum_{\langle \mathbf{r}\mathbf{r}' \rangle} \hat{\mathbf{A}}(\mathbf{r}) \cdot \hat{\mathbf{A}}(\mathbf{r}'), \tag{7.5}$$

which is equivalent to an effective exchange model on triangular lattice. Then, if $J_2^{(m)} < 0$, the ground state structure is ferromagnetic in $\hat{\mathbf{A}}(\mathbf{r})$, meaning that we obtain a $\mathbf{\Phi}_m^{(\mathbf{\Gamma})}$ structure. If $J_2^{(m)} > 0$, the system becomes frustrated, and the ground state corresponds to the 120 degree arrangement of the $\hat{\mathbf{A}}(\mathbf{r})$ vectors, which is the same as one of the $\mathbf{\Phi}_m^{(\mathbf{K})}$ structures, which are not Ising-like. Therefore, the above coarse-graining approach is only capable of producing ordered states with $\mathbf{Q} = \Gamma$ or $\mathbf{Q} = \mathrm{K}$. This suggests that the deviations from the perfect $\mathbf{\Phi}_m^{(\mathbf{\Gamma})}$ structures in each unit cell are important and must be taken into account in our coarse-graining procedure.

7.3 Effects of spin deviations

The small deviations from the perfect 120 degree configurations seen in fig. 7.1 are reminiscent of the the spin twists induced by the in-plane anisotropy, as discussed in the previous chapter. Notably, in structures with larger magnitude of D_1 (*e.g.* fig. 7.1 (c) and (d)) these deviations are smaller than in those with smaller magnitude of D_1 (*e.g.* fig. 7.1 (a) and (b)). The similarity of the two problems suggests an approach akin to that in Sec. 6.2. This time, let us take

$$\theta_i(\mathbf{r}) = \frac{\pi l_i m}{3} + \theta(\mathbf{r}) + \delta\theta_i(\mathbf{r}), \tag{7.6}$$

where $\delta\theta_i(\mathbf{r})$ describe the small deviations of each spin. Expanding the energy up to quadratic order in $\delta\theta_i(\mathbf{r})$ gives

$$\begin{aligned} E^{(m)}(\{\theta(\mathbf{r}); \delta\theta_i(\mathbf{r})\}) &= E_0^{(m)}(\{\theta(\mathbf{r})\}) + \sum_{\mathbf{r}} \sum_i g_i^{(m)}(\mathbf{r}) \delta\theta_i(\mathbf{r}) \\ &\qquad + \frac{1}{2} \sum_{\mathbf{r}\mathbf{r}'} \sum_{ij} h_{ij}^{(m)}(\mathbf{r}, \mathbf{r}') \delta\theta_i(\mathbf{r}) \delta\theta_j(\mathbf{r}') \qquad (7.7) \\ &= E_0^{(m)}(\{\theta(\mathbf{r})\}) + \mathbf{g}^{(m)} \cdot \delta\boldsymbol{\theta} + \frac{1}{2} \delta\boldsymbol{\theta}^T \mathbf{h}^{(m)} \delta\boldsymbol{\theta}. \qquad (7.8) \end{aligned}$$

The gradient vector is given by

$$\mathbf{g}^{(m)} = -D_2^{(m)} \begin{bmatrix} C(\mathbf{r}; -\mathbf{a}_2; -\mathbf{a}_1 - \mathbf{a}_2) \\ C(\mathbf{r}; -\mathbf{a}_1; +\mathbf{a}_2) \\ C(\mathbf{r}; +\mathbf{a}_1 + \mathbf{a}_2; +\mathbf{a}_1 \\ C(\mathbf{r}; +\mathbf{a}_2; +\mathbf{a}_1 + \mathbf{a}_2) \\ C(\mathbf{r}; +\mathbf{a}_1; -\mathbf{a}_2) \\ C(\mathbf{r}; -\mathbf{a}_1 - \mathbf{a}_2; -\mathbf{a}_2) \end{bmatrix}, \tag{7.9}$$

where

$$C(\mathbf{r}; \boldsymbol{\rho}_{;} \boldsymbol{\rho}_2) = \cos\big(\theta(\mathbf{r}; \mathbf{r} + \boldsymbol{\rho}_1)\big) - \cos\big(\theta(\mathbf{r}; \mathbf{r} + \boldsymbol{\rho}_2)\big), \tag{7.10}$$

and $\theta(\mathbf{r}; \mathbf{r}') = \theta(\mathbf{r}) - \theta(\mathbf{r}')$. Note that we are considering both the unit cell positions $\mathbf{r}$ and the sublattice labels i as the vector indices of $\mathbf{g}^{(m)}$. As a result, the Hessian matrix $\mathbf{h}^{(m)}$ is a $6N \times 6N$ matrix, which presents a challenge for our analysis, since we cannot diagonalize or invert for arbitrary values of $\theta(\mathbf{r})$[4]. Therefore, we must determine an approximate form of the Hessian in order to make further analytical progress. The solution comes from the relative values of the model parameters in the regions where the Ising-like phases are stable. Consider the boundaries of the $\boldsymbol{\Lambda}_4$ in diagram 5.8 (a). We estimate

$$\begin{aligned} J_1^{(4)} &\lesssim -0.93, && (7.11) \\ -0.20 \lesssim J_2^{(4)} &\lesssim 0.15, && (7.12) \\ 1.0 \lesssim D_2^{(4)} &\lesssim 1.24, && (7.13) \end{aligned}$$

where we omitted $D_1^{(4)}$ since these couplings do not appear anywhere in (7.8). These value ranges remain valid for the dual phases with arbitrary m. In most cases, we have $|D_2^{(m)}|/|J_1^{(m)}| < 1$, $|J_2^{(m)}|/|J_1^{(m)}| \ll 1$. If we also assume that $|D_2^{(m)}| \sim \mathcal{O}(\delta\boldsymbol{\theta})$, we can remove both $J_2^{(m)}$ and $D_2^{(m)}$ from the Hessian in order to keep the expansion in eq. (7.8) quadratic in $\delta\boldsymbol{\theta}$. With these approximations, we can write the Hessian in

---

[4] The issue here is that $\theta(\mathbf{r})$ generally breaks translational symmetry of the Hamiltonian, which is reflected in the Hessian. Without translational symmetry, this matrix cannot be diagonalized with Fourier transforms, which requires us to turn to approximation methods.

terms of $J_1^{(m)}$ only:

$$\mathbf{h}^{(m)} \approx J_1^{(m)} \delta(\mathbf{r}-\mathbf{r}') \begin{bmatrix} -2 & 0 & 0 & 0 & 1 & 1 \\ 0 & -2 & 0 & 1 & 0 & 1 \\ 0 & 0 & -2 & 1 & 1 & 0 \\ 0 & 1 & 1 & -2 & 0 & 0 \\ 1 & 0 & 1 & 0 & -2 & 0 \\ 1 & 1 & 0 & 0 & 0 & -2 \end{bmatrix}, \tag{7.14}$$

where $\delta(\mathbf{r}-\mathbf{r}')$ is a delta function. This matrix is diagonalized by $\mathbf{R}$ in eq. (6.14). As before, we ignore the eigenvectors that describe uniform rotations of spins in each cell and focus on the remaining five modes, which yield the following eigenvalues (each repeated N times):

$$\operatorname{diag}(\mathbf{R}^T \mathbf{h}) = \begin{bmatrix} -3J_1^{(m)} \\ -3J_1^{(m)} \\ -4J_1^{(m)} \\ -J_1^{(m)} \\ -J_1^{(m)} \end{bmatrix}. \tag{7.15}$$

Since $J_1^{(m)}$ is always negative in the stability region of the Ising-like phases, the Hessian is always positive-definite. Minimizing eq. (7.8) with respect to $\delta\boldsymbol{\theta}$ gives the effective model in $\theta(\mathbf{r})$ modes:

$$\mathcal{H}_{\text{eff}}^{(m)} = E_0^{(m)}(\{\theta(\mathbf{r})\}) + \delta E^{(m)}(\{\theta(\mathbf{r})\}), \tag{7.16}$$

where the energy correction is calculated according to eq. (C.6) in Appendix C:

$$\begin{aligned} \delta E^{(m)}(\{\theta(\mathbf{r})\}) = & -5\mathcal{K}^{(m)} \sum_{\boldsymbol{\rho}} \cos^2\theta(\mathbf{r};\mathbf{r}+\boldsymbol{\rho}) \\ & + \mathcal{K}^{(m)} \sum_{\boldsymbol{\rho}_1 \neq \boldsymbol{\rho}_2} \cos\theta(\mathbf{r};\mathbf{r}+\boldsymbol{\rho}_1)\cos\theta(\mathbf{r};\mathbf{r}+\boldsymbol{\rho}_2), \end{aligned} \tag{7.17}$$

with $\boldsymbol{\rho} = \mathbf{r}-\mathbf{r}'$ labelling the NN sites on the triangular lattice and

$$\mathcal{K}^{(m)} = -\frac{\left(D_2^{(m)}\right)^2}{12 J_1^{(m)}} \tag{7.18}$$

is a positive constant. We can also write eq. (7.16) in terms of the $\hat{\mathbf{A}}(\mathbf{r})$ vectors:

$$\mathcal{H}_{\text{eff}}^{(m)} = E_0^{(m)} + \sum_{\mathbf{r}} \Bigg[J_2^{(m)} \sum_{\boldsymbol{\rho}} \hat{\mathbf{A}}(\mathbf{r}) \cdot \hat{\mathbf{A}}(\mathbf{r}+\boldsymbol{\rho}) - 5\mathcal{K}^{(m)} \sum_{\boldsymbol{\rho}} \Big(\hat{\mathbf{A}}(\mathbf{r}) \cdot \hat{\mathbf{A}}(\mathbf{r}+\boldsymbol{\rho}) \Big)^2 \\ + \mathcal{K}^{(m)} \sum_{\boldsymbol{\rho}_1 \neq \boldsymbol{\rho}_2} \Big(\hat{\mathbf{A}}(\mathbf{r}) \cdot \hat{\mathbf{A}}(\mathbf{r}+\boldsymbol{\rho}_1) \Big) \Big(\hat{\mathbf{A}}(\mathbf{r}) \cdot \hat{\mathbf{A}}(\mathbf{r}+\boldsymbol{\rho}_2) \Big) \Bigg]. \tag{7.19}$$

We see that in addition to the effective exchange interactions governed by $J_2^{(m)}$ (first term in the square brackets), spin deviations induce through $D_2^{(m)}$ an effective biquadratic[5] (second term) and three-site interactions (third term), which are controlled by parameter $\mathcal{K}^{(m)}$. From the parameter ranges in (7.11 - 7.13) we can estimate that $0.1|J_2^{(m)}| \lesssim |\mathcal{K}^{(m)}| \lesssim |J_2^{(m)}|$ in the stability region of the Ising phases. This tells us that the effective interactions from $\delta E^{(m)}(\{\theta(\mathbf{r})\})$ are non-negligible and could play a crucial role in stabilizing the ground state structure.

Before proceeding to the next stage of the analysis, we would like to stop to appreciate these results. Firstly, recall that for $m = 0$ the dual parameters are the same as the regular model parameters, *i.e.* $(J_1^{(0)}, J_2^{(0)}, D_1^{(0)}, D_2^{(0)}) = (J_1, J_2, D_1, D_2)$. Therefore, the Ising-like phase $\boldsymbol{\Lambda}_0$ is obtained for $|D_2|/|J_1| < 1$, $|J_2|/|J_1| \ll 1$ with $J_1 < 0$. This situation is very unusual, since the DM couplings correspond to the dominant intra-layer interactions. It is extremely unlikely that this scenario would ever be realized in real compounds. However, thanks to the self-duality, we can obtain models that stabilize the same types of phases but have more realistic parameter requirements.

7.4 Quadrupole moments

Let us take a closer look at the biquadratic term in eq. (7.19). Since $\mathcal{K}^{(m)} > 0$, the coefficient of the biquadratic interaction $(-5\mathcal{K}^{(m)})$ is negative. Therefore, these effective couplings will favour both ferromagnetic and antiferromagnetic collinear arrangements of $\hat{\mathbf{A}}(\mathbf{r})$. This type of ordering is characteristic of *nematic liquid crystals* [128, 129]. Liquid crystals are typically composed of rod-like particles that do

---

[5] By biquadratic interactions, we imply any terms of the form $(\hat{\mathbf{A}}(\mathbf{r}) \cdot \hat{\mathbf{A}}(\mathbf{r}'))^2$.

not have a specified direction[6]. The orientation of each rod is instead specified by a *quadrupole moment*:

$$\mathcal{Q}_{\alpha\beta} = n_\alpha n_\beta - \frac{1}{3}\delta_{\alpha\beta}, \tag{7.20}$$

where $\hat{\mathbf{n}}$ is called a *director* of the particle, and $\delta_{\alpha\beta}$ is the Kronecker delta. Note that the prefactor of the delta function depends on the number of components in the director. We can similarly define a quadrupole moment on each site $\mathbf{r}$ as

$$\mathcal{Q}_{\alpha\beta}(\mathbf{r}) = A_\alpha(\mathbf{r})A_\beta(\mathbf{r}) - \frac{1}{2}\delta_{\alpha\beta}. \tag{7.21}$$

From this point, we will also refer to $\hat{\mathbf{A}}(\mathbf{r})$ as dipoles. With this, we can define different products involving quadrupoles and dipoles:

$$\begin{aligned}
\boldsymbol{\mathcal{Q}}(\mathbf{r}) \cdot \boldsymbol{\mathcal{Q}}(\mathbf{r}') &= \sum_{\alpha\beta} \mathcal{Q}_{\alpha\beta}(\mathbf{r})\mathcal{Q}_{\alpha\beta}(\mathbf{r}') \\
&= \left(\hat{\mathbf{A}}(\mathbf{r}) \cdot \hat{\mathbf{A}}(\mathbf{r}')\right)^2 - \frac{1}{2}, && (7.22) \\
\hat{\mathbf{A}}^T(\mathbf{r}_1)\boldsymbol{\mathcal{Q}}(\mathbf{r})\hat{\mathbf{A}}(\mathbf{r}_2) &= \sum_{\alpha\beta} A_\alpha(\mathbf{r}_1)\mathcal{Q}_{\alpha\beta}(\mathbf{r})A_\beta(\mathbf{r}_2) \\
&= \left(\hat{\mathbf{A}}(\mathbf{r}) \cdot \hat{\mathbf{A}}(\mathbf{r}_1)\right)\left(\hat{\mathbf{A}}(\mathbf{r}) \cdot \hat{\mathbf{A}}(\mathbf{r}_2)\right) - \frac{1}{2}\hat{\mathbf{A}}(\mathbf{r}_1) \cdot \hat{\mathbf{A}}(\mathbf{r}_2). && (7.23)
\end{aligned}$$

using these definitions, the effective Hamiltonian in eq. (7.19) becomes

$$\begin{aligned}
\mathcal{H}_{\text{eff}}^{(m)} = E_0^{(m)} + \sum_{\mathbf{r}} \Bigg[& J_2^{(m)} \sum_{\boldsymbol{\rho}} \hat{\mathbf{A}}(\mathbf{r}) \cdot \hat{\mathbf{A}}(\mathbf{r}+\boldsymbol{\rho}) - 5\mathcal{K}^{(m)} \sum_{\boldsymbol{\rho}} \boldsymbol{\mathcal{Q}}(\mathbf{r}) \cdot \boldsymbol{\mathcal{Q}}(\mathbf{r}+\boldsymbol{\rho}) \\
& + \frac{1}{2}\mathcal{K}^{(m)} \sum_{\boldsymbol{\rho}_1 \neq \boldsymbol{\rho}_2} \hat{\mathbf{A}}(\mathbf{r}+\boldsymbol{\rho}_1) \cdot \hat{\mathbf{A}}(\mathbf{r}+\boldsymbol{\rho}_2) \\
& + \mathcal{K}^{(m)} \sum_{\boldsymbol{\rho}_1 \neq \boldsymbol{\rho}_2} \hat{\mathbf{A}}^T(\mathbf{r}+\boldsymbol{\rho}_1)\boldsymbol{\mathcal{Q}}(\mathbf{r})\hat{\mathbf{A}}(\mathbf{r}+\boldsymbol{\rho}_2) \Bigg]. \qquad (7.24)
\end{aligned}$$

Finally, by grouping similar terms together we can write eq. (7.24) in a compact form as

---

[6] *i.e.* in the same sense that a vector would have a direction.

$$\mathcal{H}_{\text{eff}}^{(m)} = E_0^{(m)} + \mathcal{H}_D^{(m)} + \mathcal{H}_Q^{(m)} + \mathcal{H}_{DQ}^{(m)}, \tag{7.25}$$

$$\mathcal{H}_D^{(m)} = \frac{1}{2}\sum_{\mathbf{r}\boldsymbol{\rho}} \mathcal{J}_D^{(m)}(\boldsymbol{\rho})\hat{\mathbf{A}}(\mathbf{r})\cdot\hat{\mathbf{A}}(\mathbf{r}+\boldsymbol{\rho}), \tag{7.26}$$

$$\mathcal{H}_Q^{(m)} = \frac{1}{2}\sum_{\mathbf{r}\boldsymbol{\rho}} \mathcal{J}_Q^{(m)}(\boldsymbol{\rho})\boldsymbol{\mathcal{Q}}(\mathbf{r})\cdot\boldsymbol{\mathcal{Q}}(\mathbf{r}+\boldsymbol{\rho}), \tag{7.27}$$

$$\mathcal{H}_{DQ}^{(m)} = \frac{1}{2}\sum_{\mathbf{r}\boldsymbol{\rho}_1\boldsymbol{\rho}_2} \mathcal{J}_{DQ}^{(m)}(\boldsymbol{\rho};\boldsymbol{\rho}')\hat{\mathbf{A}}^T(\mathbf{r}+\boldsymbol{\rho})\boldsymbol{\mathcal{Q}}(\mathbf{r})\hat{\mathbf{A}}(\mathbf{r}+\boldsymbol{\rho}'), \tag{7.28}$$

where $\mathcal{H}_D^{(m)}$, $\mathcal{H}_Q^{(m)}$, and $\mathcal{H}_{DQ}^{(m)}$ are the dipole-dipole, quadrupole-quadrupole, and dipole-quadrupole interactions, respectively.

7.5 Qualitative description of the effective interactions

The multipolar terms in the effective model in eq. (7.25) significantly complicate the analysis of the ground state. Here, we will analyze each of the three effective interactions in order to get a better idea about which states might be favoured by our model.

7.5.1 Dipole-dipole interactions

The first type of the effective couplings is the familiar exchange-like dipolar interaction. To get an idea of which states this interaction might select, it is helpful to introduce lattice Fourier transforms of the form

$$\hat{\mathbf{A}}(\mathbf{r}) = \frac{1}{\sqrt{N}}\sum_{\mathbf{q}} \mathbf{A}(\mathbf{q})e^{i\mathbf{q}\cdot\mathbf{r}}. \tag{7.29}$$

The Fourier transform simplifies the dipole-dipole interactions to

$$\mathcal{H}_D^{(m)} = \frac{1}{2}\sum_{\mathbf{q}} \mathcal{J}_D^{(m)}(\mathbf{q})\mathbf{A}(\mathbf{q})\mathbf{A}(-\mathbf{q}), \tag{7.30}$$

where

$$\mathcal{J}_D^{(m)}(\mathbf{q}) = \sum_{\boldsymbol{\rho}} \mathcal{J}_D^{(m)}(\boldsymbol{\rho})e^{i\mathbf{q}\cdot\boldsymbol{\rho}}. \tag{7.31}$$

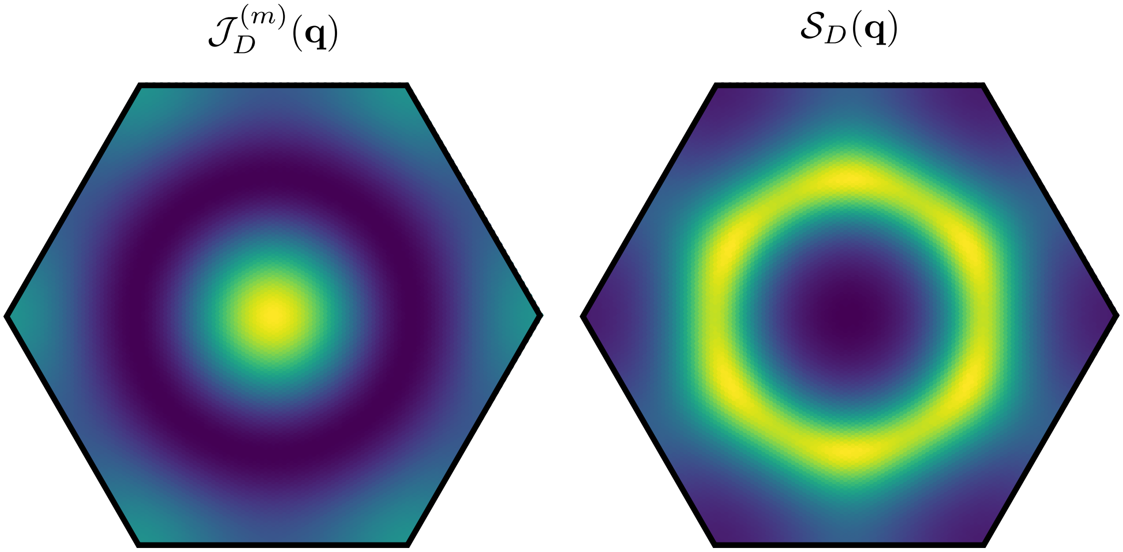

Figure 7.2: Plots of $\mathcal{J}_D^{(m)}(\mathbf{q})$, $m = 2$ in eq. (7.31) and $\mathcal{S}_D(\mathbf{q})$ in eq. (7.32) calculated using the MC simulations at $T = 0.25$ (see Chapter 8 for details). In both cases we used $J_1 = 1$, $J_2 = 1$, $D_1 = -1$, and $D_2 = -0.5$. In both cases we have $q_z = 0$. The intensity values of the two plots are different, but the colour scheme is consistent in both cases and chosen such that the dark and bright colours represent low and high values, respectively.

The $\mathcal{J}_D^{(m)}(\mathbf{q})$ gives the energy of the Fourier amplitudes $\mathbf{A}(\mathbf{q})$ corresponding to wavevector $\mathbf{q}$. Therefore, the ground state of $\mathcal{H}_D^{(m)}$ will typically consist of the amplitudes at the wavevectors that minimize $\mathcal{J}_D^{(m)}(\mathbf{q})$[7]. In fig. 7.2, we plot $\mathcal{J}_D^{(m)}(\mathbf{q})$ for $\mathbf{q} = [q_x, q_y, 0]$. Note that the minima of this function form a degenerate “ring” of incommensurate wavevectors. This ring feature is consistent with the Fourier transforms of the structure factors of the Ising-like phases,

$$\mathcal{S}_D(\mathbf{q}) = \frac{1}{N}\langle \mathbf{A}(\mathbf{q}) \cdot \mathbf{A}(-\mathbf{q})\rangle, \tag{7.32}$$

observed in the MC simulations (figs. 5.3 and 7.2). Note that the maxima of $\mathcal{S}_D(\mathbf{q})$ occur at the locations of the minima in $\mathcal{J}_D^{(m)}(\mathbf{q})$. The minimum value of $\mathcal{J}_D^{(m)}(\mathbf{q})$ at

---

[7] This is the so-called *Luttinger-Tisza* [130–132] or, equivalently, a *mean-field* analysis [133] of a spin Hamiltonian. By minimizing $\mathcal{J}_D^{(m)}(\mathbf{q})$ we obtain the lowest energy single-$\mathbf{Q}$ state. The disadvantage of this method is that it does not take into account the normalized magnitudes of spin vectors and therefore may often predict an unphysical ground state. It is, nevertheless, useful in the context of mean-field, where we deal with thermal averages and don’t require strict normalization of variables.

each wavevector in this ring can be calculated to be

$$\min(\mathcal{J}_D^{(m)}(\mathbf{q})) = -6\mathcal{K}^{(m)} - \frac{\left(J_2^{(m)}\right)^2}{\mathcal{K}^{(m)}}. \tag{7.33}$$

Therefore, there are many degenerate incommensurate structures that can form in the system, which could support the emergence of disorder[8].

7.5.2 Qudrupole-quadrupole interactions

We can perform the same Fourier analysis on the quadrupole-quadrupole interactions. Defining the quadrupole amplitudes according to

$$\boldsymbol{\mathcal{Q}}(\mathbf{r}) = \frac{1}{\sqrt{N}} \sum_{\mathbf{q}} \boldsymbol{\mathcal{Q}}(\mathbf{q}) e^{i\mathbf{q}\cdot\mathbf{r}}, \tag{7.34}$$

we obtain

$$\mathcal{H}_Q^{(m)} = \frac{1}{2} \sum_{\mathbf{q}} \mathcal{J}_Q^{(m)}(\mathbf{q}) \boldsymbol{\mathcal{Q}}(\mathbf{q}) \boldsymbol{\mathcal{Q}}(-\mathbf{q}), \tag{7.35}$$

where, similarly,

$$\mathcal{J}_Q^{(m)}(\mathbf{q}) = \sum_{\boldsymbol{\rho}} \mathcal{J}_Q^{(m)}(\boldsymbol{\rho}) e^{i\mathbf{q}\cdot\boldsymbol{\rho}}. \tag{7.36}$$

As we discussed before, these interactions favour nematic arrangements of $\hat{\mathbf{A}}(\mathbf{r})$, *i.e.* both ferromagnetic and antiferromagnetic collinear configurations. This corresponds to a minimum at $\mathbf{q} = \Gamma$ of $\mathcal{J}_Q^{(m)}(\mathbf{q})$, as shown in fig. 7.3. This is consistent with the numerically calculated quadrupolar structure factor,

$$\mathcal{S}_Q(\mathbf{q}) = \frac{1}{N} \langle \boldsymbol{\mathcal{Q}}(\mathbf{q}) \cdot \boldsymbol{\mathcal{Q}}(-\mathbf{q}) \rangle, \tag{7.37}$$

as shown in fig. 7.3. The minimum value of $\mathcal{J}_Q^{(m)}(\mathbf{q})$ is

---

[8] Recall that the effective model in eq. (7.25) is an approximation for $|D_2^{(m)}|/|J_1^{(m)}| < 1$, $|J_2^{(m)}|/|J_1^{(m)}| \ll 1$. Higher-order corrections will likely break the degeneracy of the ring in $\mathcal{J}_D^{(m)}(\mathbf{q})$, stabilizing a discrete number of wavevectors. However, this splitting is likely to be small, which could lead to metastable configurations.

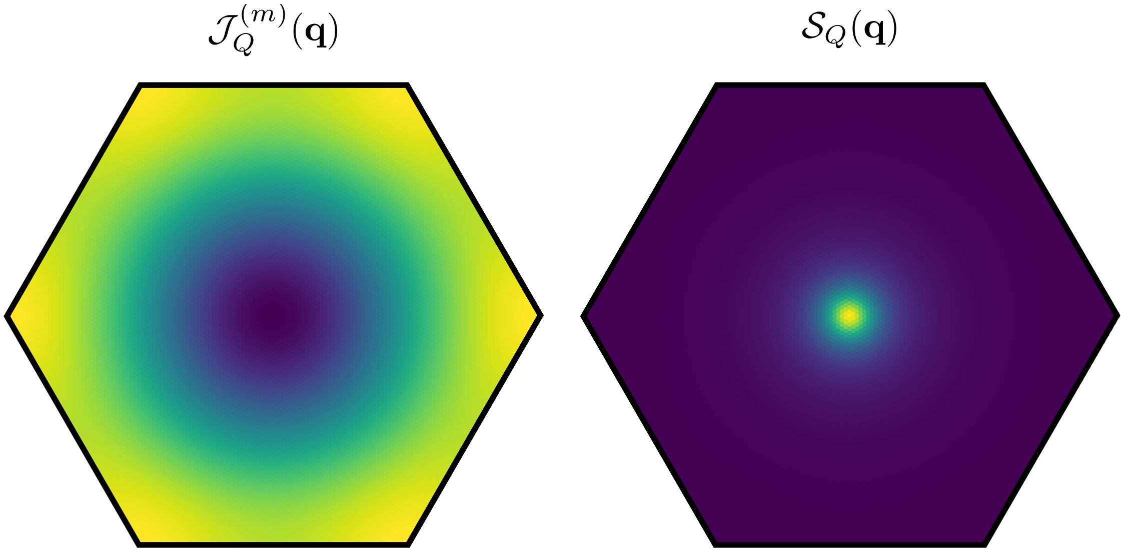

Figure 7.3: Plots of $\mathcal{J}_Q^{(m)}(\mathbf{q})$, $m = 2$ in eq. (7.36) and $\mathcal{S}_Q(\mathbf{q})$ in eq. (7.37), calculated using the same parameters as in fig. 7.2.

$$\min(\mathcal{J}_Q^{(m)}(\mathbf{q})) = -15\mathcal{K}^{(m)}, \tag{7.38}$$

which is almost three times lower than $\min(\mathcal{J}_D^{(m)}(\mathbf{q}))$, for all values of $J_2^{(m)}$. Since there is no direct competitions between $\mathcal{H}_D^{(m)}$ and $\mathcal{H}_Q^{(m)}$, the quadrupolar interactions set the nematic order, while the dipolar interactions select collinear states characterized by wavevectors on the degenerate ring, $\min(\mathcal{J}_D^{(m)}(\mathbf{q}))$, which, in turn, creates the Ising-like patterns. Note that nematic order means that $\hat{\mathbf{A}}(\mathbf{r}) = v(\mathbf{r})\hat{\mathbf{n}}$, where $v(\mathbf{r}) = \pm 1$ and $\hat{\mathbf{n}}$ is the director, pointing in an arbitrary direction. This leads to

$$\mathcal{H}_D^{(m)} = \frac{1}{2}\sum_{\mathbf{r}\boldsymbol{\rho}} \mathcal{J}_D^{(m)}(\boldsymbol{\rho}) v(\mathbf{r}) v(\mathbf{r}+\boldsymbol{\rho}) \tag{7.39}$$

$$\mathcal{H}_Q^{(m)} = 15N\mathcal{K}^{(m)}. \tag{7.40}$$

In other words, $\mathcal{H}_D^{(m)}$ becomes an Ising Hamiltonian, while $\mathcal{H}_Q^{(m)}$ becomes a constant.

7.5.3 Dipole-quadrupole interactions

Finally, the coupling between dipolar and quadrupolar variables, $\mathcal{H}_{DQ}^{(m)}$, is non-local, since it couples variables on three different sites, and cannot be simplified with Fourier transforms. When the system becomes nematic, as discussed above, we obtain

$$\mathcal{H}_{DQ}^{(m)} = \frac{1}{2} \sum_{\mathbf{r}\boldsymbol{\rho}_1\boldsymbol{\rho}_2} \mathcal{J}_{DQ}^{(m)}(\boldsymbol{\rho};\boldsymbol{\rho}')v(\mathbf{r}+\boldsymbol{\rho})v(\mathbf{r}+\boldsymbol{\rho}'), \tag{7.41}$$

which is also an Ising Hamiltonian. Thus, $\mathcal{H}_{DQ}^{(m)}$ enhances the $\mathcal{H}_{D}^{(m)}$ and will modify the radius of the degenerate ring in $\mathcal{J}_{D}^{(m)}(\mathbf{q})$.

To conclude, we note that in Ref. [81] we determined that ignoring these interactions still produces qualitative agreement with the numerical simulations, which might indicate secondary importance of the dipole-quadrupole coupling. However, further numerical analysis is required to fully understand the role of $\mathcal{H}_{DQ}^{(m)}$ in the formation of disordered configurations.

7.6 Summary of important results and open questions

This chapter provides a brief introduction to the physics of the exotic $\boldsymbol{\Lambda}_m$ phases. The main goal of the analysis presented here was to explain the Ising-like character of these structures using analytical coarse-graining of the spin Hamiltonian. This was done by first fixing the $\boldsymbol{\Phi}_m^{(\boldsymbol{\Gamma})}$ spin configurations in each unit cell and then allowing for small deviations from these idealized structures. A simplified version of this method was first introduced in Ref. [80], and a more general scheme, which is described in this chapter, was later devised in Ref. [81]. The coarse-graining procedure revealed that, in a truly remarkable fashion, the DM interactions induce effective biquadratic interactions, which tendto stabilize nematic arrangements, leading to the Ising-like patterns.

The argument for the nematic ordering presented here is largely qualitative and requires further numerical confirmation, which we will provide in the next chapter. Furthermore, simplified versions of the effective model eq. (7.25) (*i.e.* with ferromagnetic dipolar interactions and no dipole-quadrupole coupling) have been studied in other references, which showed separate nematic and Ising phase transitions [134–144].

There are many questions about the nature of the Ising-like phases that remain unanswered. As we mentioned in the beginning of this chapter, the effective model in eq. (7.25) does not provide a clear answer to why the resulting spin configurations lack long-range order. The answer to this question requires comparison of the energy landscape for the effective model and the full Hamiltonian in eq. (7.1). If in both cases we see many degenerate or nearly degenerate states, then it is likely that $\mathcal{H}_{DQ}^{(m)}$ is responsible for the disorder. If, on the other case, the effective Hamiltonian does not produce disordered configurations, then the neglected terms with $J_2^{(m)}$ and $D_2^{(m)}$ in the Hessian (7.14) are important for the full description of the system. Finally, as with other magnetic phases in this thesis, the effects of an applied magnetic field are both interesting and important for the future experimental studies.

Chapter 8

Numerical analysis of the Ising-like phases

> No, no! The adventures first,
> explanations take such a dreadful
> time.
>
> ---
>
> Lewis Carroll,
> *Alice's Adventures in Wonderland*

In the previous chapter, we were able to show via analytical coarse-graining that the DM interactions in AB-SKL systems induce strong effective quadrupolar interactions that would explain the Ising-like nature of the $\mathbf{\Lambda}_m$ phases. To analyze the validity of the approximations made in our analysis, it is desirable to compliment these analytical results with numerical data. Therefore, in this chapter, we will present the finite-temperature analysis of the $\mathbf{\Lambda}_4$ phases using the MC methods outlined in Chapter 4. These results can be further generalized to other Ising-like phases with $m \neq 4$, thanks to the self-duality properties of the model discussed in Chapter 3.

The numerical results presented here assume some familiarity with the theory of phase transitions in 2D systems. Appendix D contains a summary of important concepts and provides references to the helpful resources on this topic.

8.1 Methods

8.1.1 Details of the MC simulations

Following the results of Chapter 5, which demonstrated that in all of the observed ground state phases the spin configurations assumed $Q_z = 0$, in this chapter, we will study the thermal properties of a single AB-stacked kagome bilayer. This simplified setup allows us to study large quasi-2D systems with $N = L^2$ unit cells, where $18 < L < 108$. However, the energy scale of a bilayer system is different from that of a 3D system, since the latter includes additional inter-layer interactions. As a result, in order to match the properties of a bilayer system with the phase diagrams in fig. 5.8, we have to double the inter-layer interactions, J_1 and D_1. In this work, we set $J_1 = 2$, $J_2 = 1$, and $D_1 = -2$, $D_2 = -0.5$, which corresponds to a point on the $\mathbf{\Lambda}_4$ phase on diagram (a) in fig. 5.8. As before, the temperature values are set in units of $|J_2|$.

To achieve high-quality numerical data, we use $\sim 10^4$ MC steps to equilibrate the system at every temperature, and then $\sim 10^5$ steps to calculate the thermodynamic averages. Microcanonical overupdates (Sec. 4.4) were shown to improve the quality of averages, especially in the case of the correlation functions. After each MC step we performed 4-7 over-relaxation updates to generate a sufficiently broad distribution of spin configurations.

8.1.2 Quantities of interest

Heat capacity

Since there is no trivial order parameter for the Ising-like patterns, we considered a number of quantities to help us understand the properties of the system. The simplest of these are the average energy $\langle E \rangle$ and the heat capacity per spin:

$$C_v = \frac{\beta^2}{6N}(\langle E^2 \rangle - \langle E \rangle^2), \tag{8.1}$$

where, as before, $6N$ gives the total number of spins.

As discussed in the Appendix D.2, at the phase transition point the heat capacity becomes singular. However, this singularity is strictly valid for the thermodynamic limit ($N \rightarrow \infty$). In a finite-size system, it is often smoothed down, and may appear as a broadened maximum. This makes the analysis of the phase transitions more difficult, since other crossover phenomena that are not related to phase transitions may sometimes result in a maximum in C_v[1]. To overcome this challenge, it is important to consider how the heat capacity (and other thermodynamic quantities) scales as the system size increases. This type of *finite-size* analysis is often able to identify and characterize the phase transitions in a given system.

---

[1] For example, a simple two-level system leads to a well-known *Schottky anomaly*, which does not correspond to a phase transition.

Energy components

One of the most challenging problems in the studies of the continuous spin systems is the identification of weak first-order transitions. When the energy difference between the ordered and disordered phases is small, the average energy may appear continuous, which may lead to incorrect conclusions about the order of the phase transition. This issue is even more significant in the finite systems, which makes the MC studies of these transitions difficult. A famous example of this is the phase transition that occurs in the antiferromagnetic triangular lattice with three-component (Heisenberg) spins. The order of this transition was a subject of a 30 year controversy, until it was resolved first by studies of short-time dynamics [145], and then by high-precision numerical MC calculations [146,147]. Thanks to this controversy, a considerable effort was put into developing numerical tools for studying weak first-order transitions.

One of the most successful tests of a first-order transition consists of collecting histograms of the total energy at the transition temperature. If there are several states that co-exist at this temperature (*e.g.* a disordered and ordered states), the energy histogram will display several peaks (one for each state), which would indicate a first-order transition. However, if the energies of these states are similar, the multiple-peak feature could be more difficult to resolve. In these situations, it is helpful to consider histograms of other quantities that may better distinguish the different states in the simulation. In this work, we found that analyzing histograms of different energy contributions to be more effective than looking at the total energy. In particular, the self-dual in-plane exchange interactions, corresponding to the $\mu_2^{(+1,+1)}$ in eq. (3.24) with a coupling constant $J_2^{(4)}$, were proven to be very useful in characterizing the nature of the phase transitions in our system.

Chirality

Next, we would like to define quantities that could help us to analyze the average properties of the Ising-like configurations. As discussed in the previous chapter and seen from figs. 7.1, the spin structure of the $\mathbf{\Lambda}_4$ in each unit cell corresponds to approximately $\mathbf{\Phi}_4^{(\mathbf{\Gamma})}$. Since the resulting 120 degree configuration is chiral, it is useful to define a measure of chirality in each cell. For a single triangle, the vector chirality is typically defined [148, 149] as

$$\boldsymbol{\chi}_t = \frac{2}{3\sqrt{3}} \left[\mathbf{S}_1 \times \mathbf{S}_2 + \mathbf{S}_2 \times \mathbf{S}_3 + \mathbf{S}_3 \times \mathbf{S}_1 \right], \tag{8.2}$$

where $\mathbf{S}_i$ are spins on a triangle and indices indicate clockwise or anti-clockwise direction (depending on notation). The constant in front of the expression is used to normalize the vector. For AB-stacked kagome, we can define chirality in a given unit cell as

$$\begin{aligned} \boldsymbol{\chi}(\mathbf{r}) = \frac{1}{3\sqrt{3}} \Big[& \mathbf{S}_1(\mathbf{r}) \times \mathbf{S}_2(\mathbf{r}) + \mathbf{S}_2(\mathbf{r}) \times \mathbf{S}_3(\mathbf{r}) + \mathbf{S}_3(\mathbf{r}) \times \mathbf{S}_1(\mathbf{r}) \\ & + \mathbf{S}_4(\mathbf{r}) \times \mathbf{S}_5(\mathbf{r}) + \mathbf{S}_5(\mathbf{r}) \times \mathbf{S}_6(\mathbf{r}) + \mathbf{S}_6(\mathbf{r}) \times \mathbf{S}_4(\mathbf{r}) \Big]. \end{aligned} \tag{8.3}$$

The z-component of $\boldsymbol{\chi}(\mathbf{r})$ is an invariant[2], and thus we define $\chi(\mathbf{r}) = \hat{\mathbf{z}} \cdot \boldsymbol{\chi}(\mathbf{r})$. The average unit cell chirality per cell is defined as

$$\langle \chi \rangle = \frac{1}{N} \sum_{\mathbf{r}} \langle \chi(\mathbf{r}) \rangle. \tag{8.4}$$

Since the DM interactions generally select one type of chirality, we may be interested in calculating the average sign of chirality,

$$\langle \mathrm{sgn}(\chi) \rangle = \frac{1}{N} \sum_{\mathbf{r}} \langle \mathrm{sgn}\left(\chi(\mathbf{r}) \right) \rangle, \tag{8.5}$$

which provides information about the presence of domains with opposite chirality.

Local order parameter

In the previous chapter, we derived an effective model for the Ising-like systems, described by the unit vectors $\hat{\mathbf{A}}(\mathbf{r})$, which describe the in-plane rotations of spins in each unit cell. To test the analytical predictions, we would like to obtain average quantities written in terms of these unit vectors from the MC simulations. However, calculating the in-plane rotation angles of the six sublattices is computationally expensive, since it requires a frequent use of inverse trigonometric functions. We also

---

[2] This is because the definition of the chirality in eq. (8.3) is proportional to the cross products in the intra-layer DM interactions in eq. (2.30).

noticed that the values calculated using this direct method tend to be very noisy and require more MC steps to resolve the averages.

A simpler and quicker approach is to study a quantity defined as a linear combination of the spin vectors

$$\mathbf{A}(\mathbf{r}) = \frac{1}{6}\sum_i \begin{bmatrix} \hat{\mathbf{n}}_{ix}^{(4)} \cdot \mathbf{S}_i(\mathbf{r}) \\ \hat{\mathbf{n}}_{iy}^{(4)} \cdot \mathbf{S}_i(\mathbf{r}) \end{bmatrix}, \tag{8.6}$$

where

$$\hat{\mathbf{n}}_{ix}^{(4)} = \begin{bmatrix} \cos(4\alpha_i) \\ \sin(4\alpha_i) \\ 0 \end{bmatrix}, \hat{\mathbf{n}}_{iy}^{(4)} = \begin{bmatrix} -\sin(4\alpha_i) \\ \cos(4\alpha_i) \\ 0 \end{bmatrix}, \tag{8.7}$$

and α_i are defined in eq. (2.36). We will refer to these vectors as the *local order parameters* (LOPs). These vectors are not normalized since the magnitude $|\mathbf{A}(\mathbf{r})|$ can range between 0 and 1. However, if we define the in-plane spin angles as $\theta_i(\mathbf{r}) = \theta(\mathbf{r}) + \delta\theta_i(\mathbf{r})$, one can show that

$$\frac{\mathbf{A}(\mathbf{r}) \cdot \mathbf{A}(\mathbf{r}')}{|\mathbf{A}(\mathbf{r})||\mathbf{A}(\mathbf{r}')|} \approx \cos\bigl(\theta(\mathbf{r}) - \theta(\mathbf{r}')\bigr) = \hat{\mathbf{A}}(\mathbf{r}) \cdot \hat{\mathbf{A}}(\mathbf{r}'). \tag{8.8}$$

This approximation is further improved by considering the thermal averages of these quantities. Therefore, in the remainder of this chapter, we will assume that

$$\frac{1}{|\mathbf{A}(\mathbf{r})|}\mathbf{A}(\mathbf{r}) \equiv \hat{\mathbf{A}}(\mathbf{r}). \tag{8.9}$$

The average magnitude of the LOPs is defined as

$$\langle|\mathbf{A}|^2\rangle = \frac{1}{N}\sum_{\mathbf{r}}\langle|\mathbf{A}(\mathbf{r})|^2\rangle, \tag{8.10}$$

and we can further calculate the fluctuations in the magnitude via

$$C_{|\mathbf{A}|} = \frac{1}{N}\sum_{\mathbf{r}}\Bigl\langle \Bigl(|\mathbf{A}(\mathbf{r})|^2 - \langle|\mathbf{A}(\mathbf{r})|^2\rangle\Bigr)^2 \Bigr\rangle, \tag{8.11}$$

which will help us to test the approximation in eq. (8.9). Since the magnitude of the LOP vectors does not depend on their orientation, the $C_{|\mathbf{A}|}$ can be viewed as a measure of the longitudinal fluctuations. The correlations between the transverse modes of the LOPs are defined as

$$\mathcal{S}_D(\boldsymbol{\rho}) = \frac{1}{N}\sum_{\mathbf{r}} \big\langle \hat{\mathbf{A}}(\mathbf{r}) \cdot \hat{\mathbf{A}}(\mathbf{r}+\boldsymbol{\rho})\big\rangle, \tag{8.12}$$

where $\boldsymbol{\rho} = \mathbf{r} - \mathbf{r}$. In terms of distance, this function reads

$$\mathcal{S}_D(\rho) = \frac{1}{N_\rho}\sum_{\hat{\boldsymbol{\rho}}} \left|\mathcal{S}_D(\boldsymbol{\rho})\right|, \tag{8.13}$$

where $\rho = |\boldsymbol{\rho}|$, and the sum is taken over all equivalent neighbors (N_ρ in total) separated by distance ρ. The absolute value inside the sum is taken for plotting conveniences. Since the $\mathbf{A}(\mathbf{r})$ vectors lie on a triangular lattice, one can define a Fourier transform:

$$\mathbf{A}(\mathbf{q}) = \frac{1}{N}\sum_{\mathbf{r}} \hat{\mathbf{A}}(\mathbf{r}) e^{-i\mathbf{q}\cdot\mathbf{r}}. \tag{8.14}$$

In the Fourier form, the LOP correlation function reads

$$\mathcal{S}_D(\mathbf{q}) = \frac{1}{N}\big\langle \mathbf{A}(\mathbf{q}) \cdot \mathbf{A}(-\mathbf{q})\big\rangle, \tag{8.15}$$

which is the same as in eq. (7.32) in the previous chapter. Since at low temperatures the Ising-like structures tend to select wavevectors lying on a ring with radius Q, we can calculate average correlation functions at $\mathbf{Q} = Q\hat{\mathbf{Q}}$, where $\hat{\mathbf{Q}}$ is parallel to either the $\Gamma-$M line or the $\Gamma-$K line. The two averages are then defined as

$$\langle|\mathbf{A}(\mathbf{Q}_{\Gamma-\mathrm{M}})|^2\rangle = \frac{1}{6N}\sum_{\hat{\mathbf{q}}\in\mathbf{Q}_{\Gamma-\mathrm{M}}} \langle|\mathbf{A}(\mathbf{q})|^2\rangle, \tag{8.16}$$

$$\langle|\mathbf{A}(\mathbf{Q}_{\Gamma-\mathrm{K}})|^2\rangle = \frac{1}{6N}\sum_{\hat{\mathbf{q}}\in\mathbf{Q}_{\Gamma-\mathrm{K}}} \langle|\mathbf{A}(\mathbf{q})|^2\rangle, \tag{8.17}$$

where the sums are over the six symmetry-equivalent directions in the Brillouin zone. These averages can be viewed as the approximate dipolar order parameters[3].

---

[3] Similar to the previous section, we use "dipolar" order parameter in the sense of the multipole expansions, *i.e.* as opposed to the quadrupolar order parameter, which lacks a sense of vector direction.

Quadrupole moment

The quadrupole moment is a 2 × 2 tensor, which is defined in eq. (7.21). In the simulations, we will consider the average magnitude of the quadrupole moment:

$$\begin{aligned}\langle \boldsymbol{\mathcal{Q}}^2 \rangle &= \frac{1}{N} \sum_{\mathbf{r}} \big\langle \boldsymbol{\mathcal{Q}}(\mathbf{r}) \cdot \boldsymbol{\mathcal{Q}}(\mathbf{r}) \big\rangle \\ &= \frac{1}{N} \sum_{\mathbf{r}} \sum_{\alpha\beta} \big\langle \mathcal{Q}^2_{\alpha\beta}(\mathbf{r}) \big\rangle, \end{aligned} \tag{8.18}$$

where the dot product is assumed to be analagous to the vector dot product. The quadrupolar correlations can be defined in a similar way to the dipolar ones:

$$\mathcal{S}_Q(\boldsymbol{\rho}) = \frac{1}{N} \sum_{\mathbf{r}} \big\langle \boldsymbol{\mathcal{Q}}(\mathbf{r}) \cdot \boldsymbol{\mathcal{Q}}(\mathbf{r} + \boldsymbol{\rho}) \big\rangle, \tag{8.19}$$

$$\mathcal{S}_Q(\rho) = \frac{1}{N_\rho} \sum_{\hat{\boldsymbol{\rho}}} \mathcal{S}_Q(\boldsymbol{\rho}), \tag{8.20}$$

$$\mathcal{S}_Q(\mathbf{q}) = \frac{1}{N} \big\langle \boldsymbol{\mathcal{Q}}(\mathbf{q}) \cdot \boldsymbol{\mathcal{Q}}(-\mathbf{q}) \big\rangle, \tag{8.21}$$

with

$$\boldsymbol{\mathcal{Q}}(\mathbf{q}) = \frac{1}{N} \sum_{\mathbf{r}} \boldsymbol{\mathcal{Q}}(\mathbf{r}) e^{-i\mathbf{q}\cdot\mathbf{r}}. \tag{8.22}$$

Note that the quadrupolar correlation function is defined in the same way as the structure factor in eq. (7.37).

Collinearity parameter

In addition to the LOP quadrupole moment, it is useful to define a measure of the local nematic order. We consider the following overlap function:

$$\psi(\mathbf{r}) = \frac{1}{3} \sum_{\boldsymbol{\rho}} \big\langle \boldsymbol{\mathcal{Q}}(\mathbf{r}) \cdot \boldsymbol{\mathcal{Q}}(\mathbf{r} + \boldsymbol{\rho}) \big\rangle \tag{8.23}$$

$$= \frac{1}{6} \sum_{\boldsymbol{\rho}} \left\langle 2 \left(\hat{\mathbf{A}}(\mathbf{r}) \cdot \hat{\mathbf{A}}(\mathbf{r} + \boldsymbol{\rho}) \right)^2 - 1 \right\rangle, \tag{8.24}$$

where the sum is taken over the nearest neighbours. The lattice-averaged value of $\psi(\mathbf{r})$ is given by

$$\langle \psi \rangle = \frac{1}{N} \sum_{\mathbf{r}} \psi(\mathbf{r}). \tag{8.25}$$

We will refer to $\psi(\mathbf{r})$ as the *collinearity parameter*.

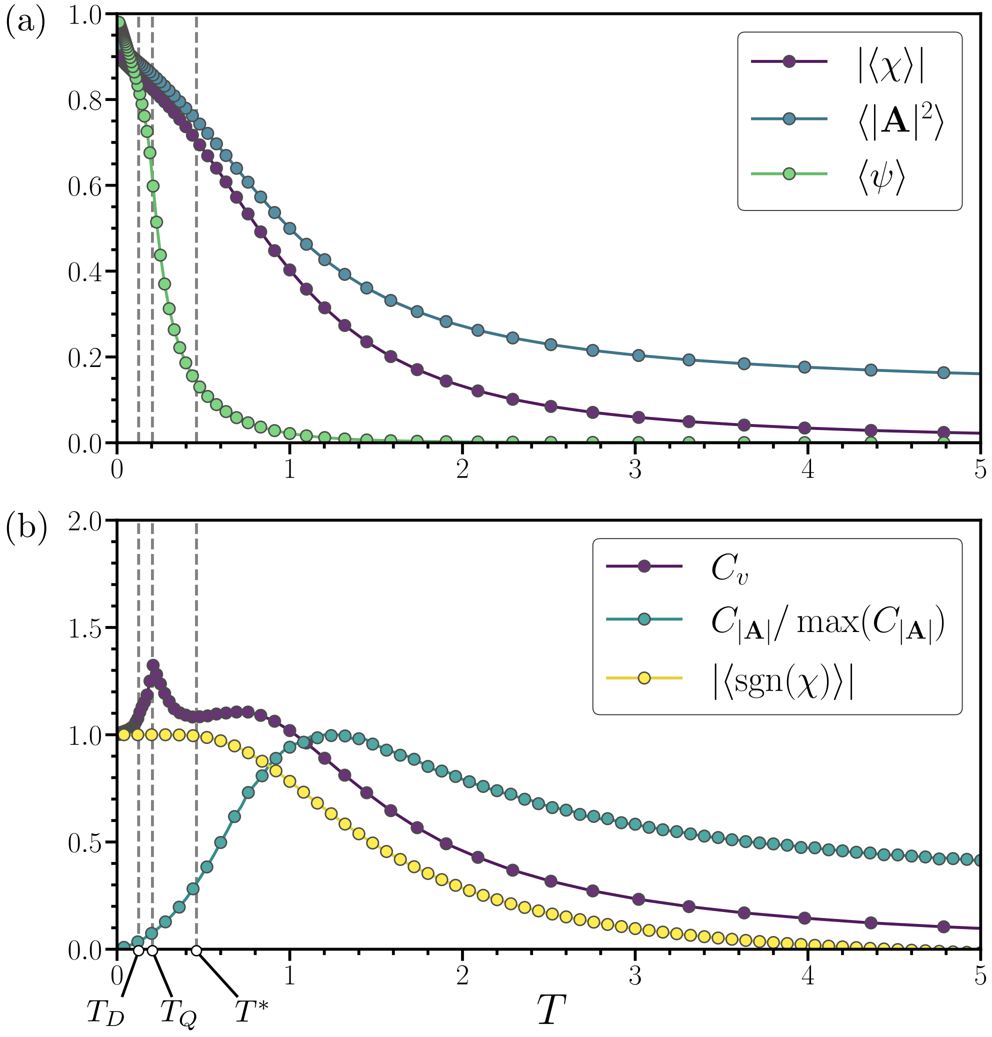

Figure 8.1: Thermodynamic averages of the relevant quantities, defined in Sec. 8.1.2. (a) Average chirality ($\langle\chi\rangle$), magnitude of the LOP ($\langle|\mathbf{A}|^2\rangle$), and the collinearity parameter ($\langle\psi\rangle$) reflect the evolution of local order. (b) Heat capacity (C_v), fluctuations in the relative LOP magnitude ($C_{|\mathbf{A}|}/\max(C_{|\mathbf{A}|})$), and the distribution of chiral domains ($\langle\mathrm{sgn}(\chi)\rangle$) illustrate the establishment of the chiral paramagnet phase (see text). Grey dashed lines indicate the temperatures at which the system undergoes qualitative changes. All quantities were obtained from MC simulations using $L = 54$. The error bars are much smaller than the markers.

8.2 Chiral paramagnetic phase

We will now discuss the results of the MC simulations. Some of the thermodynamic averages of quantities defined in the previous section are presented over a wide temperature range in fig. 8.1. The system displays qualitative changes at three distinct temperatures, $T^* \approx 0.46$, $T_Q \approx 0.21$, and $T_D \approx 0.13$. Let us first focus on the properties of the system at temperatures $T \geq T^*$.

Note that the average chirality $|\langle\chi\rangle|$ and the average magnitude of the LOPs $\langle|\mathbf{A}|^2\rangle$, plotted in fig. 8.1 (a), both monotonically increase, which signals the formation of the 120 degree $\mathbf{\Phi}_4^{(\mathbf{\Gamma})}$ order in each unit cell. The fluctuations in the magnitude, determined by $C_{|\mathbf{A}|}$, reach a maximum at $T \approx 1.2$ and then decay as the temperature is decreased, as shown in fig. 8.1 (b). We calculate the maximum value of $C_{|\mathbf{A}|}$ to be

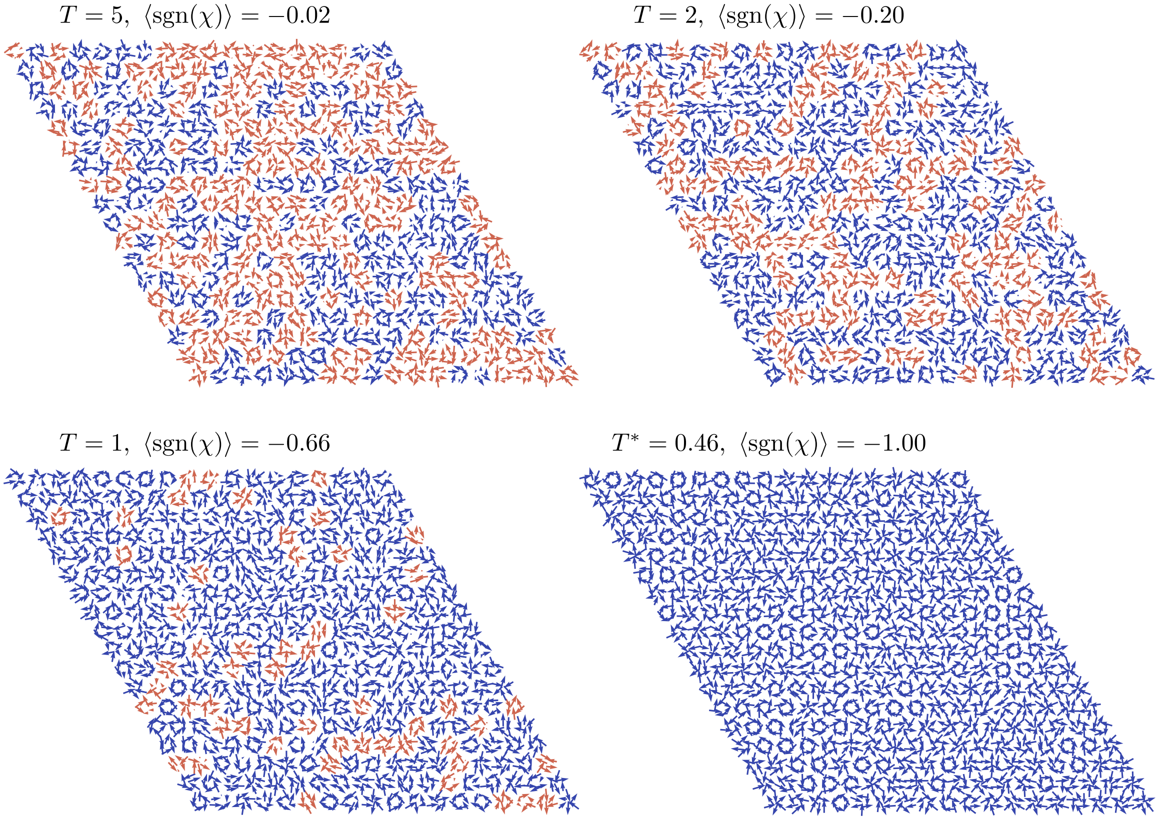

$T = 5,\ \langle \mathrm{sgn}(\chi)\rangle = -0.02$

$T = 2,\ \langle \mathrm{sgn}(\chi)\rangle = -0.20$

$T = 1,\ \langle \mathrm{sgn}(\chi)\rangle = -0.66$

$T^* = 0.46,\ \langle \mathrm{sgn}(\chi)\rangle = -1.00$

Figure 8.2: Snapshots of spin configurations from MC simulations in the region $T \geq T^*$. Blue and pale red represent the cells in which the local spin structure has negative and positive chirality, respectively.

$$\max_T(C_{|\mathbf{A}|}) \sim 5 \times 10^{-5}, \tag{8.26}$$

which suggests that the longitudinal fluctuations of the LOPs remain small at all temperatures. Interestingly, the average sign of the chirality $|\langle \text{sgn}(\chi) \rangle|$ saturates at $T = T^*$, after a broad peak in the heat capacity, as shown in fig. 8.1 (b). The snapshots of the spin configurations in fig. 8.2 display distorted $\mathbf{\Phi}_4^{(\mathbf{\Gamma})}$ structures with an arbitrary phase (*i.e.* rotated in the kagome plane) in each unit cell. Thus, at this temperature, the system forms a single chiral domain with ferromagnetically ordered chirality vectors in each unit cell. At this point, the fluctuations in the magnitude of the LOPs are small, as indicated by the plot of the $C_{|\mathbf{A}|}$. However, both the dipolar and quadrupolar correlation functions, represented by $\mathcal{S}_D(\rho)$ and

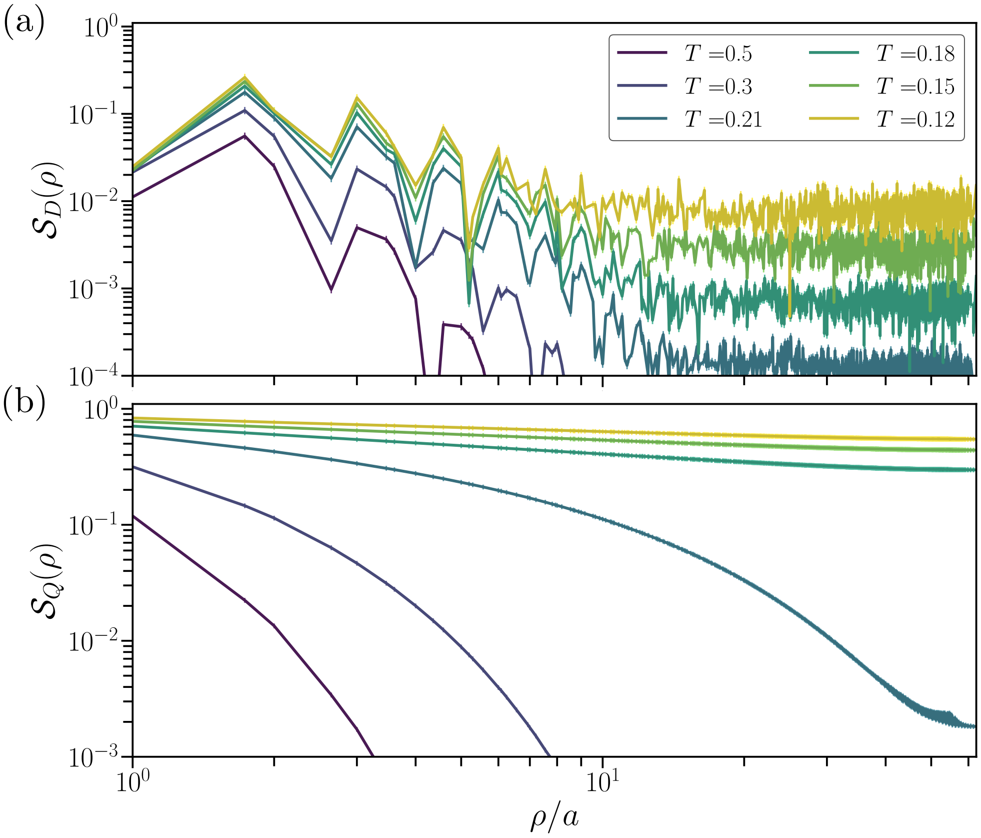

Figure 8.3: Distance dependence of the (a) dipolar and (b) quadrupolar correlation functions calculated at different temperatures for the $L = 108$ system. The temperatures are chosen to analyze the behaviour of the correlation functions above and below $T^* \approx 0.46$, as well as at and below $T_Q \approx 0.21$. Here, ρ/a is the distance per kagome bond length.

$\mathcal{S}_Q(\rho)$ in fig. 8.3 just below T^* display exponential decay with the distance. This implies that despite the apparent ordering of the chiralities, the system continues to fluctuate and the thermal fluctuations are sufficient to destroy the correlations between the LOPs. From the definitions of $\mathcal{S}_D(\rho)$ and $\mathcal{S}_Q(\rho)$ in eq. (8.13) and (8.20), we see that both of these correlation functions reflect the transverse fluctuations of the LOP vectors. Therefore, from the plots of $C_{|\mathbf{A}|}$ (fig. 8.1 (b)), $\mathcal{S}_D(\rho)$ and $\mathcal{S}_Q(\rho)$ (figs. 8.3 (a) and (b) respectively), we conclude that the transverse fluctuations, which correspond to the in-plane rotations of spins, promote the disordered configurations in the temperature region $T_Q < T \leq T^*$. At these temperatures, the system behaves as an XY paramagnet, characterized by the 2-component LOP vectors. Finally, since each $\mathbf{A}(\mathbf{r})$ describes a chiral 120 degree structure, we refer to the state of the system in this temperature region as a *chiral paramagnet*.

The existence of a crossover to the chiral paramagnetic phase validates the analytical coarse-graining procedure that we introduced in the previous chapter. The XY nature of this phase provides a rationale for the omission of the out-of-plane spin components from our calculations, and the smallness of $C_{|\mathbf{A}|}$ further justifies the perturbative analysis. As a result, we expect that the effective model in eq. (7.24) would be most accurate for $T < T^*$.

8.3 Chiral nematic phase

As we further decrease the temperature to $T = T_Q$, the system develops a quadrupole moment, while the heat capacity displays a sharp peak, as shown in figs. 8.4 (a), (b). From the finite-size analysis we see that as the system size increases, the appearance of the quadrupole moment becomes more and more sharp, which is consistent with a continuous phase transition (see Appendix D.2). At the same time, in figs. 8.4 (c), (d), we present the values of $\langle|\mathbf{A}(\mathbf{Q}_{\Gamma-\mathrm{M}})|\rangle$ and $\langle|\mathbf{A}(\mathbf{Q}_{\Gamma-\mathrm{K}})|\rangle$ defined in eqs. (8.16) - (8.17), respectively. Evidently, there is no qualitative change in the behaviour of these functions at T_Q. Moreover, as the system size increases, these values gradually decay, suggesting the absence of the dipolar order in the thermodynamic limit.

A spontaneous quadrupole moment would break the in-plane rotational symmetry

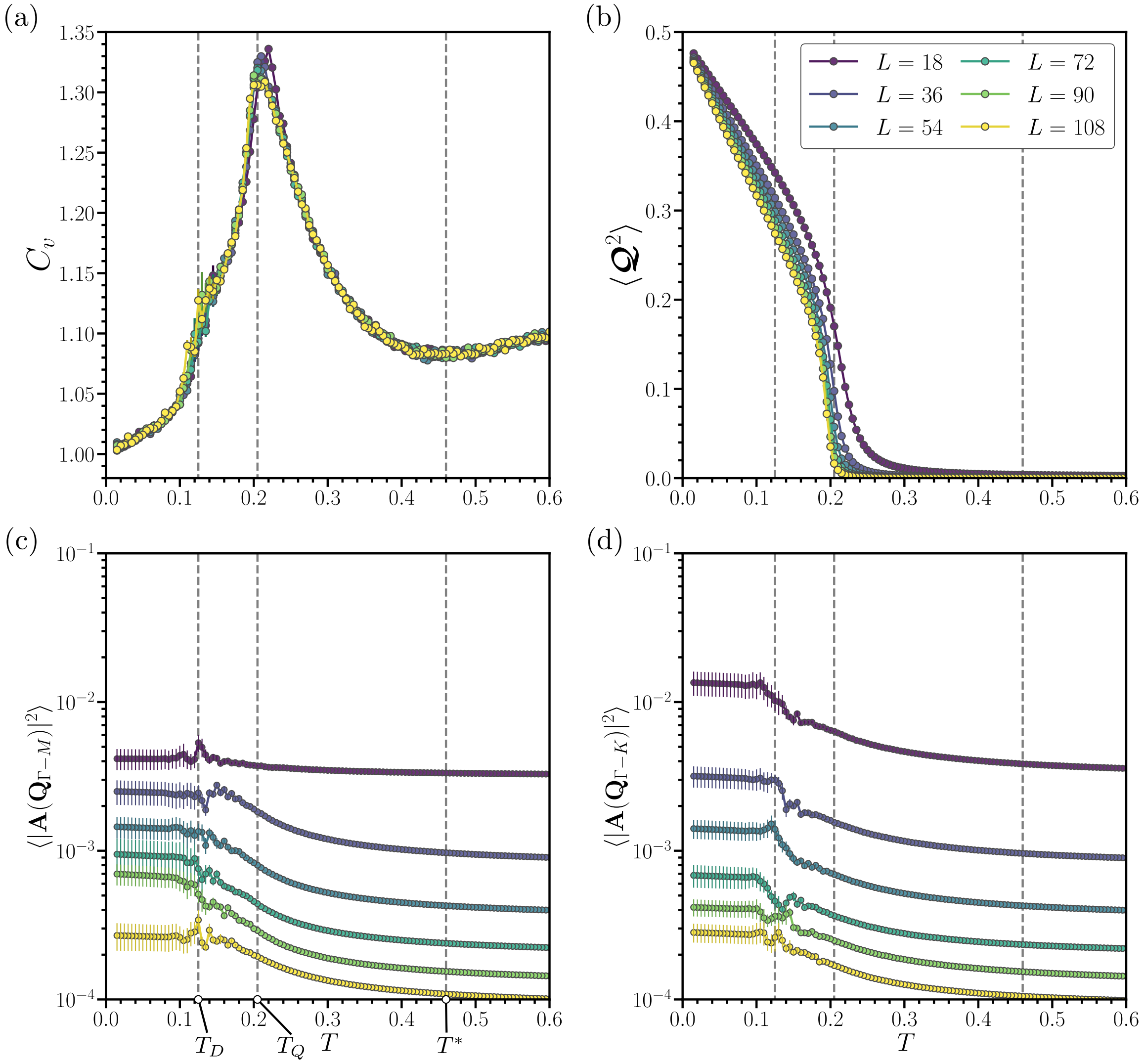

Figure 8.4: Low-temperature finite-size data for (a) heat cpacity, (b) average quadrupole moments, and (c), (d) the dipolar order parameters. The error bars are shown on all plots but are smaller than the markers in sub-plot (b). As before, the grey dashed lines indicate the locations of T^*, T_Q, and T_D (in the order of decreasing temperature).

of the system but remain invariant under the discrete time-reversal symmetry[4]. However, since the system under consideration is quasi-2D, the broken continuous symmetry would contradict the Mermin-Wagner theorem, which states that no broken

---

[4] This is because the quadrupole variables $\mathcal{Q}(\mathbf{r})$ are written as the squares of the components of LOP vectors $\mathbf{A}(\mathbf{r})$, which themselves depend linearly on the spin variables. Since the application of the time-inversion gives $\mathbf{S}_i(\mathbf{r}) \to -\mathbf{S}_i(\mathbf{r})$, it would also lead to $\mathbf{A}(\mathbf{r}) \to -\mathbf{A}(\mathbf{r})$, which, after squaring, leaves the quadrupoles unchanged: $\mathcal{Q}(\mathbf{r}) \to \mathcal{Q}(\mathbf{r})$.

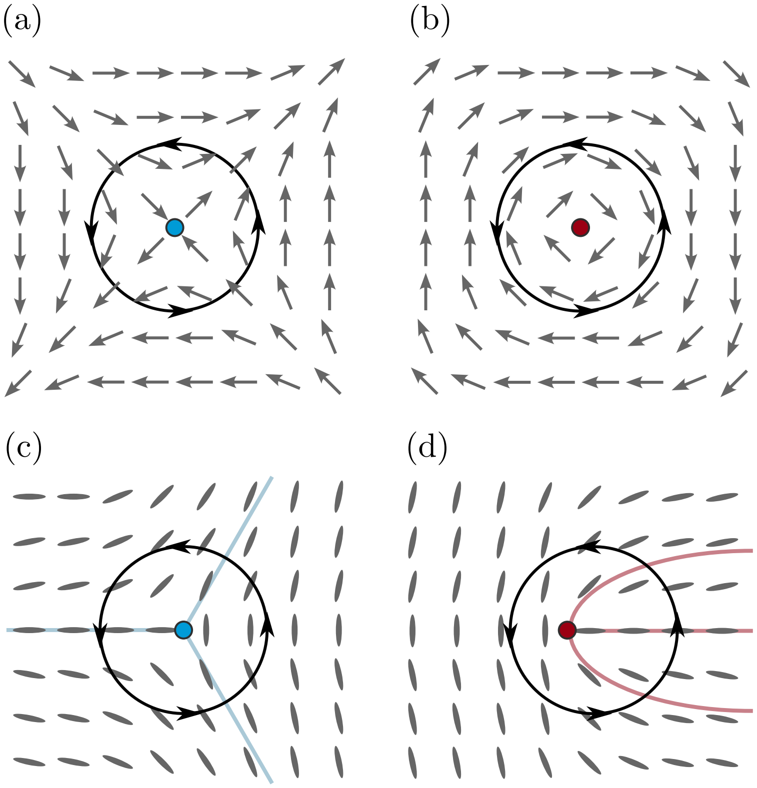

Figure 8.5: Examples of topological defects in XY models. The cores of the defects are represented by small circles (blue and red for negative and positive winding numbers, respectively). Black circles with arrows are drawn around the cores to help identify the winding numbers. (a) and (b) represent respectively an antivortex and vortex defects in an XY ferromagnet, where as we trace a closed loop around the circle, the spins rotate by 2π, leading to winding numbers ± 1. (c) and (d) show nematic defects with negative and positive windings (a disclination and a dislocation), respectively. Given the symmetry of the ellipsoids, a full rotation corresponds to an angle of π, which gives winding numbers $\pm 1/2$. The coloured lines are used to clearly indicate the Y and U defects.

continuous symmetry occurs in systems with dimensions $d \leq 2$ (see Appendix D.4). This is further supported by the plots of the correlation function $\mathcal{S}_Q(\rho)$ at temperatures $T \leq T_Q$ in fig. 8.3 (b), which displays a crossover from an exponential to an algebraic decay, $\mathcal{S}_Q(\rho) \sim \rho^{-\eta(T)}$. Since the correlations decay at temperatures below T_Q, the long-range order is destroyed by the thermal fluctuations, meaning that the observed quadrupolar ordering is only quasi-long-range.

Nevertheless, the existence of a crossover in the decay of the correlations suggests a transition of Kosterlitz-Thouless (KT) type (Appendix D.5). To demonstrate that this transition does, in fact, take place in our system, we need to show the formation of

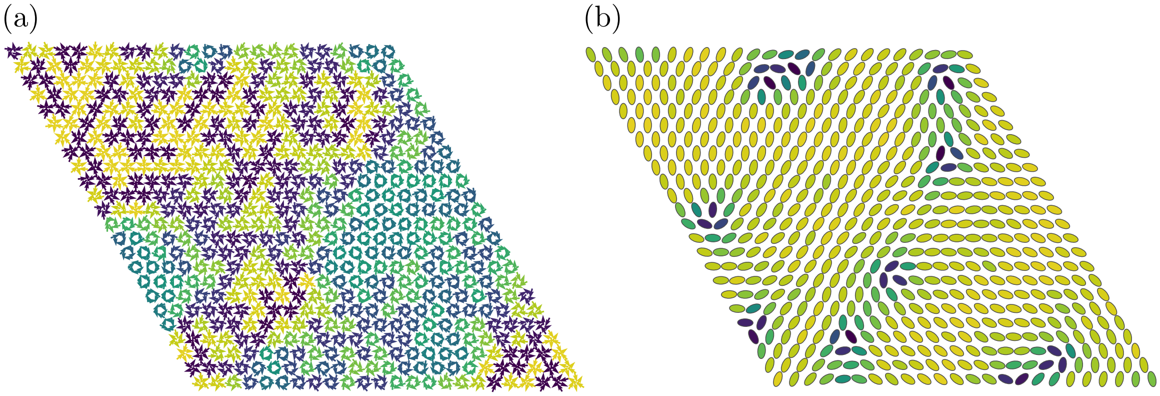

Figure 8.6: Topological defects in the chiral nematic phase. (a) A fragment of the spin structure with the colours determined by $\hat{\mathbf{A}}(\mathbf{r}) \cdot \hat{\mathbf{A}}(0)$ (yellow, green, and purple corresponding to 1, 0, and -1 respectively). (b) the same configuration, where the six sublattices were replaced by the LOPs, represented as ellipses and coloured using $\psi(\mathbf{r})$ function as described in the text. The snapshots were obtained by quickly cooling a $L = 54$ system below $T = T_Q$.

topological defects. In a typical ferromagnetic XY model, these correspond to vortices and antivortices, which are characterized by integer winding numbers (see discussion in Appendix D.5). Examples of these are given in figs. 8.5 (a), (b). However, in the present case, the system displays a quasi-long-range nematic ordering, which changes the nature of the topological defects. Since the quadrupolar order parameter is invariant under the time-reversal (or spin inversion), it is said to be defined up to rotations by π, rather than 2π, as in a regular XY model. Therefore, the rotation of this order parameter by π should count as a single winding. This means that the topological defects in the nematic phase[5] are equivalent to "half-integer vortices", as shown in figs. 8.5 (c),(d). The nematic defects with winding numbers $-1/2$ and $1/2$ are also sometimes called the "Y" and "U" defects, due to their shape.

To obtain the topological defects, we simulate a quick cooling of the spin configurations below $T = T_Q$ and analyze the resulting snapshots of the spin configurations. To provide a better presentation of the quadrupolar order, we replace the spin structure in each unit cell by the corresponding LOP vector $\mathbf{A}(\mathbf{r})$. Furthermore, rather than presenting these as arrows, we instead display ellipsoids, which properly capture

---

[5] Commonly called disclinations in the liquid crystal literature.

the symmetry of the quadrupole moment. Finally, we choose the collinearity parameter $\psi(\mathbf{r})$, defined in eq. (8.24) as a colour map to highlight the regions in space where the LOPs deviate from the collinear arrangements. The resulting structures are presented in fig. 8.6. We see that our simulations reveal pairs of topological defects with winding numbers equal to $\pm 1/2$. The fact that these defects appear as bound pairs (not, for example, a pair of defects in the upper right corner of fig. 8.6 (b)) below $T = T_Q$ qualitatively confirms the KT transition.

These results are quite remarkable since they demonstrate a stabilization of a nematic phase in a magnetic system at a finite temperature. The existence of spin nematics has been hypothesized for a long time, typically through exaggerated models with unusually large biquadratic interactions between the spins [150–156]. To date, there is no experimental evidence that these models could be compatible with realistic magnetic systems [156]. The Ising-like phases in AB-SKL provide a completely different mechanism for stabilizing nematic states, which relies on moderate values of DM interactions and thermal fluctuations. Another important difference comes from the fact that the nematic order described here is also chiral, as a result of the 120 degree structure in each cell. The coexistence of chirality and nematicity is unusual, since they are typically associated with opposite structures (non-collinear and collinear, respectively). Note that this coexistence is not analogous to the cholesteric phase in liquid crystals, since the ordering of the LOPs (in the absence of defects) is precisely collinear and generally does not display any chiral twisting over macroscopic distances [128].

8.4 Nucleation of Ising-like phases

Finally, as the temperature of the system decreases further below T_Q, in the vicinity of $T = T_D$ we observe a series of jumps in the heat capacity, as shown in fig. 8.4 (a). These jumps are also reflected in the plots of the dipolar order parameters, $\langle|\mathbf{A}(\mathbf{Q}_{\Gamma-\mathrm{M}})|\rangle$ and $\langle|\mathbf{A}(\mathbf{Q}_{\Gamma-\mathrm{K}})|\rangle$ (figs. 8.4 (c), (d)), which also acquire larger error bars. The error bars indicate a distribution of structures with distinct spin configurations in different simulations, which is consistent with the formation of the disordered Ising-like patterns. Fig. 8.7 shows the MC snapshots of these structures at different temperatures. We see that the Ising degrees of freedom fluctuate, which leads to dissimilar patterns at each temperatures.

To analyze the nature of this behaviour close to T_D, we collect histograms of the energy components at different temperatures. The energy values, corresponding to the self-dual intra-plane exchange, and labelled as $E_{J_2^{(4)}}$ were shown to be very sensitive to the fluctuations in the Ising-like patterns. In fig. 8.8, we present the histograms of the $E_{J_2^{(4)}}$ at different temperatures. We see that as the temperature is lowered, the histograms start to display multiple peaks, which corresponds to many coexisting configurations. Note that compared to the average energy of about $\langle E \rangle \approx 3.0$, the energy differences between the peaks are quite small. The presence of metastability indicates a weak first-order transition, although in the present case, instead of two coexisting phases (ordered and disordered), there appears to be up to 7 different metastable states at once. This suggests a presence of a complicated free energy landscape, meaning that many distinct Ising-like patterns have very similar energies and are metastable near T_D, which allows thermal fluctuations to drive the system in a sort of a random walk through the configuration space. However, this high configurational entropy could also prevent the system from reaching the true equilibrium state, leaving it stuck in one of the metastable configurations.

The last point that we would like to discuss is the origin of the weak first-order transition. Since the time-reversal symmetry is broken once the Ising-like structures are formed, we would expect a second-order type transition between the chiral nematic and low-temperature Ising-like phases[6]. Therefore, a first-order transition is somewhat surprising. The explanation of this inconsistency comes from the large volume of fluctuations, concentrated along the ring in the Brillouin zone, as seen from the plots of the dipolar correlation functions in fig. 8.7. As discussed in the previous chapter, the dipolar interactions in the effective model in eq. (7.24) yield a quasi-degenerate[7] ring of states. As a result, the thermal fluctuations in the vicinity of this ring cost very little energy, meaning that the Ising degrees of freedom continue to fluctuate as long as the resulting configurations are described by the wavevectors

---

[6] Recall that a broken discrete time-reversal symmetry in a 2D system does not contradict the Mermin-Wagner theorem, since the latter only applies to the continuous symmetries.

[7] As mentioned in the discussion of the last chapter, the neglected terms in the Hessian in eq. (7.14) could yield small effective interactions that break the exact degeneracy of this ring.

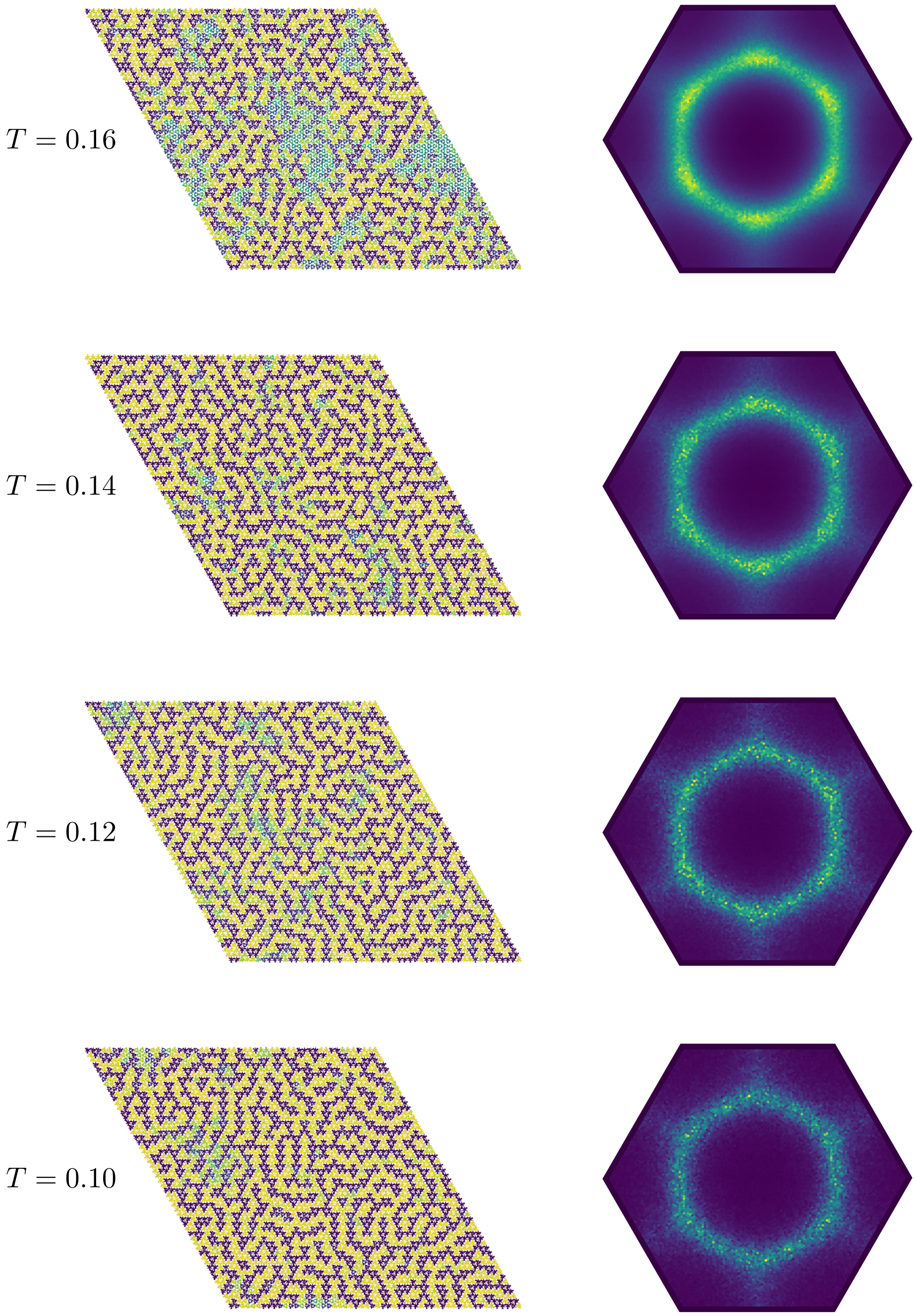

Figure 8.7: Evolution of the spin structure during the nucleation of the Ising-like phases. The snapshots of the spin configurations at the specified temperatures are shown on the left (colour scheme is the same as in fig. 8.6 (a)), and the corresponding plots of the dipolar correlation functions $\mathcal{S}_D(\mathbf{q})$ are presented on the right (brighter colours indicate higher intensity). The results are obtained from the MC simulations of the $L = 108$ systems.

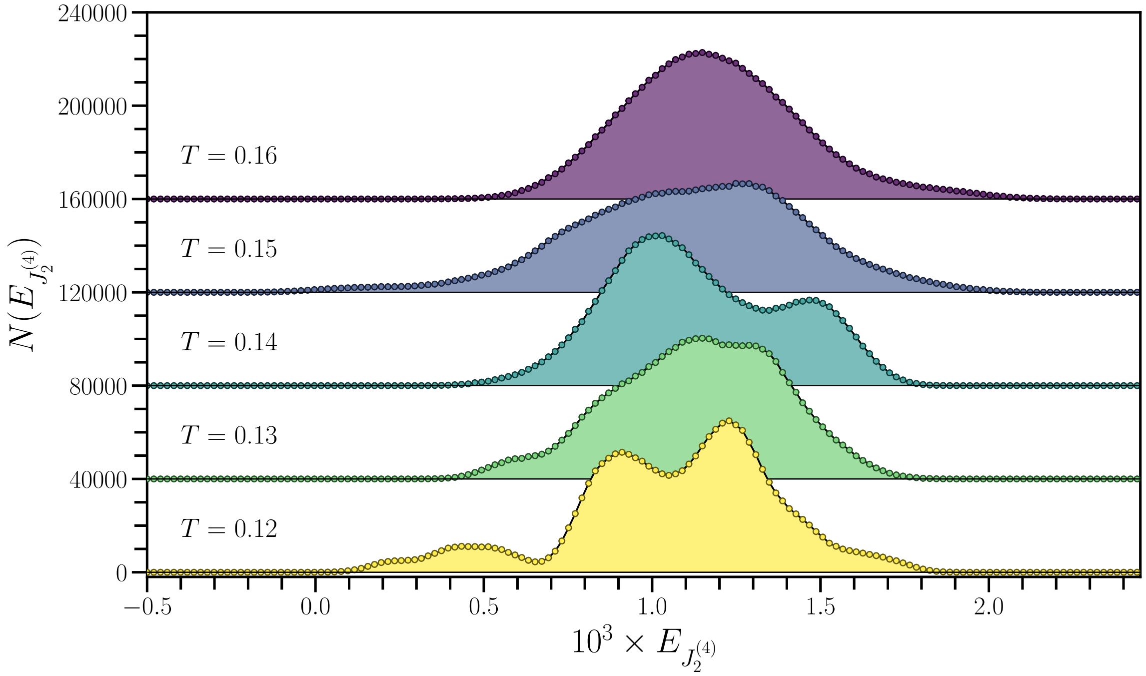

Figure 8.8: Evolution of the histograms of the energy components $E_2^{(4)}$ during the nucleation of the Ising phases. The energy components were collected from an equilibrated $L = 54$ system after each MC update (with the total of 2×10^6 MC updates per temperature).

that lie inside of this ring. Since the Ising fluctuations prevent the breaking of the time-reversal symmetry, this quasi-degeneracy leads to the entropic stabilization of the nematic phase by thermal fluctuations [8]. Eventually, the energetic penalties become sufficiently large and the structures nucleate into Ising-like patterns. However, this transition cannot happen in a continuous fashion, since any fluctuation would stabilize a nematic phase. Therefore, the nucleation occurs as a weak first-order transition. Although this discussion is only qualitative, in Ref. [81] we confirmed it by performing a field theory analysis of the effective model in eq. (7.24). This type of a fluctuation-induced first-order transition is known as the Brazovskii transition [157]. The original subject of Brazovskii's study was a 3D isotropic systems with a degenerate manifold of states located on a surface of a sphere in the reciprocal space. This mechanism for a first-order transition was demonstrated in a number of very distinct systems, from the theory of weak crystallization of solids to the formation of biological

---

[8] In other words, the chiral nematic phase acts as the Ising paramagnet.

membranes [158–162].

8.5 Summary of important results and open questions

In this final chapter, we presented a numerical MC study of the thermal properties of Ising-like phases. Our results reveal that the nucleation of the Ising-like patterns at finite temperatures displays a surprising complexity and occurs in three stages: a crossover to a chiral paramagnetic state, a KT transition to a chiral nematic phase, and an unusual first-order transition into the low-temperature Ising-like phase.

The crossover from the Heisenberg to the chiral XY paramagnetism is driven entirely by the DM interactions, since the remaining exchange couplings are isotropic. Interestingly, similar qualitative change from isotropic to the chiral paramagnetic state was reported in a chiral helimagnet MnSi, which is well-know for the experimental realization of magnetic skyrmions [163, 164]. Furthermore, the transition from the chiral paramagnet to the helimagnetic phase is also said to display the fluctuation-induced first-order behaviour, as prescribed by the Brazovskii scenario [165–167]. These surprising similarities might indicate universal properties of the Heisenberg-DM models that are valid in both centrosymmetric (*e.g.* AB-SKL) and non-centrosymmetric (*e.g.* MnSi) systems.

The most intriguing state revealed by our analysis is the chiral nematic phase. As stated in the main discussion, the existence of nematic phases in spin systems continues to be a subject of controversy. The quadrupolar order presented in this work is fundamentally different in that we demonstrate a nematic ordering of the LOPs, rather than individual spins. Since the Ising-like phases in the AB-SKL are robust against various perturbation, we propose that these systems could be promising candidates for experimental realization of these exotic phases. An important question that should be addressed in the future studies is whether these phases persist in 3D. A theoretical discovery of a long-range nematic order in a magnetic system could bring us a step closer to an experimental realization of these states in realistic magnetic compounds.

Finally, the transition from the chiral nematic phase to the low-temperature Ising-like state was shown to be of first-order with the use of energy histograms. Interestingly, these histograms revealed up to seven coexisting metastable configurations at once, suggesting a complex free energy landscape. It remains unclear if the final spin configuration obtained in the MC simulations is a true ground state with a large degeneracy, or if it is simply an arrested metastable configuration. This will be the subject of future investigations. The mechanism of the fluctuation-driven first-order transition discussed here and confirmed in Ref. [81] also deserves further investigation in 3D systems. We would expect the situation in bulk systems to be different, since the relative number of the quasi-degenerate wavevectors with respect to the total volume of the Brillouin zone would be smaller in 3D compared to 2D. It would therefore also be interesting to study these differences in thin-film systems with different numbers of layers.

Chapter 9

Summary and conclusions

> What you do in this world is a matter of no consequence. The question is what can you make people believe you have done.
>
> ---
>
> Arthur Conan Doyle,
> *A Study in Scarlet*

In the Introduction, we stated that the effects of 3D stacking of kagome layers remain relatively unknown. We motivated an investigation into the magnetic properties of AB-SKL by referring to a wealth of experimental data and potential importance of these compounds for industrial applications. In what followed, we quickly realized that this simple modification of the well-known 2D system leads to fascinatingly rich phenomena, some of which evaded our best attempts at characterizing them.

In our studies, we made use of various analytical and numerical methods. Symmetry analysis was first used to derive the magnetic Hamiltonian for AB-SKL systems and then to describe the emergent self-duality properties of the parameter space of the resulting model. The properties of the spin Hamiltonian were studied numerically using MC simulations to characterize the magnetic ground states in a large portion of the parameter space. MC methods were also used to study the finite-temperature properties of the unusual Ising-like phases. Finally, we developed an analytical coarse-graining method that allowed us firstly to obtain the exact effects of the in-plane anisotropy in Mn_3X compounds, and secondly to derive an effective model for the Ising-like phases, written in terms of the averaged local order parameter variables.

It would be a significant overstatement to say that this work provides, in any sense, a complete description of the properties of AB-SKL. After all, there are still many unanswered questions, some of which we pointed out at the end of each chapter. It is, nevertheless, important to summarize the most significant results of this thesis and potential avenues for the future studies.

Before summarizing the results in this thesis, let us briefly discuss the potential applications of the magnetic AB-SKL systems for high-speed spintronic devices. Even without an overall magnetization, the magnetic properties of antiferromagnetic metals can be utilized with the use of spin-polarized currents, since the principles of magnetic interactions between the localized free electron spins are exactly the same as in ferromagnets [6, 7, 168]. As a result, the spin-polarized currents may be used to switch the direction of the aniferromagnetic order, thus providing a way to write the information in antiferromagnetic devices. The rate of this switching depends on both the energetic cost of inducing a magnetic moment as well as the strength magnetic anisotropy [6]. One of the potential advantages of antiferromagnetic memory storage is that the switch rates of the antiferromagnets have been shown to be as large as two orders of magnitude higher than those of the ferromagnets [169]. When it comes to the antiferromagnetic AB-SKL compounds, such as the Mn_3X family, the anisotropically induced magnetic moment is of high utility, since it may interact with the spin-polarized free electrons and thus lower the energy barrier for the magnetic switching [76]. Therefore, the study of the in-plane anisotropy in Chapter 6 is relevant for the understanding of the six-fold switching in these systems. We also note that the large AHE, observed in $\mathrm{Mn}_3\mathrm{Sn}$ and $\mathrm{Mn}_3\mathrm{Ge}$ is connected to the non-trivial topology of the electronic band structure [46, 52, 55]. This topological character arises from the non-collinear magnetic structure and provides extremely robust exotic electronic properties, which can be manipulated by polarized currents [170]. Finally, we note that since many of the phases studied in this thesis, including the exotic $\mathbf{\Lambda}_4$ Ising-like phases, are chiral. Since spin chirality is known to couple to the electron currents to produce emergent electomagnetic fields [171, 172], it may be possible to utilize the spin structures in AB-SKL for manipulation or generation of spin-polarized currents.

9.1 Summary of important results

9.1.1 Derivation of the magnetic Hamiltonian

The first main achievement of this work is the derivation of the phenomenological spin Hamiltonian in Chapter 2, eq. (2.30) using symmetry principles. As stated in Ref. [75], this is the first general model, which was derived rigorously from symmetry, that provides all possible two-spin magnetic interactions in AB-SKL. Our analysis identified previously ignored interactions, such as the inter-layer DM couplings and anisotropic exchange interactions. This model served as the backbone for the characterization of all magnetic properties of AB-SKL in this thesis. The derivation was presented in a pedagogical way, which will hopefully be useful to anyone new to the symmetry analysis. At the same time, the supplemental material of Ref. [75] provides a group theory-based analysis, serving as an alternative reference for this derivation.

9.1.2 Self-duality transformations

Arguably the most important discovery that helped us to devise a very general characterization of different phenomena is the existence of self-duality transformations in Chapter 3. Self-duality was shown to describe the symmetries of the parameter space of the model through various local reference-frame transformations. We devised a procedure for identifying self-duality maps in our model and were able to relate the existence of certain transformations to the approximate strength of the SOC. Ref. [80] further extends this analysis and proposes a general procedure for deriving self-duality in arbitrary anisotropic magnetic systems. It is hard to overstate the importance and utility of self-duality. By using these transformations properly, one can make extremely general statements about the properties of the magnetic system, while significantly reducing the time of computation. One could also potentially relate the properties of models with non-physical parameters to ones with more realistic parameter sets, thus improving the chances of experimental discovery of various exotic phases.

Knowledge of possible self-dualities is important for experimental studies. Since certain quantities of interest may be exactly the same in distinct self-dual phases, in some cases a single experimental study may not be sufficient to conclusively determine the magnetic structure of the system [105]. Therefore, our results may be helpful for future experimental studies of magnetic properties of novel compounds with AB-SKL structure.

9.1.3 Ground state phase diagrams

In Chapter 5, we used numerical simulations to study general ground state properties of our model in the three SOC limits: isotropic, weakly-coupled and strongly-coupled. We discovered a large number of non-trivial magnetic structures, many of which are unique to the AB-SKL systems. Self-duality properties allowed us to separate these phases into families of self-dual configurations, which greatly simplified the overall analysis. These results should be of use for the future experimental characterization of magnetic phases in AB-SKL compounds and may serve as a good starting point for further in-depth theoretical studies.

9.1.4 In-plane anisotropy in Q=Γ phases

Chapter 6 concerned a question of in-plane anisotropy in $\mathbf{\Phi}_m^{(\mathbf{\Gamma})}$ structures, which is directly relevant to the experimental studies of Mn_3X compounds. We used an analytical procedure to derive the expression for the six-fold anisotropy from the SIA and anisotropic exchange interactions and showed that it removes the continuous rotational symmetry, in agreement with the experimental observations. Somewhat surprisingly, we found that while both SIA and anisotropic exchange lead to small twisting of spins towards the anisotropic axes, the direction of this twisting depends on the type of anisotropic interactions. This is relevant to the observed small magnetization in Mn_3X compounds, since the direction of the magnetic moment, induced by the anisotropy, depends on whether the SIA or the anisotropic exchange dominate in these systems. Ref. [75] takes this analysis a step further by providing numerical studies of the effects of other interactions in AB-SKL on the magnitude of the induced magnetic moment, as well as calculating the effects of the in-plane anisotropy on the static and dynamic structure factors for the elastic and inelastic neutron scattering experiments. These results could be used to determine the relative strengths of the different anisotropic interactions in Mn_3X compounds.

9.1.5 Ising-like phases

The last two chapters, 7 and 8 specialized on the properties of the most complex phases in our system – the Ising-like $\mathbf{\Lambda}_m$ structures. These studies are motivated by their considerable stability in the parameter space, which increases the possibility that these phases may be discovered in future experiments. Through analytical coarse-graining of the spin Hamiltonian in Chapter 7, we were able to derive an effective model for these structures, written in terms of the soft mode variables, corresponding to the in-plane rotations of the spins on the six sublattices in each unit cell. We parameterized these rotations using two-component local order parameter vectors, which resulted in the effective Hamiltonian in eq. (7.19). Upon further analysis, we found that the interactions in this coarse-grained model can be divided into couplings between dipolar and quadrupolar degrees of freedom. Since the quadrupolar interactions were the largest, we suggested that they are responsible for the Ising-like structure in these phases. This was confirmed in Chapter 8 by the numerical simulations of the AB-stacked kagome bilayers, which showed that the nucleation of the Ising-like structures occurs in three stages: a crossover from Heisenberg to XY paramagnet, a KT transition to a nematic phase, and finally a fluctuation-induced first-order transition to the low-temperature Ising-like phase.

These results provide a unique example of stabilization of nematic order in a magnetic system via DM interactions. Furthermore, in our analysis we considered the $\mathbf{\Lambda}_4$ phases, for which both the XY paramagnet and the nematic phase were shown to be chiral, which is highly unusual. Ref. [81] provides further analytical confirmation of the Brazovskii fluctuation-induced first-order transition at low temperatures, which indicates interesting connections between the properties of the Ising-like structures in AB-SKL and the magnetic phases in a chiral MnSi compound, where this transition has been discussed in the context of several experimental studies.

9.2 Future areas of study

This work provides, first of all, an invitation for other researchers to learn about and, hopefully, to extend the existing knowledge about the magnetism of AB-SKL.

The most natural extension of the results in most of the chapters in this work is the addition of the external magnetic field. The two most important studies that should be considered in the future are as follows. First of all, the generalization of the results in Chapter 6 to finite magnetic fields along arbitrary directions would provide a nice theoretical component to an experimental study of anisotropic interactions in AB-SKL, such as Mn_3X compounds. Secondly, analyzing the properties of the Ising-like structures under applied field would help to design potential experiments that would facilitate the discovery of these structures in real compounds.

Extending the symmetry analysis to finite systems, such as thin films is an interesting and important problem. The surface reduces the point group symmetry from D_{6h} to D_{3d}, which would introduce new spin invariants on each bond. Thus, the resulting surface interactions may lead to very different phenomena compared to the bulk, or further stabilize the exotic orders presented in this work. The symmetry analysis tools provided in Chapter 2 should be sufficient to derive these new interactions, and the bulk magnetic ground states in Chapter 5 would provide a starting point for the analysis of the surface magnetic properties.

Finally, we hope that our studies of the Ising-like phases would encourage further extensive experimental and theoretical investigations of these structures.

Beyond that, the author of this thesis made an attempt to introduce different tools – analytical, numerical, and data processing – that helped him to bring this work to life. It is his hope that the reader would find these tools useful and helpful in solving problems that may have nothing to do with the magnetic properties of AB-SKL.

Bibliography

[1] L. Néel, "Propriétés magnétiques de l'état métallique et énergie d'interaction entre atomes magnétiques," in *Annales de physique*, vol. 11, 5, pp. 232–279, 1936.

[2] L. Néel, "Magnetism and Local Molecular Field," *Science*, vol. 174, no. 4013, pp. 985–992, 1971.

[3] C. G. Shull and J. S. Smart, "Detection of Antiferromagnetism by Neutron Diffraction," *Phys. Rev.*, vol. 76, pp. 1256–1257, Oct 1949.

[4] V. K. Joshi, "Spintronics: A contemporary review of emerging electronics devices," *Engineering Science and Technology, an International Journal*, vol. 19, no. 3, pp. 1503–1513, 2016.

[5] B. Dieny, I. L. Prejbeanu, K. Garello, P. Gambardella, P. Freitas, R. Lehndorff, W. Raberg, U. Ebels, S. O. Demokritov, J. Akerman, A. Deac, P. Pirro, C. Adelmann, A. Anane, A. V. Chumak, A. Hirohata, S. Mangin, S. O. Valenzuela, M. C. Onbaşlı, M. d'Aquino, G. Prenat, G. Finocchio, L. Lopez-Diaz, R. Chantrell, O. Chubykalo-Fesenko, and P. Bortolotti, "Opportunities and challenges for spintronics in the microelectronics industry," *Nature Electronics*, vol. 3, pp. 446–459, 8 2020.

[6] T. Jungwirth, X. Marti, P. Wadley, and J. Wunderlich, "Antiferromagnetic spintronics," *Nature Nanotechnology*, vol. 11, pp. 231–241, 3 2016.

[7] T. Jungwirth, J. Sinova, A. Manchon, X. Marti, J. Wunderlich, and C. Felser, "The multiple directions of antiferromagnetic spintronics," *Nature Physics*, vol. 14, pp. 200–203, 3 2018.

[8] N. H. D. Bohr, "II. The Doctor's Dissertation (Text and Translation)**[See Introduction, sect. 2.]," in *EARLY WORK (1905–1911)* (L. Rosenfeld and J. R. Nielsen, eds.), vol. 1 of *Niels Bohr Collected Works*, pp. 163–393, Elsevier, 1972.

[9] Van Leeuwen, H.-J., "Problèmes de la théorie électronique du magnétisme," *J. Phys. Radium*, vol. 2, no. 12, pp. 361–377, 1921.

[10] W. Pauli, "Über den Zusammenhang des Abschlusses der Elektronengruppen im Atom mit der Komplexstruktur der Spektren," *Zeitschrift für Physik*, vol. 31, pp. 765–783, Feb 1925.

[11] W. Heisenberg, "Zur Theorie des Ferromagnetismus," *Zeitschrift für Physik*, vol. 49, pp. 619–636, Sep 1928.

[12] P. A. Dirac, *Chapter IX: Systems containing several similar particles.*, p. 221–224. Clarendon Pr., 3 ed., 1935.

[13] P. W. Anderson, “Antiferromagnetism. Theory of Superexchange Interaction,” *Phys. Rev.*, vol. 79, pp. 350–356, Jul 1950.

[14] M. Mourigal, W. T. Fuhrman, A. L. Chernyshev, and M. E. Zhitomirsky, “Dynamical structure factor of the triangular-lattice antiferromagnet,” *Phys. Rev. B*, vol. 88, p. 094407, Sep 2013.

[15] G. H. Wannier, “Antiferromagnetism. The Triangular Ising Net,” *Phys. Rev.*, vol. 79, pp. 357–364, Jul 1950.

[16] G. H. Wannier, “Antiferromagnetism. The Triangular Ising Net,” *Phys. Rev. B*, vol. 7, pp. 5017–5017, Jun 1973.

[17] K. Kanô and S. Naya, “Antiferromagnetism. The Kagomé Ising Net,” *Progress of Theoretical Physics*, vol. 10, pp. 158–172, 08 1953.

[18] J. T. Chalker, P. C. W. Holdsworth, and E. F. Shender, “Hidden order in a frustrated system: Properties of the Heisenberg Kagomé antiferromagnet,” *Phys. Rev. Lett.*, vol. 68, pp. 855–858, Feb 1992.

[19] A. B. Harris, C. Kallin, and A. J. Berlinsky, “Possible Néel orderings of the Kagomé antiferromagnet,” *Phys. Rev. B*, vol. 45, pp. 2899–2919, Feb 1992.

[20] D. A. Huse and A. D. Rutenberg, “Classical antiferromagnets on the Kagomé lattice,” *Phys. Rev. B*, vol. 45, pp. 7536–7539, Apr 1992.

[21] M. E. Zhitomirsky, “Octupolar ordering of classical kagome antiferromagnets in two and three dimensions,” *Phys. Rev. B*, vol. 78, p. 094423, Sep 2008.

[22] A. L. Chernyshev and M. E. Zhitomirsky, “Order and excitations in large $-S$ kagome-lattice antiferromagnets,” *Phys. Rev. B*, vol. 92, p. 144415, Oct 2015.

[23] P. Bruno, “Tight-binding approach to the orbital magnetic moment and magnetocrystalline anisotropy of transition-metal monolayers,” *Phys. Rev. B*, vol. 39, pp. 865–868, Jan 1989.

[24] I. Dzyaloshinsky, “A thermodynamic theory of “weak” ferromagnetism of antiferromagnetics,” *Journal of Physics and Chemistry of Solids*, vol. 4, no. 4, pp. 241–255, 1958.

[25] T. Moriya, “Anisotropic Superexchange Interaction and Weak Ferromagnetism,” *Phys. Rev.*, vol. 120, pp. 91–98, Oct 1960.

[26] A. Bogdanov and A. Hubert, “Thermodynamically stable magnetic vortex states in magnetic crystals,” *Journal of Magnetism and Magnetic Materials*, vol. 138, no. 3, pp. 255–269, 1994.

[27] U. K. Rößler, A. N. Bogdanov, and C. Pfleiderer, “Spontaneous skyrmion ground states in magnetic metals,” *Nature*, vol. 442, pp. 797–801, Aug 2006.

[28] L. Shekhtman, O. Entin-Wohlman, and A. Aharony, “Moriya’s anisotropic superexchange interaction, frustration, and Dzyaloshinsky’s weak ferromagnetism,” *Phys. Rev. Lett.*, vol. 69, pp. 836–839, Aug 1992.

[29] A. Zheludev, S. Maslov, I. Tsukada, I. Zaliznyak, L. P. Regnault, T. Masuda, K. Uchinokura, R. Erwin, and G. Shirane, “Experimental Evidence for Kaplan–Shekhtman–Entin-Wohlman–Aharony Interactions in $\mathrm{Ba_2CuGe_2}O_7$,” *Phys. Rev. Lett.*, vol. 81, pp. 5410–5413, Dec 1998.

[30] H. Takagi, T. Takayama, G. Jackeli, G. Khaliullin, and S. E. Nagler, “Concept and realization of Kitaev quantum spin liquids,” *Nature Reviews Physics*, vol. 1, pp. 264–280, Apr 2019.

[31] K. Essafi, O. Benton, and L. D. C. Jaubert, “A kagome map of spin liquids from XXZ to Dzyaloshinskii–Moriya ferromagnet,” *Nature Communications*, vol. 7, p. 10297, Jan 2016.

[32] K. Essafi, O. Benton, and L. D. C. Jaubert, “Generic nearest-neighbor kagome model: XYZ and Dzyaloshinskii-Moriya couplings with comparison to the pyrochlore-lattice case,” *Phys. Rev. B*, vol. 96, p. 205126, 11 2017.

[33] H. D. Rosales, F. A. G. Albarracín, P. Pujol, and L. D. C. Jaubert, “Skyrmion Fluid and Bimeron Glass Protected by a Chiral Spin Liquid on a Kagome Lattice,” *Phys. Rev. Lett.*, vol. 130, p. 106703, Mar 2023.

[34] K. Seki and K. Okunishi, “Phase Transitions for Cuboc Orders in Stacked Kagome Heisenberg Systems,” *Journal of the Physical Society of Japan*, vol. 87, no. 2, p. 023001, 2018.

[35] O. Götze and J. Richter, “The route to magnetic order in the spin-1/2 kagome Heisenberg antiferromagnet: The role of interlayer coupling,” *Europhysics Letters*, vol. 114, p. 67004, jul 2016.

[36] I. Tomeno, H. N. Fuke, H. Iwasaki, M. Sahashi, and Y. Tsunoda, “Magnetic neutron scattering study of ordered $\mathrm{Mn_3Ir}$,” *Journal of Applied Physics*, vol. 86, no. 7, pp. 3853–3856, 1999.

[37] K. O’Grady, L. Fernandez-Outon, and G. Vallejo-Fernandez, “A new paradigm for exchange bias in polycrystalline thin films,” *Journal of Magnetism and Magnetic Materials*, vol. 322, no. 8, pp. 883–899, 2010.

[38] H. Takahashi, M. Tsunoda, and M. Takahashi, “Perpendicular exchange anisotropy in Mn-Ir/Fe-Co/[Pt/Co] 4 multilayers,” *IEEE Transactions on Magnetics*, vol. 48, no. 11, pp. 4347–4350, 2012.

[39] V. Hemmati, M. L. Plumer, J. P. Whitehead, and B. W. Southern, “Monte Carlo simulations of magnetic ordering in the fcc kagome lattice,” *Phys. Rev. B*, vol. 86, p. 104419, Sep 2012.

[40] M. D. Leblanc, J. P. Whitehead, and M. L. Plumer, “Monte Carlo simulations of intragrain spin effects in a quasi-2D Heisenberg model with uniaxial anisotropy,” *Journal of Physics: Condensed Matter*, vol. 25, p. 196004, apr 2013.

[41] M. D. LeBlanc, M. L. Plumer, J. P. Whitehead, and B. W. Southern, “Monte Carlo simulations of the fcc kagome lattice: Competition between triangular frustration and cubic anisotropy,” *Phys. Rev. B*, vol. 88, p. 094406, Sep 2013.

[42] M. D. LeBlanc, B. W. Southern, M. L. Plumer, and J. P. Whitehead, “Spin waves in the anisotropic fcc kagome antiferromagnet,” *Phys. Rev. B*, vol. 90, p. 144403, Oct 2014.

[43] M. D. LeBlanc, A. A. Aczel, G. E. Granroth, B. W. Southern, J.-Q. Yan, S. E. Nagler, J. P. Whitehead, and M. L. Plumer, “Impact of further-range exchange and cubic anisotropy on magnetic excitations in the fcc kagome antiferromagnet $IrMn_3$,” *Phys. Rev. B*, vol. 104, p. 014427, Jul 2021.

[44] H. V. Yerzhakov, M. L. Plumer, and J. P. Whitehead, “Monte Carlo simulations of ABC stacked kagome lattice films,” *Journal of Physics: Condensed Matter*, vol. 28, p. 196003, apr 2016.

[45] R. Coehoorn, *Giant Magnetoresistance in Exchange-Biased Spin-Valve Layered Structures and its Application in Read Heads*, pp. 65–127. Berlin, Heidelberg: Springer Berlin Heidelberg, 2000.

[46] H. Chen, Q. Niu, and A. H. MacDonald, “Anomalous Hall Effect Arising from Noncollinear Antiferromagnetism,” *Phys. Rev. Lett.*, vol. 112, p. 017205, 1 2014.

[47] S. Nakatsuji, N. Kiyohara, and T. Higo, “Large anomalous Hall effect in a non-collinear antiferromagnet at room temperature,” *Nature*, vol. 527, pp. 212–215, 11 2015.

[48] A. K. Nayak, J. E. Fischer, Y. Sun, B. Yan, J. Karel, A. C. Komarek, C. Shekhar, N. Kumar, W. Schnelle, J. Kübler, C. Felser, and S. S. P. Parkin, “Large anomalous Hall effect driven by a nonvanishing Berry curvature in the noncolinear antiferromagnet Mn_3Ge,” *Science Advances*, vol. 2, no. 4, 2016.

[49] N. Kiyohara, T. Tomita, and S. Nakatsuji, “Giant Anomalous Hall Effect in the Chiral Antiferromagnet Mn_3Ge,” *Phys. Rev. Applied*, vol. 5, p. 064009, 6 2016.

[50] Y. Taguchi, Y. Oohara, H. Yoshizawa, N. Nagaosa, and Y. Tokura, “Spin Chirality, Berry Phase, and Anomalous Hall Effect in a Frustrated Ferromagnet,” *Science*, vol. 291, no. 5513, pp. 2573–2576, 2001.

[51] N. Nagaosa, J. Sinova, S. Onoda, A. H. MacDonald, and N. P. Ong, "Anomalous Hall effect," *Rev. Mod. Phys.*, vol. 82, pp. 1539–1592, 5 2010.

[52] J. Kübler and C. Felser, "Non-collinear antiferromagnets and the anomalous Hall effect," *EPL (Europhysics Letters)*, vol. 108, p. 67001, 12 2014.

[53] M.-T. Suzuki, T. Koretsune, M. Ochi, and R. Arita, "Cluster multipole theory for anomalous Hall effect in antiferromagnets," *Phys. Rev. B*, vol. 95, p. 094406, Mar 2017.

[54] O. Busch, B. Göbel, and I. Mertig, "Microscopic origin of the anomalous Hall effect in noncollinear kagome magnets," *Phys. Rev. Research*, vol. 2, p. 033112, 7 2020.

[55] L. Šmejkal, A. H. MacDonald, J. Sinova, S. Nakatsuji, and T. Jungwirth, "Anomalous Hall antiferromagnets," *Nature Reviews Materials*, vol. 7, pp. 482–496, Jun 2022.

[56] R. Troć, M. Pasturel, O. Tougait, A. P. Sazonov, A. Gukasov, C. Sułkowski, and H. Noël, "Single-crystal study of the kagome antiferromagnet $U_3Ru_4Al_{12}$," *Phys. Rev. B*, vol. 85, p. 064412, Feb 2012.

[57] D. I. Gorbunov, M. S. Henriques, A. V. Andreev, A. Gukasov, V. Petříček, N. V. Baranov, Y. Skourski, V. Eigner, M. Paukov, J. Prokleška, and A. P. Gonçalves, "Electronic properties of a distorted kagome lattice antiferromagnet $Dy_3Ru_4Al_{12}$," *Phys. Rev. B*, vol. 90, p. 094405, Sep 2014.

[58] S. Nakamura, S. Toyoshima, N. Kabeya, K. Katoh, T. Nojima, and A. Ochiai, "Low-temperature properties of the $S = \frac{1}{2}$ spin system $Yb_3Ru_4Al_{12}$ with a distorted kagome lattice structure," *Phys. Rev. B*, vol. 91, p. 214426, Jun 2015.

[59] D. I. Gorbunov, M. S. Henriques, A. V. Andreev, V. Eigner, A. Gukasov, X. Fabrèges, Y. Skourski, V. Petříček, and J. Wosnitza, "Magnetic anisotropy and reduced neodymium magnetic moments in $Nd_3Ru_4Al_{12}$," *Phys. Rev. B*, vol. 93, p. 024407, Jan 2016.

[60] V. Chandragiri, K. K. Iyer, and E. V. Sampathkumaran, "Magnetic behavior of $Gd_3Ru_4Al_12$, a layered compound with distorted kagomé net," *Journal of Physics: Condensed Matter*, vol. 28, p. 286002, may 2016.

[61] I. Ishii, T. Mizuno, K. Takezawa, S. Kumano, Y. Kawamoto, T. Suzuki, D. I. Gorbunov, M. S. Henriques, and A. V. Andreev, "Magnetic-field-induced quadrupolar ordering and the crystal electric field effect in the distorted kagome lattice antiferromagnet $Dy_3Ru_4Al_{12}$," *Phys. Rev. B*, vol. 97, p. 235130, Jun 2018.

[62] D. I. Gorbunov, T. Nomura, I. Ishii, M. S. Henriques, A. V. Andreev, M. Doerr, T. Stöter, T. Suzuki, S. Zherlitsyn, and J. Wosnitza, "Crystal-field effects in the kagome antiferromagnet $Ho_3Ru_4Al_{12}$," *Phys. Rev. B*, vol. 97, p. 184412, May 2018.

[63] T. Matsumura, Y. Ozono, S. Nakamura, N. Kabeya, and A. Ochiai, "Helical Ordering of Spin Trimers in a Distorted Kagome Lattice of $Gd_3Ru_4Al_{12}$ Studied by Resonant X-ray Diffraction," *Journal of the Physical Society of Japan*, vol. 88, no. 2, p. 023704, 2019.

[64] M. Hirschberger, T. Nakajima, S. Gao, L. Peng, A. Kikkawa, T. Kurumaji, M. Kriener, Y. Yamasaki, H. Sagayama, H. Nakao, K. Ohishi, K. Kakurai, Y. Taguchi, X. Yu, T.-h. Arima, and Y. Tokura, "Skyrmion phase and competing magnetic orders on a breathing kagomé lattice," *Nature Communications*, vol. 10, p. 5831, Dec 2019.

[65] L. A. Fenner, A. A. Dee, and A. S. Wills, "Non-collinearity and spin frustration in the itinerant kagome ferromagnet Fe_3Sn_2," *Journal of Physics: Condensed Matter*, vol. 21, p. 452202, oct 2009.

[66] Z. Hou, W. Ren, B. Ding, G. Xu, Y. Wang, B. Yang, Q. Zhang, Y. Zhang, E. Liu, F. Xu, W. Wang, G. Wu, X. Zhang, B. Shen, and Z. Zhang, "Observation of Various and Spontaneous Magnetic Skyrmionic Bubbles at Room Temperature in a Frustrated Kagome Magnet with Uniaxial Magnetic Anisotropy," *Advanced Materials*, vol. 29, no. 29, p. 1701144, 2017.

[67] J. Tang, L. Kong, Y. Wu, W. Wang, Y. Chen, Y. Wang, J. Li, Y. Soh, Y. Xiong, M. Tian, and H. Du, "Target Bubbles in Fe_3Sn_2 Nanodisks at Zero Magnetic Field," *ACS Nano*, vol. 14, no. 9, pp. 10986–10992, 2020. PMID: 32806036.

[68] M. Altthaler, E. Lysne, E. Roede, L. Prodan, V. Tsurkan, M. A. Kassem, H. Nakamura, S. Krohns, I. Kézsmárki, and D. Meier, "Magnetic and geometric control of spin textures in the itinerant kagome magnet Fe_3Sn_2," *Phys. Rev. Res.*, vol. 3, p. 043191, Dec 2021.

[69] L. Kong, J. Tang, W. Wang, Y. Wu, J. Jiang, Y. Wang, J. Li, Y. Xiong, M. Tian, and H. Du, "Observation of hybrid magnetic skyrmion bubbles in Fe_3Sn_2 nanodisks," *Phys. Rev. B*, vol. 107, p. 174425, May 2023.

[70] D. Flavián, J. Nagl, S. Hayashida, M. Yan, O. Zaharko, T. Fennell, D. Khalyavin, Z. Yan, S. Gvasaliya, and A. Zheludev, "Magnetic phase diagram of the breathing-kagome antiferromagnet Nd_3BWO_9," *Phys. Rev. B*, vol. 107, p. 174406, May 2023.

[71] J. Liu and L. Balents, "Anomalous Hall Effect and Topological Defects in Antiferromagnetic Weyl Semimetals: Mn_3Sn/Ge," *Phys. Rev. Lett.*, vol. 119, p. 087202, 8 2017.

[72] P. Park, J. Oh, K. Uhlířová, J. Jackson, A. Deák, L. Szunyogh, K. H. Lee, H. Cho, H.-L. Kim, H. C. Walker, D. Adroja, V. Sechovský, and J.-G. Park, "Magnetic excitations in non-collinear antiferromagnetic Weyl semimetal Mn_3Sn," *npj Quantum Materials*, vol. 3, p. 63, 12 2018.

[73] J.-R. Soh, F. de Juan, N. Qureshi, H. Jacobsen, H.-Y. Wang, Y.-F. Guo, and A. T. Boothroyd, “Ground-state magnetic structure of $\mathrm{Mn_3Ge}$,” *Phys. Rev. B*, vol. 101, p. 140411, 4 2020.

[74] S. Dasgupta and O. Tchernyshyov, “Theory of spin waves in a hexagonal antiferromagnet,” *Phys. Rev. B*, vol. 102, p. 144417, 10 2020.

[75] A. Zelenskiy, T. L. Monchesky, M. L. Plumer, and B. W. Southern, “Anisotropic magnetic interactions in hexagonal *AB*-stacked kagome lattice structures: Application to $\mathrm{Mn_3}X$ ($X = \mathrm{Ge, Sn, Ga}$) compounds,” *Phys. Rev. B*, vol. 103, p. 144401, Apr 2021.

[76] H. Reichlova, T. Janda, J. Godinho, A. Markou, D. Kriegner, R. Schlitz, J. Zelezny, Z. Soban, M. Bejarano, H. Schultheiss, P. Nemec, T. Jungwirth, C. Felser, J. Wunderlich, and S. T. B. Goennenwein, “Imaging and writing magnetic domains in the non-collinear antiferromagnet $\mathrm{Mn_3Sn}$,” *Nature Communications*, vol. 10, p. 5459, 11 2019.

[77] X. Li, C. Collignon, L. Xu, H. Zuo, A. Cavanna, U. Gennser, D. Mailly, B. Fauqué, L. Balents, Z. Zhu, and K. Behnia, “Chiral domain walls of $\mathrm{Mn_3Sn}$ and their memory,” *Nature Communications*, vol. 10, p. 3021, 7 2019.

[78] D. Go, M. Sallermann, F. R. Lux, S. Blügel, O. Gomonay, and Y. Mokrousov, “Noncollinear Spin Current for Switching of Chiral Magnetic Textures,” *Phys. Rev. Lett.*, vol. 129, p. 097204, Aug 2022.

[79] X. Zhou, X. Chen, Y. You, L. Liao, H. Bai, R. Zhang, Y. Zhou, H. Wu, C. Song, and F. Pan, “Exchange Bias in Antiferromagnetic $\mathrm{Mn_3Sn}$ Monolayer Films,” *Phys. Rev. Appl.*, vol. 14, p. 054037, Nov 2020.

[80] A. Zelenskiy, T. L. Monchesky, M. L. Plumer, and B. W. Southern, “Magnetic interactions in AB-stacked kagome lattices: Magnetic structure, symmetry, and duality,” *Phys. Rev. B*, vol. 106, p. 144433, Oct 2022.

[81] A. Zelenskiy, M. L. Plumer, B. W. Southern, M. E. Zhitomirsky, and T. L. Monchesky, “Chiral nematic and fluctuation-induced first-order phase transitions in AB-stacked kagome bilayers,” 2023.

[82] M. Tinkham, *Chapter 3: Theory of Group Representations*, p. 20–31. Dover Publications, 2003.

[83] E. Bertaut, “4 - Spin Configurations of Ionic Structures: Theory and Practice,” in *Spin Arrangements and Crystal Structure, Domains, and Micromagnetics* (G. T. Rado and H. Suhl, eds.), pp. 149 – 209, Academic Press, 1963.

[84] S. H. Curnoe, “Effective spin-1/2 exchange model for $\mathrm{Tb_2Ti_2O_7}$,” *Phys. Rev. B*, vol. 88, p. 014429, Jul 2013.

[85] K. P. W. Hall and S. H. Curnoe, “Generalized model of MnSi-like spiral magnets,” *Phys. Rev. B*, vol. 104, p. 094408, Sep 2021.

[86] C. Kittel, “Model of Exchange-Inversion Magnetization,” *Phys. Rev.*, vol. 120, pp. 335–342, Oct 1960.

[87] J. C. Slonczewski, “Origin of biquadratic exchange in magnetic multilayers (invited),” *Journal of Applied Physics*, vol. 73, no. 10, pp. 5957–5962, 1993.

[88] S. Hayami, “Multiple-Q magnetism by anisotropic bilinear-biquadratic interactions in momentum space,” *Journal of Magnetism and Magnetic Materials*, vol. 513, p. 167181, Nov 2020.

[89] T. Hahn, U. Shmueli, and J. W. Arthur, *International tables for crystallography*, vol. 1. Reidel Dordrecht, 1983.

[90] J. W. Cable, N. Wakabayashi, and P. Radhakrishna, “Magnetic excitations in the triangular antiferromagnets Mn_3Sn and Mn_3Ge,” *Phys. Rev. B*, vol. 48, pp. 6159–6166, 9 1993.

[91] A. S. Sukhanov, M. S. Pavlovskii, P. Bourges, H. C. Walker, K. Manna, C. Felser, and D. S. Inosov, “Magnon-polaron excitations in the noncollinear antiferromagnet Mn_3Ge,” *Phys. Rev. B*, vol. 99, p. 214445, 6 2019.

[92] Y. Chen, J. Gaudet, S. Dasgupta, G. G. Marcus, J. Lin, T. Chen, T. Tomita, M. Ikhlas, Y. Zhao, W. C. Chen, M. B. Stone, O. Tchernyshyov, S. Nakatsuji, and C. Broholm, “Antichiral spin order, its soft modes, and their hybridization with phonons in the topological semimetal Mn_3Ge,” *Phys. Rev. B*, vol. 102, p. 054403, 8 2020.

[93] H. A. Kramers and G. H. Wannier, “Statistics of the Two-Dimensional Ferromagnet. Part I,” *Phys. Rev.*, vol. 60, pp. 252–262, Aug 1941.

[94] L. Onsager, “Crystal Statistics. I. A Two-Dimensional Model with an Order-Disorder Transition,” *Phys. Rev.*, vol. 65, pp. 117–149, Feb 1944.

[95] G. H. Wannier, “The Statistical Problem in Cooperative Phenomena,” *Rev. Mod. Phys.*, vol. 17, pp. 50–60, Jan 1945.

[96] F. J. Wegner, “Duality in Generalized Ising Models and Phase Transitions without Local Order Parameters,” *Journal of Mathematical Physics*, vol. 12, no. 10, pp. 2259–2272, 1971.

[97] F. Y. Wu and Y. K. Wang, “Duality transformation in a many-component spin model,” *Journal of Mathematical Physics*, vol. 17, no. 3, pp. 439–440, 1976.

[98] R. Savit, “Duality in field theory and statistical systems,” *Rev. Mod. Phys.*, vol. 52, pp. 453–487, Apr 1980.

[99] J. D. Jackson, *Classical Electrodynamics.* New York, NY: Wiley, 2nd ed. ed., 1998.

[100] J. c. v. Chaloupka and G. Khaliullin, "Hidden symmetries of the extended Kitaev-Heisenberg model: Implications for the honeycomb-lattice iridates $A_2\mathrm{IrO}_3$," *Phys. Rev. B*, vol. 92, p. 024413, Jul 2015.

[101] I. Kimchi and A. Vishwanath, "Kitaev-Heisenberg models for iridates on the triangular, hyperkagome, kagome, fcc, and pyrochlore lattices," *Phys. Rev. B*, vol. 89, p. 014414, Jan 2014.

[102] P. A. Maksimov, Z. Zhu, S. R. White, and A. L. Chernyshev, "Anisotropic-Exchange Magnets on a Triangular Lattice: Spin Waves, Accidental Degeneracies, and Dual Spin Liquids," *Phys. Rev. X*, vol. 9, p. 021017, Apr 2019.

[103] T. Giamarchi, *Quantum physics in one dimension oxford science publications.* Oxford University Press: New York, USA, 2004.

[104] S. K. Kim and J. Zang, "U(1) symmetry of the spin-orbit coupled Hubbard model on the kagome lattice," *Phys. Rev. B*, vol. 92, p. 205106, Nov 2015.

[105] A. L. Sanders, R. A. Mole, J. Liu, A. J. Brown, D. Yu, C. D. Ling, and S. Rachel, "Dominant Kitaev interactions in the honeycomb materials $\mathrm{Na_3Co_2SbO_6}$ and $\mathrm{Na_2Co_2TeO_6}$," *Phys. Rev. B*, vol. 106, p. 014413, Jul 2022.

[106] M. Newman and G. Barkema, *Monte carlo methods in statistical physics*, vol. 24. Oxford University Press: New York, USA, 1999.

[107] D. P. Landau and K. Binder, *A guide to Monte Carlo simulations in statistical physics.* Cambridge university press, 2014.

[108] J. D. Alzate-Cardona, D. Sabogal-Suárez, R. F. L. Evans, and E. Restrepo-Parra, "Optimal phase space sampling for Monte Carlo simulations of Heisenberg spin systems," *Journal of Physics: Condensed Matter*, vol. 31, p. 095802, jan 2019.

[109] Y. Miyatake, M. Yamamoto, J. Kim, M. Toyonaga, and O. Nagai, "On the implementation of the'heat bath'algorithms for Monte Carlo simulations of classical Heisenberg spin systems," *Journal of Physics C: solid state physics*, vol. 19, no. 14, p. 2539, 1986.

[110] M. Creutz, "Overrelaxation and Monte Carlo simulation," *Phys. Rev. D*, vol. 36, pp. 515–519, Jul 1987.

[111] K. Kanki, D. Loison, and K. D. Schotte, "Efficiency of the microcanonical overrelaxation algorithm for vector spins analyzing first and second order transitions," *The European Physical Journal B - Condensed Matter and Complex Systems*, vol. 44, pp. 309–315, Apr 2005.

[112] T. Okubo, S. Chung, and H. Kawamura, “Multiple-q States and the Skyrmion Lattice of the Triangular-Lattice Heisenberg Antiferromagnet under Magnetic Fields,” *Phys. Rev. Lett.*, vol. 108, p. 017206, Jan 2012.

[113] L. Janssen, E. C. Andrade, and M. Vojta, “Honeycomb-Lattice Heisenberg-Kitaev Model in a Magnetic Field: Spin Canting, Metamagnetism, and Vortex Crystals,” *Phys. Rev. Lett.*, vol. 117, p. 277202, Dec 2016.

[114] J. H. Han, *Solitons and Homotopy*, pp. 19–43. Cham: Springer International Publishing, 2017.

[115] J. Villain, R. Bidaux, J.-P. Carton, and R. Conte, “Order as an effect of disorder,” *Journal de Physique*, vol. 41, no. 11, pp. 1263–1272, 1980.

[116] C. L. Henley, “Ordering due to disorder in a frustrated vector antiferromagnet,” *Phys. Rev. Lett.*, vol. 62, pp. 2056–2059, Apr 1989.

[117] J. S. Gardner, M. J. P. Gingras, and J. E. Greedan, “Magnetic pyrochlore oxides,” *Rev. Mod. Phys.*, vol. 82, pp. 53–107, Jan 2010.

[118] T. Nagamiya, S. Tomiyoshi, and Y. Yamaguchi, “Triangular spin configuration and weak ferromagnetism of Mn_3Sn and Mn_3Ge,” *Solid State Communications*, vol. 42, no. 5, pp. 385 – 388, 1982.

[119] T. F. Duan, W. J. Ren, W. L. Liu, S. J. Li, W. Liu, and Z. D. Zhang, “Magnetic anisotropy of single-crystalline Mn_3Sn in triangular and helix-phase states,” *Applied Physics Letters*, vol. 107, no. 8, p. 082403, 2015.

[120] H. Ohmori, S. Tomiyoshi, H. Yamauchi, and H. Yamamoto, “Spin structure and weak ferromagnetism of Mn_3Sn,” *Journal of Magnetism and Magnetic Materials*, vol. 70, no. 1, pp. 249–251, 1987.

[121] J. Kouvel and J. Kasper, “Magnetic structure of Mn_3Sn,” in *Proceedings of the International Conference on Magnetism*, Institute of Physics and Physical Chemistry, London, 1965.

[122] G. Kádár and E. Krén, “Neutron diffraction study of Mn_3Ge,” *Int. J. Magn*, vol. 1, pp. 143–148, 1971.

[123] E. Krén and G. Kádár, “Neutron diffraction study of Mn_3Ga,” *Solid State Communications*, vol. 8, no. 20, pp. 1653 – 1655, 1970.

[124] G. J. Zimmer, E. Kren, C. D. Graham, and J. J. Rhyne, “Investigation of the Magnetic Phase Transformation in Mn_3Sn,” *AIP Conference Proceedings*, vol. 5, no. 1, pp. 513–516, 1972.

[125] P. Radhakrishna and S. Tomiyoshi, “A neutron scattering study of the magnetic excitations in a triangular itinerant antiferromagnet, Mn_3Sn,” *Journal of Physics: Condensed Matter*, vol. 3, pp. 2523–2527, 4 1991.

[126] K. Yasukōchi, K. Kanematsu, and T. Ohoyama, “Magnetic Properties of Intermetallic Compounds in Manganese-Tin System: $Mn_{3.67}Sn$, $Mn_{1.77}Sn$, and $MnSn_2$,” *Journal of the Physical Society of Japan*, vol. 16, no. 6, pp. 1123–1130, 1961.

[127] T. Ohoyama, K. Yasukōchi, and K. Kanematsu, “A New Phase of an Intermetallic Compound $Mn_{3.4}Sn$ and its Magnetism,” *Journal of the Physical Society of Japan*, vol. 16, no. 2, pp. 352–353, 1961.

[128] P. de Gennes and J. Prost, *The Physics of Liquid Crystals.* International Series of Monographs on Physics, Clarendon Press, 1993.

[129] D. L. Stein, “Kosterlitz-Thouless phase transitions in two-dimensional liquid crystals,” *Phys. Rev. B*, vol. 18, pp. 2397–2399, Sep 1978.

[130] J. M. Luttinger and L. Tisza, “Theory of Dipole Interaction in Crystals,” *Phys. Rev.*, vol. 70, pp. 954–964, Dec 1946.

[131] D. H. Lyons and T. A. Kaplan, “Method for Determining Ground-State Spin Configurations,” *Phys. Rev.*, vol. 120, pp. 1580–1585, Dec 1960.

[132] D. B. Litvin, “The Luttinger-Tisza method,” *Physica*, vol. 77, pp. 205–219, Oct 1974.

[133] A. J. Berlinsky and A. B. Harris, *Density Matrix Mean-Field Theory and Landau Expansions*, pp. 201–222. Cham: Springer International Publishing, 2019.

[134] D. H. Lee and G. Grinstein, “Strings in two-dimensional classical XY models,” *Phys. Rev. Lett.*, vol. 55, pp. 541–544, Jul 1985.

[135] S. E. Korshunov, “Possible splitting of a phase transition in a 2D XY model,” *JETP Lett. (Engl. Transl.); (United States)*, vol. 41:5, 3 1985.

[136] S. E. Korshunov, “Phase diagram of the modified XY model,” *Journal of Physics C: Solid State Physics*, vol. 19, p. 4427, aug 1986.

[137] E. Granato, J. M. Kosterlitz, J. Lee, and M. P. Nightingale, “Phase transitions in coupled XY-Ising systems,” *Phys. Rev. Lett.*, vol. 66, pp. 1090–1093, Feb 1991.

[138] D. B. Carpenter and J. T. Chalker, “The phase diagram of a generalised XY model,” *Journal of Physics: Condensed Matter*, vol. 1, p. 4907, jul 1989.

[139] F. C. Poderoso, J. J. Arenzon, and Y. Levin, “New Ordered Phases in a Class of Generalized XY Models,” *Phys. Rev. Lett.*, vol. 106, p. 067202, Feb 2011.

[140] Y. Shi, A. Lamacraft, and P. Fendley, “Boson Pairing and Unusual Criticality in a Generalized XY Model,” *Phys. Rev. Lett.*, vol. 107, p. 240601, Dec 2011.

[141] G. A. Canova, Y. Levin, and J. J. Arenzon, "Kosterlitz-Thouless and Potts transitions in a generalized XY model," *Phys. Rev. E*, vol. 89, p. 012126, Jan 2014.

[142] G. A. Canova, Y. Levin, and J. J. Arenzon, "Competing nematic interactions in a generalized XY model in two and three dimensions," *Phys. Rev. E*, vol. 94, p. 032140, Sep 2016.

[143] P. Serna, J. T. Chalker, and P. Fendley, "Deconfinement transitions in a generalised XY model," *Journal of Physics A: Mathematical and Theoretical*, vol. 50, p. 424003, sep 2017.

[144] M. Žukovič, "Multiple phase transitions in the XY model with nematic-like couplings," *Physics Letters A*, vol. 382, no. 37, pp. 2618–2621, 2018.

[145] M. Zelli, K. Boese, and B. W. Southern, "Short-time dynamics study of Heisenberg noncollinear magnets," *Phys. Rev. B*, vol. 76, p. 224407, Dec 2007.

[146] H. T. Diep, *Frustrated Spin Systems.* WORLD SCIENTIFIC, 2005.

[147] V. T. Ngo and H. T. Diep, "Phase transition in Heisenberg stacked triangular antiferromagnets: End of a controversy," *Phys. Rev. E*, vol. 78, p. 031119, Sep 2008.

[148] J. Villain, "Two-level systems in a spin-glass model. I. General formalism and two-dimensional model," *Journal of Physics C: Solid State Physics*, vol. 10, p. 4793, dec 1977.

[149] H. Kawamura, "Spin- and chirality-orderings of frustrated magnets – stacked-triangular anti-ferromagnets and spin glasses," *Canadian Journal of Physics*, vol. 79, no. 11-12, pp. 1447–1458, 2001.

[150] M. Blume and Y. Y. Hsieh, "Biquadratic Exchange and Quadrupolar Ordering," *Journal of Applied Physics*, vol. 40, pp. 1249–1249, 11 2003.

[151] N. Shannon, T. Momoi, and P. Sindzingre, "Nematic Order in Square Lattice Frustrated Ferromagnets," *Phys. Rev. Lett.*, vol. 96, p. 027213, Jan 2006.

[152] K. Penc and A. M. Läuchli, "Spin nematic phases in quantum spin systems," in *Introduction to frustrated magnetism: materials, experiments, theory*, pp. 331–362, Springer, 2010.

[153] N. Shannon, K. Penc, and Y. Motome, "Nematic, vector-multipole, and plateau-liquid states in the classical $O(3)$ pyrochlore antiferromagnet with biquadratic interactions in applied magnetic field," *Phys. Rev. B*, vol. 81, p. 184409, May 2010.

[154] T. Momoi, P. Sindzingre, and K. Kubo, “Spin Nematic Order in Multiple-Spin Exchange Models on the Triangular Lattice,” *Phys. Rev. Lett.*, vol. 108, p. 057206, Feb 2012.

[155] Y. Iqbal, P. Ghosh, R. Narayanan, B. Kumar, J. Reuther, and R. Thomale, “Intertwined nematic orders in a frustrated ferromagnet,” *Phys. Rev. B*, vol. 94, p. 224403, Dec 2016.

[156] S. Jiang, J. Romhányi, S. R. White, M. E. Zhitomirsky, and A. L. Chernyshev, “Where is the Quantum Spin Nematic?,” *Phys. Rev. Lett.*, vol. 130, p. 116701, Mar 2023.

[157] S. A. Brazovskiĭ, “Phase transition of an isotropic system to a nonuniform state,” *Soviet Journal of Experimental and Theoretical Physics*, vol. 41, p. 85, 1 1975.

[158] S. Brazovskiĭ and S. Dmitriev, “Phase transitions in cholesteric liquid crystals,” *Soviet Journal of Experimental and Theoretical Physics*, vol. 42, p. 497, 1975.

[159] S. A. Brazovskii, I. E. Dzyaloshinskii, and A. R. Muratov, “Theory of weak crystallization,” *Sov. Phys. JETP*, vol. 66, no. 3, p. 625, 1987.

[160] F. S. Bates, J. H. Rosedale, G. H. Fredrickson, and C. J. Glinka, “Fluctuation-Induced First-Order Transition of an Isotropic System to a Periodic State,” *Phys. Rev. Lett.*, vol. 61, pp. 2229–2232, Nov 1988.

[161] E. I. Kats, V. V. Lebedev, and A. R. Muratov, “Weak crystallization theory,” *Physics Reports*, vol. 228, pp. 1–91, 6 1993.

[162] M. O. Lavrentovich, E. M. Horsley, A. Radja, A. M. Sweeney, and R. D. Kamien, “First-order patterning transitions on a sphere as a route to cell morphology,” *Proceedings of the National Academy of Sciences*, vol. 113, no. 19, pp. 5189–5194, 2016.

[163] C. Pappas, E. Lelièvre-Berna, P. Falus, P. M. Bentley, E. Moskvin, S. Grigoriev, P. Fouquet, and B. Farago, “Chiral Paramagnetic Skyrmion-like Phase in MnSi,” *Phys. Rev. Lett.*, vol. 102, p. 197202, May 2009.

[164] S. Mühlbauer, B. Binz, F. Jonietz, C. Pfleiderer, R. A., N. A., G. R., and B. P., “Skyrmion Lattice in a Chiral Magnet,” *Science*, vol. 323, no. 5916, pp. 915–919, 2009.

[165] M. Janoschek, M. Garst, A. Bauer, P. Krautscheid, R. Georgii, P. Böni, and C. Pfleiderer, “Fluctuation-induced first-order phase transition in Dzyaloshinskii-Moriya helimagnets,” *Phys. Rev. B*, vol. 87, p. 134407, Apr 2013.

[166] A. Bauer, M. Garst, and C. Pfleiderer, “Specific Heat of the Skyrmion Lattice Phase and Field-Induced Tricritical Point in MnSi,” *Phys. Rev. Lett.*, vol. 110, p. 177207, Apr 2013.

[167] J. Kindervater, I. Stasinopoulos, A. Bauer, F. X. Haslbeck, F. Rucker, A. Chacon, S. Mühlbauer, C. Franz, M. Garst, D. Grundler, and C. Pfleiderer, "Weak Crystallization of Fluctuating Skyrmion Textures in MnSi," *Phys. Rev. X*, vol. 9, p. 041059, Dec 2019.

[168] E. V. Gomonay and V. M. Loktev, "Spintronics of antiferromagnetic systems (Review Article)," *Low Temperature Physics*, vol. 40, pp. 17–35, 01 2014.

[169] S. A. Siddiqui, J. Sklenar, K. Kang, M. J. Gilbert, A. Schleife, N. Mason, and A. Hoffmann, "Metallic antiferromagnets," *Journal of Applied Physics*, vol. 128, p. 040904, 07 2020.

[170] H. Tsai, T. Higo, K. Kondou, T. Nomoto, A. Sakai, A. Kobayashi, T. Nakano, K. Yakushiji, R. Arita, S. Miwa, Y. Otani, and S. Nakatsuji, "Electrical manipulation of a topological antiferromagnetic state," *Nature*, vol. 580, pp. 608–613, Apr 2020.

[171] T. Schulz, R. Ritz, A. Bauer, M. Halder, M. Wagner, C. Franz, C. Pfleiderer, K. Everschor, M. Garst, and A. Rosch, "Emergent electrodynamics of skyrmions in a chiral magnet," *Nature Physics*, vol. 8, pp. 301–304, Apr 2012.

[172] K. Everschor-Sitte and M. Sitte, "Real-space Berry phases: Skyrmion soccer (invited)," *Journal of Applied Physics*, vol. 115, no. 17, p. 172602, 2014.

[173] G. Jaeger, "The Ehrenfest Classification of Phase Transitions: Introduction and Evolution," *Archive for History of Exact Sciences*, vol. 53, pp. 51–81, May 1998.

[174] M. Plischke and B. Bergersen, *Equilibrium statistical physics.* World scientific, 1994.

[175] J. P. Sethna, *Statistical mechanics: entropy, order parameters, and complexity*, vol. 14. Oxford University Press, USA, 2021.

[176] A. Berlinsky and A. Harris, *Statistical Mechanics: An Introductory Graduate Course.* Springer Nature, 2019.

[177] E. Ising, "Beitrag zur Theorie des Ferromagnetismus," *Zeitschrift für Physik*, vol. 31, pp. 253–258, Feb 1925.

[178] R. Peierls, "On Ising's model of ferromagnetism," *Mathematical Proceedings of the Cambridge Philosophical Society*, vol. 32, no. 3, p. 477–481, 1936.

[179] N. D. Mermin and H. Wagner, "Absence of Ferromagnetism or Antiferromagnetism in One- or Two-Dimensional Isotropic Heisenberg Models," *Phys. Rev. Lett.*, vol. 17, pp. 1133–1136, Nov 1966.

[180] J. M. Kosterlitz and D. J. Thouless, “Ordering, metastability and phase transitions in two-dimensional systems,” *Journal of Physics C: Solid State Physics*, vol. 6, p. 1181, apr 1973.

[181] J. M. Kosterlitz, “The critical properties of the two-dimensional XY model,” *Journal of Physics C: Solid State Physics*, vol. 7, p. 1046, mar 1974.

Appendix A

Transformation properties of cross products

We are going to prove that

$$\mathbf{a} \cdot \big((\mathbf{R}\mathbf{b}) \times (\mathbf{R}\mathbf{c})\big) = \det(\mathbf{R})(\mathbf{R}^T\mathbf{a}) \cdot (\mathbf{b} \times \mathbf{c}), \tag{A.1}$$

where **a**, **b**, and **c** are vectors, and **R** is an orthogonal transformation matrix. This equation can be used to define the transformation properties of axial vectors (see Sec. 2.3) and to demonstrate the rotational symmetry of DM interactions in AB-SKL (Sec. 2.5). Although these properties are often quoted in the literature, the actual proof is almost always omitted and, as a result, is difficult to find in the literature.

First, the left side of eq. (A.1) can be written in index notation as

$$\sum_{\alpha\beta\gamma}\sum_{\zeta\eta} \varepsilon_{\alpha\beta\gamma} a_\alpha R_{\beta\zeta} b_\zeta R_{\gamma\eta} c_\eta, \tag{A.2}$$

where we use Greek letters for matrix components, and $\varepsilon_{\alpha\beta\gamma}$ is the Levi-Civita tensor. Note that the Levi-Civita tensor is also used in the definition of the determinant of a matrix:

$$\det(\mathbf{R}) = \sum_{\delta\beta\gamma} \varepsilon_{\delta\beta\gamma} R_{\delta 1} R_{\beta 2} R_{\gamma 3}. \tag{A.3}$$

Let us define a new tensor

$$T_{\mu\zeta\eta} = \sum_{\delta\beta\gamma} \varepsilon_{\delta\beta\gamma} R_{\delta\mu} R_{\beta\zeta} R_{\gamma\eta}. \tag{A.4}$$

Tensor $T_{\mu\zeta\eta}$ is completely antisymmetric with respect to permutations of the indices and therefore must be proportional to the Levi-Civita symbol, $T_{\mu\zeta\eta} = C\varepsilon_{\mu\zeta\eta}$. But from eq. (A.3) it follows that

$$T_{123} = C\varepsilon_{123} = C = \det(\mathbf{R}), \tag{A.5}$$

so $T_{\mu\zeta\eta} = \det(\mathbf{R})\varepsilon_{\mu\zeta\eta}$. Multiplying this equation by $R_{\alpha\mu}$ and summing over μ gives

$$\begin{aligned} \det\{R\} \sum_{\mu} \varepsilon_{\mu\zeta\eta} R_{\alpha\mu} &= \sum_{\delta\beta\gamma\mu} \varepsilon_{\delta\beta\gamma} R_{\delta\mu} R_{\beta\zeta} R_{\gamma\eta} R_{\alpha\mu} \\ &= \sum_{\beta\gamma} \varepsilon_{\alpha\beta\gamma} R_{\beta\eta} R_{\gamma\mu}, \end{aligned} \tag{A.6}$$

where in the last step we used the orthogonality property of R:

$$\mathbb{I} = \mathbf{R}^T\mathbf{R} = \sum_{\mu} R_{\delta\mu} R_{\alpha\mu} = \delta_{\delta\alpha}. \tag{A.7}$$

Returning to eq. (A.2), we see that

$$\sum_{\alpha\beta\gamma} \sum_{\zeta\eta} \varepsilon_{\alpha\beta\gamma} a_\alpha R_{\beta\zeta} b_\zeta R_{\gamma\eta} c_\eta = \det(\mathbf{R}) \sum_{\alpha\zeta\eta\mu} \varepsilon_{\mu\zeta\eta} R_{\alpha\mu} a_\alpha b_\zeta c_\eta, \tag{A.8}$$

or, in vector form

$$\det(\mathbf{R})\mathbf{a} \cdot \big[\mathbf{R}(\mathbf{b} \times \mathbf{c})\big] = \det(\mathbf{R})(\mathbf{R}^T\mathbf{a}) \cdot (\mathbf{b} \times \mathbf{c}), \tag{A.9}$$

as required.

Appendix B

Monte Carlo algorithms

Algorithm 1: Metropolis MC step

```
input : array of $N$ spin vectors, $\mathbf{S}$; array of effective field vectors, $\mathbf{H}$; inverse
        temperature, $\beta$; array of uniformly distributed random numbers,
        $rn \in [0, 1)$
for $i \leftarrow 0$ to $N$ do
    select a random lattice site $\mathbf{r}$;
    generate a new random orientation for spin at $\mathbf{r}$, $\mathbf{S}'(\mathbf{r})$;
    $\Delta E = -\mathbf{H}(\mathbf{r}) \cdot \big(\mathbf{S}'(\mathbf{r}) - \mathbf{S}(\mathbf{r})\big)$;
    if $\Delta E \leq 0$ then
        $\mathbf{S}(\mathbf{r}) \leftarrow \mathbf{S}'(\mathbf{r})$;
        update $\mathbf{H}$ values;
    end
    else if $\exp(-\beta \Delta E) > rn$ then
        $\mathbf{S}(\mathbf{r}) \leftarrow \mathbf{S}'(\mathbf{r})$;
        update $\mathbf{H}$ values;
end
```

Algorithm 2: Heat-bath MC step

```
input  : array of $N$ spin vectors, $\mathbf{S}(\mathbf{r})$; array of effective field vectors, $\mathbf{H}(\mathbf{r})$;
         inverse temperature, $\beta$
for $i \leftarrow 0$ to $N$ do
    select a random lattice site $\mathbf{r}$;
    generate random numbers $r_1$ and $r_2$;
    $\phi(\mathbf{r}) \leftarrow 2\pi r_1$;
    $\cos\theta(\mathbf{r}) \leftarrow 1 + \frac{1}{\beta H(\mathbf{r})} \ln\left(r_2 + (1 - r_2)e^{-2\beta H(\mathbf{r})}\right)$;
    $\mathbf{S}(\mathbf{r}) = [\cos\phi(\mathbf{r})\sin\theta(\mathbf{r}), \sin\phi(\mathbf{r})\sin\theta(\mathbf{r}), \cos\theta(\mathbf{r})]$;
    rotate $\mathbf{S}(\mathbf{r})$ to the global coordinate frame;
    update $\mathbf{H}(\mathbf{r})$ values;
end
```

Algorithm 3: Over-relaxation lattice update

```
input  : array of $N$ spin vectors, $\mathbf{S}(\mathbf{r})$; array of effective field vectors, $\mathbf{H}(\mathbf{r})$;
         inverse temperature, $\beta$
for $i \leftarrow 0$ to $N$ do
    select $i^{\text{th}}$ lattice site $\mathbf{r}$;
    $\mathbf{S}(\mathbf{r}) \leftarrow \frac{2\mathbf{S}(\mathbf{r})\cdot\mathbf{H}(\mathbf{r})}{H^2(\mathbf{r})}\mathbf{H}(\mathbf{r}) - \mathbf{S}(\mathbf{r})$;
    update $\mathbf{H}(\mathbf{r})$ values;
end
```

Appendix C

Quadratic optimization

In chapters 6 and 7 we obtain harmonic expansions of the energy of the form

$$\begin{aligned} E(\mathbf{x}) &= e_0 + \sum_i g_i x_i + \frac{1}{2} \sum_{ij} h_{ij} x_i x_j \\ &= e_0 + \mathbf{g} \cdot \mathbf{x} + \frac{1}{2} \mathbf{x}^T \mathbf{h} \mathbf{x}, \end{aligned} \tag{C.1}$$

where $\mathbf{x}$ are the expansion variables contained in a M-dimensional vector, e_0 is a constant, $\mathbf{g}$ is a vector of M linear coefficients (alternatively, a gradient vector), and $\mathbf{h}$ is a symmetric $M \times M$ matrix of quadratic coefficients (or the Hessian matrix). The condition for the minimum can be determined by calculating the derivative with respect to variable x_k:

$$\begin{aligned} \frac{\partial E}{\partial x_k} &= g_k + \frac{1}{2} \left(\sum_i h_{ik} x_i + \sum_j h_{kj} x_j \right) \\ &= g_k + \sum_i h_{ki} x_i = 0, \end{aligned} \tag{C.2}$$

or, in vector form,

$$\nabla_{\mathbf{x}} E = \mathbf{g} + \mathbf{h}\mathbf{x} = \mathbf{0}. \tag{C.3}$$

To simplify the problem, it often helps to switch to a basis that diagonalizes the Hessian. We will denote the variable and gradient vectors in the new basis as $\tilde{\mathbf{x}}$ and $\tilde{\mathbf{g}}$, and the k^{th} eigenvalue of the Hessian as $\tilde{h}_k$. The condition for the minimum becomes

$$\tilde{g}_k + \tilde{h}_k \tilde{x}_k = 0. \tag{C.4}$$

Therefore, in order to be able to minimize the energy function, we must ensure that the eigenvalues of the Hessian are non-negative. This is equivalent to saying that the energy must be convex and the Hessian matrix is positive semidefinite. Note that a function will have a unique minimum if and only if it is *strictly* convex, meaning that the Hessian is positive definite. The difference between definite and semidefinite matrices is that the latter has one or several zero eigenvalues. The only way to satisfy eq. (C.4) when $\tilde{h}_k$ is zero is by ensuring that $\tilde{g}_k$ is also zero. If this cannot be achieved, the minimization problem is ill-defined. If both $\tilde{g}_k$ and $\tilde{h}_k$ are equal to zero, the corresponding eigenvector describes a collective zero-energy mode. In all other cases, the solution is simply

$$\tilde{x}_k^{(\mathrm{min})} = -\frac{\tilde{g}_k}{\tilde{h}_k}. \tag{C.5}$$

Since the energy is invariant under a change of basis, we obtain the minimum energy value

$$\begin{aligned} E^{(\mathrm{min})} &= e_0 + \delta E \\ \delta E &= -\sum_k \frac{\tilde{g}_k^2}{2\tilde{h}_k} = -\frac{1}{2}\mathbf{g}^T\mathbf{h}^{-1}\mathbf{g}. \end{aligned} \tag{C.6}$$

Appendix D

Phase transitions in 2D spin systems

In Chapter 8, we study thermal properties of a single AB-stacked bilayer, which corresponds to a quasi-2D system. We therefore dedicate this appendix to a review of the phase transition theory in 2D.

D.1 Thermodynamic quantities

In statistical mechanics, the partition function Z describes all of the equilibrium properties of a given physical system. It can be written as

$$Z = \mathrm{Tr}\Big\{e^{-\beta\mathcal{H}}\Big\}, \tag{D.1}$$

where the trace indicates a summation or integration over all possible degrees of freedom in a system described by the Hamiltonian $\mathcal{H}$. A statistical average of any quantity X is defined as

$$\langle X\rangle = \frac{1}{Z}\,\mathrm{Tr}\Big\{Xe^{-\beta\mathcal{H}}\Big\}. \tag{D.2}$$

An important identity that connects the statistical theory of the microscopic degrees of freedom to the macroscopic thermodynamics is the expression of the Helmholtz free energy as a logarithm of the partition function:

$$F = -k_B T \ln Z. \tag{D.3}$$

Using this equation, we can define most thermodynamic quantities either in terms of the statistical averages in eq. (D.2) or as derivatives of the free energy F. We will demonstrate this with a few examples.

Internal energy and heat capacity

The average internal energy of the system is simply calculated using

$$\begin{aligned}
\langle\mathcal{H}\rangle &= \frac{1}{Z}\,\mathrm{Tr}\Big\{\mathcal{H}e^{-\beta\mathcal{H}}\Big\} \\
&= -\frac{1}{Z}\frac{\partial Z}{\partial\beta} \\
&= -\frac{\partial}{\partial\beta}\ln Z = -\frac{\partial(\beta F)}{\partial\beta}. \qquad \text{(D.4)}
\end{aligned}$$

The heat capacity is simply the temperature derivative of $\langle\mathcal{H}\rangle$:

$$\begin{aligned}
C_v &= \frac{\partial\langle\mathcal{H}\rangle}{\partial T} \\
&= k_B\beta^2\frac{\partial^2(\beta F)}{\partial\beta^2} \qquad \text{(D.5)} \\
&= k_B\beta^2\left[-\left(\frac{1}{Z}\frac{\partial Z}{\partial\beta}\right)^2 + \frac{1}{Z}\,\mathrm{Tr}\Big\{\mathcal{H}^2e^{-\beta\mathcal{H}}\Big\}\right] \\
&= k_B\beta^2\left[\langle\mathcal{H}^2\rangle - \langle\mathcal{H}\rangle^2\right]. \qquad \text{(D.6)}
\end{aligned}$$

The heat capacity is a measure of thermal fluctuations and is typically used to identify qualitative changes in the structure of the system, such as phase transitions.

Order parameters, susceptibilities, and correlation functions

One of the most profound observations in physics is that we can characterize the properties of a macroscopic system, composed of an uncountable number of degrees of freedom, using only a few important parameters. These important parameters describe the collective behaviour of the degrees of freedom and can be used to represent the overall state of the system. In the studies of phase transitions, we often try to identify a quantity that characterizes the ordered phase, which is then simply called the *order parameter*. An ideal order parameter quantity is zero in the disordered phase and non-zero in the ordered phase. For example, in the case of a ferromagnetic phase, the appropriate order parameter is a uniform magnetization, $\mathbf{m} = \sum_{\mathbf{r}}\mathbf{S}(\mathbf{r})$. In order to calculate the average magnetization, it is useful to temporarily add an applied field $\mathbf{H}$, such that the energy of the system is modified as $\mathcal{H} \to \mathcal{H} - \mathbf{H}\cdot\mathbf{m}$. As a result, we obtain

$$\begin{aligned}\langle m_\alpha \rangle &= \frac{1}{Z}\,\mathrm{Tr}\Big\{ m_\alpha e^{-\beta(\mathcal{H}-\mathbf{H}\cdot\mathbf{m})} \Big\} \\ &= \frac{1}{Z}\frac{\partial Z}{\partial \beta H_\alpha} \\ &= \frac{\partial}{\partial \beta H_\alpha}\ln Z = \left.\frac{\partial F}{\partial H_\alpha}\right|_{\mathbf{H}=0}, \end{aligned} \tag{D.7}$$

where in the last step we took the limit of zero field to recover the original Hamiltonian. The susceptibility, which determines the response of the system to a magnetic field, is defined as

$$\begin{aligned}\chi_{\alpha\beta} &= \left.\frac{\partial \langle m_\alpha \rangle}{\partial H_\beta}\right|_{\mathbf{H}=0} \\ &= \left.\frac{\partial^2 F}{\partial H_\alpha \partial H_\beta}\right|_{\mathbf{H}=0} && \text{(D.8)} \\ &= \beta\left[\langle m_\alpha m_\beta\rangle - \langle m_\alpha\rangle\langle m_\beta\rangle\right], && \text{(D.9)}\end{aligned}$$

such that is provides the information about the fluctuations of the magnetization. These definitions can be extended to any quantity of interest. For example, by including an inhomogeneous field $\mathbf{H}(\mathbf{r})$ in the system, we can obtain

$$\begin{aligned}\langle S_\alpha(\mathbf{r}) \rangle &= \frac{1}{Z}\,\mathrm{Tr}\Big\{ S_\alpha(\mathbf{r}) e^{-\beta(\mathcal{H}-\sum_{\mathbf{r}}\mathbf{H}(\mathbf{r})\cdot\mathbf{S}(\mathbf{r}))} \Big\} \\ &= \frac{1}{Z}\frac{\partial Z}{\partial \beta H_\alpha(\mathbf{r})} \\ &= \left.\frac{\partial F}{\partial H_\alpha(\mathbf{r})}\right|_{\mathbf{H}(\mathbf{r})=0}, \end{aligned} \tag{D.10}$$

from which the generalized spin susceptibility is

$$\begin{aligned}\chi_{\alpha\beta}(\mathbf{r},\mathbf{r}') &= \left.\frac{\partial^2 F}{\partial H_\alpha(\mathbf{r}) \partial H_\beta(\mathbf{r}')}\right|_{\mathbf{H}(\mathbf{r})=0} && \text{(D.11)} \\ &= \beta\left[\langle S_\alpha(\mathbf{r}) S_\beta(\mathbf{r}')\rangle - \langle S_\alpha(\mathbf{r})\rangle\langle S_\beta(\mathbf{r}')\rangle\right]. && \text{(D.12)}\end{aligned}$$

If we assume that the system is isotropic and possesses the translational symmetry, we may rewrite eq. (D.12) as

$$k_B T \chi(\boldsymbol{\rho}) = \mathcal{S}(\boldsymbol{\rho}), \tag{D.13}$$

where $\boldsymbol{\rho} = \mathbf{r} - \mathbf{r}'$ and

$$\mathcal{S}(\boldsymbol{\rho}) = \frac{1}{N} \sum_{\mathbf{r}} \left[\langle \mathbf{S}(\mathbf{r}) \cdot \mathbf{S}(\mathbf{r} - \boldsymbol{\rho}) \rangle - \langle \mathbf{S}(\mathbf{r}) \rangle \cdot \langle \mathbf{S}(\mathbf{r} - \boldsymbol{\rho}) \rangle \right] \tag{D.14}$$

is the *two-point correlation function.* Note that in the disordered phase, $\langle \mathbf{S}(\mathbf{r}) \rangle = 0$, which eliminates the second term in the brackets in eq. (D.14).

D.2 Types of phase transitions

In the previous section we introduced the concept of an order parameter. As we cross a phase transition point from disordered to the ordered phase, the value of the order parameter changes from zero to non-zero. The way in which this change occurs determines the two main types of phase transitions: if the order parameter changes in a discontinuous (continuous) fashion, we say that the phase transition is first (second) order. This classification is due to Ehrenfest [173], who distinguished the phase transitions based on the derivatives of the free energy that become discontinuous at the transition point. From the previous section, we see that the average energy and order parameters are related to the first-order derivatives of F, and therefore change abruptly during a first-order transition. At the same time, in a second-order transition, these quantities remain continuous, while the properties like the heat capacity and susceptibility, which derive from the second-order derivatives of the free energy, still become singular.

Most phase transitions in nature are first-order transitions. At the transition point, most of the properties change abruptly to their new values, often without any precursors[1]. The central concept in the theory of first-order transitions is *metastability.* We will illustrate this using a phenomenological description of the free energy as a function of the order parameter Ψ in fig. D.1 (a). At high enough temperatures

---

[1] For example, consider liquid water, which at 0 °C becomes ice, and at 100 °C – vapour. Both transitions correspond to an abruptly changing density, and occur without any intermediate phases, such as slush or mist.

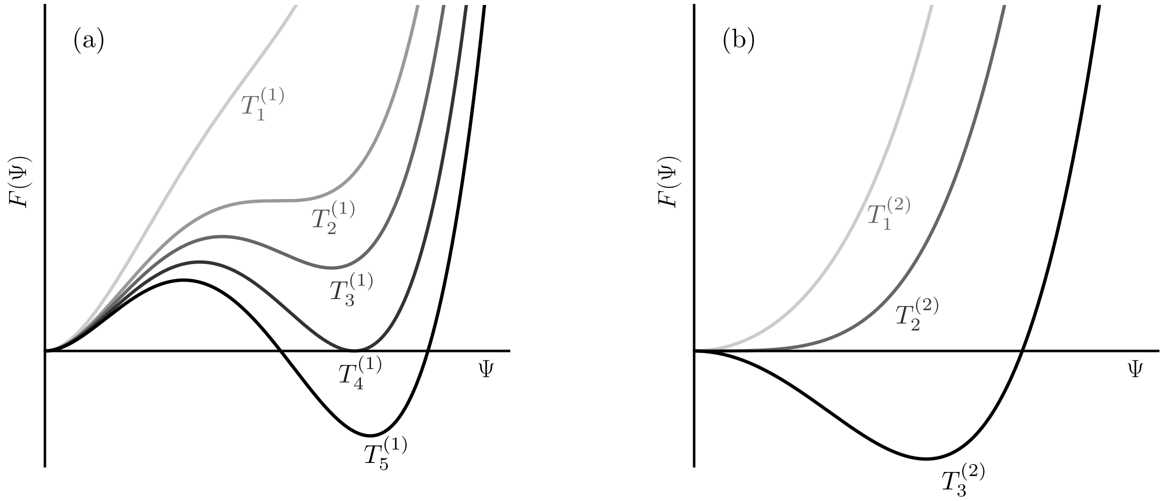

Figure D.1: A phenomenological illustration of the free energy $F(\Psi)$ as function of the order parameter Ψ at different temperatures during a first-order (a) and second-order (b) phase transitions. The meaning of the temperatures is explained in the main text.

(*e.g.* $T = T_1^{(1)}$ in fig. D.1 (a)), the fluctuations dominate in the system and the disordered state at $\Psi = 0$ is the only stable minimum of the system. As the temperature is decreased ($T = T_1^{(2)}$), the energetic interactions become sufficient to stabilize the ordered configurations with $\Psi \neq 0$. However, if the fluctuations are still large, the free energy will favour the high entropy disordered state, and $F(\Psi = 0)$ will remain the global minimum. Thus, at temperatures $T_3^{(1)} < T \leq T_4^{(1)}$, the ordered state at $\Psi \neq 0$ produces a local minimum in the free energy and is therefore metastable, since it does not correspond to the equilibrium phase. As the temperature is lowered to $T = T_4^{(1)}$, the two minima become equal, leading to coexisting states. Finally, below the transition point, the ordered state becomes the global free energy minimum, while the disordered state becomes metastable, as shown for $T = T_5^{(1)}$. Often, the metastability persists for a wide range of temperatures, which means that if the system passes through the transition point too quickly, it may get trapped in the metastable minimum, leading to an *out-of-equilibrium state*.

In second-order transitions, the system evolves continuously from the disordered phase to the ordered one. In this case, at any temperature, the free energy has only a single minimum, as shown in fig. D.1 (b). As in the previous example, at high temperatures (*e.g.* $T = T_1^{(2)}$) the system starts off in the disordered state where the free energy has a single minimum at $\Psi = 0$. This time, no metastable states form, and the system undergoes a transition at $T = T_2^{(2)}$ from the disordered to the ordered state, shifting the minimum of the free energy from $\Psi = 0$ to $\Psi \neq 0$ in a continuous fashion. At lower temperatures (*e.g.* $T = T_3^{(2)}$), the free energy has a single minimum corresponding to the ordered state. In the vicinity of a second-order phase transition, the singular parts of the thermodynamic quantities follow power laws in control variables (such as temperature and external field), measured with respect to the transition point. Each thermodynamic property is therefore associated with a *critical exponent* that determines the singular behaviour. For example, if Ψ is the order parameter and $\mathcal{S}(\rho)$ is the corresponding correlation function (with ρ representing distance), close to the transition point at $T = T_c$ we would have

$$\Psi \sim (T_c - T)^{\beta}, \tag{D.15}$$

$$S(\rho) \sim \rho^{2-d-\eta}, \tag{D.16}$$

where β and η are typically used to label the critical exponents for the order parameter and correlation function, and d is the spatial dimensionality of the system. Surprisingly, the critical exponents turn out to be independent of the microscopic details of the model, and instead are specified by the overall symmetry of the system and the type of the order parameter. Therefore, the critical exponents provide a *universal* classification of the second-order phase transitions. The discovery of universality is an extremely important achievement of the celebrated *renormalization group theory.* Although we will not discuss it here, these concepts are covered in most of the modern statistical mechanics books, such as in Refs. [174–176].

The last important concept that we would like to mention here is the *spontaneous symmetry breaking.* Frequently, a transition into a more ordered phase is accompanied by the lowering of the symmetry. For example, when a liquid freezes into a crystalline solid, the average distribution of particles (atoms or molecules) changes from spatially uniform to periodic. This means that the continuous translations and rotations are reduced to the discrete crystal symmetries, as dictated by the corresponding space group. Second-order transitions are always associated with a broken symmetry, while the first-order transitions may occur without any change in symmetry. The example of the latter is a liquid-gas transition, where the symmetry of both states is unchanged by the abrupt change in the density. Importantly, the spontaneous symmetry breaking occurs solely as a result of minimization of the free energy, and not because of the symmetry-lowering terms in the model Hamiltonian.

D.3 2D Ising ferromagnet

One of the simplest models to allow for a phase transition is the 2D Ising model on a square lattice:

$$\mathcal{H} = J \sum_{\langle \mathbf{r}\mathbf{r}' \rangle} S(\mathbf{r}) S(\mathbf{r}'), \tag{D.17}$$

where the sum is over the NN on a square lattice, and $S(\mathbf{r}) = \pm 1$ are the discrete Ising spins. Originally invented by Wilhelm Lenz in 1920, the 1D version of this model was solved by his student, Ernst Ising, who showed that there was no phase transition [177]. The 2D model was later realized to possess a phase transition [178], but its solution evaded the scholars for over a decade. Arguably the most significant and impressive achievement in the theory of phase transitions was the analytical solution of the 2D Ising model by Lars Onsager in 1944 [94]. Onsager's solution revealed a second-order transition between the disordered and the ferromagnetic phases. In this case, the ferromagnetic state breaks the discrete time-reversal symmetry (see Chapter 2.2) by establishing a spontaneous magnetization. In the vicinity of the transition temperature T_c, the magnetization behaves as

$$m \sim (T_c - T)^{\frac{1}{8}}, \tag{D.18}$$

where as in eq. (D.15), 1/8 is the Ising critical exponent for the order parameter.

The original 1944 paper by Onsager is extremely complicated, and it took another decade for various authors to simplify this solution. Nevertheless, it provided the first rigorous example of a phase transition at which various thermodynamic functions become singular, with the singularities described by the critical exponents. It also established the foundation for the studies of phase transitions in more complicated magnetic systems[2]. For further reading on the Ising model, we suggest the material in Refs. [174, 176].

D.4 Mermin-Wagner theorem

A natural generalization of the 2D Ising model is an exchange model with continuous spins (typically either 2-component XY, 3-component Heisenberg spins), as presented in eq. (1.2). For simplicity, we will continue the discussion assuming the same system as in the last section: a ferromagnetic NN model on a square lattice. The order parameter of this model is still the magnetization, although it will now be a vector quantity with the same number of components as the spin vectors. As discussed in Chapter 2, the exchange model with continuous spins is isotropic and will have a continuous rotational symmetry. This means that in the ferromagnetic phase, we can rotate the magnetization vector in an arbitrary angle, without changing the energy of the system. In contrast, in the Ising model, the degeneracy of the ground state is discrete, since the corresponding time-reversal symmetry simply changes the sign of the magnetization. An important consequence of the rotational symmetry in a system with continuous spins is that the low-energy excitations correspond to spin-wave fluctuations with large wavelengths, which cost significantly less energy than individual spin flips in the Ising systems.

Since the 2D Ising model is known to display a second-order phase transition, naively we might assume that the continuous models will also have one, albeit belonging to a different universality class. However, let us consider the value of the correlation function $\mathcal{S}(\boldsymbol{\rho})$ (eq. (D.14)) in the ferromagnetic phase in the limit of large spin-spin separation ($\rho = |\boldsymbol{\rho}| \to \infty$). If the ferromagnetic order is stable against fluctuations, this limit should yield a finite value, meaning that the spins are correlated over macroscopic distances. One can show that in the presence of the long-wavelength spin fluctuations, the correlation function becomes

$$\mathcal{S}(\rho) \propto \exp\left(-KC_d(\rho)\right), \tag{D.19}$$

---

[2] For example, the seminal paper on the antiferromagnetic Ising model on a triangular lattice by Wannier was based on Onsager's derivation [15]

where $K = \frac{k_B T}{J}$ and

$$C_d(\rho) = \begin{cases} \frac{\rho^{2-d} - a^{2-d}}{(2-d) S_d}, & \text{if } d \neq 2, \\ \frac{\ln(\rho) - \ln(a)}{2\pi}, & \text{if } d = 2, \end{cases} \tag{D.20}$$

$$S_d = \frac{2\pi^{d/2}}{(d/2-1)!}, \tag{D.21}$$

where d is the spatial dimension of the system, and a is the inter-atomic distance. Therefore,

$$\lim_{\rho\to\infty} \mathcal{S}(\rho) = \begin{cases} \mathcal{S} & \text{if } d > 2, \\ 0 & \text{if } d \leq 2, \end{cases} \tag{D.22}$$

where $\mathcal{S}$ is a positive constant. We see that the long-range order is only possible in 3D systems, while in 1D and 2D it is completely destroyed by the fluctuations. This is a manifestation of a much more general theorem, which states that there is no spontaneous breaking of continuous symmetry in systems with short-range interactions and dimensions $d \leq 2$. This theorem is named after Herbert Wagner and David Mermin, who first proved it for ferromagnetic and antiferromagnetic phases [179]. Importantly, this theorem does not apply to the Ising model in the previous section, since it does not have any continuous symmetries.

D.5 Kosterlitz-Thouless transition

Although the Mermin-Wagner theorem places a strict constraint on the existence of a long-range order in systems with continuous symmetry, one may notice that in 2D, the correlation function in eq. (D.19) becomes

$$\mathcal{S}(\rho) \propto \rho^{-\eta(T)}, \tag{D.23}$$

where

$$\eta(T) = \frac{k_B T}{2\pi J}. \tag{D.24}$$

This leads to a few interesting observations. Firstly, in the high-temperature limit, we expect the correlations to decay exponentially, regardless of the dimensionality of the system. However, at low-temperature the correlations in a 2D system display an algebraic decay, as evident from eq. (D.23). This implies a qualitative change in the properties of the system at some finite intermediate temperature. Secondly, the expression in eq. (D.23) is of the same form as eq. (D.16), which describes correlations near a second-order transition. The difference comes from the fact that the exponent in (D.23) is non-universal, since it depends on the coupling constant J, and is temperature-dependent, which is inconsistent with a singular transition point. These observations lead to a conclusion that there may be a sort of a phase transition in a 2D system with continuous symmetry, which, however, does not yield a long-range order.

The answer to this puzzle was provided in a series of works on a ferromagnetic XY model, which revealed a novel type of phase transitions, namely a *topological phase transition* [180, 181]. This transition is often named after John Kosterlitz and David Thouless, who first discovered it. In order to understand the origin of this transition, we must take a more careful look at the low-energy excitations in the XY model. We have already discussed the role of small amplitude spin-wave fluctuations, which can be viewed as simple harmonic excitations with respect to the ferromagnetic state. However, there is another type of excitations that cannot be obtained from a ferromagnetic configuration by any continuous rotations. These are the *topological defects*, which in the XY model manifest as the *magnetic vortices*, shown in figs. 8.5 (a), (b). The reason for the term "topological" is that these excitations possess an integer *winding number*, as illustrated in the figures. We refer to defects with positive and negative winding numbers as vortices and antivortices, respectively. The vortices and antivortices behave similarly to charged particles, such that the defects with the opposite winding numbers attract, while those with the same windings repel. For this reason, the winding number is also sometimes called the *topological charge*. At high temperatures, vortices and antivortices are generated simultaneously, but they remain isolated (or free), leading to a high-entropy disordered state. However, as the temperature is lowered, the effective interactions between the defects with opposite topological charges become more and more prominent. Eventually, every vortex in the system is paired with an antivortex, simultaneously minimizing the energy and lowering the entropy. The temperature at which this pairing occurs corresponds to the Kosterlitz-Thouless (KT) phase transition.

It is important to point out some of the differences between the conventional phase transitions and the KT transition. In terms of the Ehrenfest classification, the KT transition does not correspond to either a first or second-order transition, since the quantities related to the first and second derivatives of the free energy remain non-singular[3]. Most importantly, the KT transition does not lead to a long-range order, since the correlations still decay at large distances. However, since the decay is algebraic rather than exponential, the low-temperature phase is often said to possess a *quasi-long-range* order.

---

[3] In fact, it is considered to be an infinite-order transition, since the free energy remains smooth at all temperatures.